MINISTÉRIO DA CIÊNCIA, TECNOLOGIA E INOVAÇÃO
INSTITUTO NACIONAL DE PESQUISAS ESPACIAIS

sid.inpe.br/mtc-m21d/2023/07.07.00.48-TDI

STUDY ON THE ROLE OF THE GYRORESONANCE IN THE BRIGHTNESS TEMPERATURE GRADIENT AT 17 GHZ OF SOLAR ACTIVE REGIONS

Abimael Xavier Barbosa Amaro

Doctorate Thesis of the Graduate Course in Space Geophysics, guided by Drs. Marlos Rockenbach da Silva, and Joaquim Eduardo Rezende Costa, approved in June 30, 2023.

URL of the original document:
<http://urlib.net/8JMKD3MGP3W34T/49DJHRL>

INPE
São José dos Campos
2023

PUBLISHED BY:

Instituto Nacional de Pesquisas Espaciais - INPE
Coordenação de Ensino, Pesquisa e Extensão (COEPE)
Divisão de Biblioteca (DIBIB)
CEP 12.227-010
São José dos Campos - SP - Brasil
Tel.:(012) 3208-6923/7348
E-mail: pubtc@inpe.br

MINISTÉRIO DA CIÊNCIA, TECNOLOGIA E INOVAÇÃO
INSTITUTO NACIONAL DE PESQUISAS ESPACIAIS

sid.inpe.br/mtc-m21d/2023/07.07.00.48-TDI

STUDY ON THE ROLE OF THE GYRORESONANCE IN THE BRIGHTNESS TEMPERATURE GRADIENT AT 17 GHZ OF SOLAR ACTIVE REGIONS

Abimael Xavier Barbosa Amaro

Doctorate Thesis of the Graduate Course in Space Geophysics, guided by Drs. Marlos Rockenbach da Silva, and Joaquim Eduardo Rezende Costa, approved in June 30, 2023.

URL of the original document:
<http://urlib.net/8JMKD3MGP3W34T/49DJHRL>

INPE
São José dos Campos
2023

Cataloging in Publication Data

Amaro, Abimael Xavier Barbosa.

Am13s Study on the role of the gyroresonance in the brightness temperature gradient at 17 GHz of solar active regions / Abimael Xavier Barbosa Amaro. – São José dos Campos : INPE, 2023.

xxvi + 88 p. ; (sid.inpe.br/mtc-m21d/2023/07.07.00.48-TDI)

Thesis (Doctorate in Space Geophysics) – Instituto Nacional de Pesquisas Espaciais, São José dos Campos, 2023.

Guiding : Drs. Marlos Rockenbach da Silva, and Joaquim Eduardo Rezende Costa.

1. Gyroresonance. 2. Solar active region. 3. bremsstrahlung. 4. Circular polarization degree. 5. Brightness temperature gradient. I.Title.

CDU 523.98

MINISTÉRIO DA CIÊNCIA, TECNOLOGIA E INOVAÇÃO

INSTITUTO NACIONAL DE PESQUISAS ESPACIAIS
Serviço de Pós-Graduação - SEPGR

DEFESA FINAL DE TESE DE ABIMAEL XAVIER BARBOSA AMARO
REG. 458400/2018, BANCA Nº 171/2023

No dia 30 de junho de 2023, de forma híbrida, o(a) aluno(a) mencionado(a) acima defendeu seu trabalho final (apresentação oral seguida de arguição) perante uma Banca Examinadora, cujos membros estão listados abaixo. O(A) aluno(a) foi APROVADO(A) pela Banca Examinadora, por unanimidade, em cumprimento ao requisito exigido para obtenção do Título de Doutor em Geofísica Espacial/Ciências do Ambiente Solar-Terrestre, com a exigência de que o trabalho final a ser publicado deverá incorporar as correções sugeridas pela Banca Examinadora, com revisão pelo(s) orientador(es).

Título: Study on the role of the gyroresonance in the brightness temperature gradient at 17 GHz of solar active regions

Membros da banca:

Dr. Alisson Dal Lago – Presidente – INPE
Dr. Marlos Rockenbach da Silva – Orientador – INPE
Dr. Joaquim Eduardo Rezende Costa – Orientador – INPE
Dr. Luis Eduardo Antunes Vieira – Membro Interno – INPE
Dr. Jean Carlo Santos – Membro Externo – UFTPR
Dr. Caius Lucius Selhorst – Membro Externo – NJIT

Documento assinado eletronicamente por **Marlos Rockenbach da Silva**, **Pesquisador**, em 03/07/2023, às 08:52 (horário oficial de Brasília), com fundamento no § 3º do art. 4º do Decreto nº 10.543, de 13 de novembro de 2020.

Documento assinado eletronicamente por **jean carlo santos (E)**, **Usuário Externo**, em 03/07/2023, às 09:18 (horário oficial de Brasília), com fundamento no § 3º do art. 4º do Decreto nº 10.543, de 13 de novembro de 2020.

Documento assinado eletronicamente por **Luis Eduardo Antunes Vieira**, **Pesquisador**, em 03/07/2023, às 20:25 (horário oficial de Brasília), com fundamento no § 3º do art. 4º do Decreto nº 10.543, de 13 de novembro de 2020.

Documento assinado eletronicamente por **Caius lucius selhorst (E)**, **Usuário Externo**, em 05/07/2023, às 15:37 (horário oficial de Brasília), com fundamento no § 3º do art. 4º do Decreto nº 10.543, de 13 de novembro de 2020.

Documento assinado eletronicamente por **Alisson Dal Lago**, **Pesquisador**, em 06/07/2023, às 09:30 (horário oficial de Brasília), com fundamento no § 3º do art. 4º do Decreto nº 10.543, de 13 de novembro de 2020.

Documento assinado eletronicamente por **Joaquim Eduardo Rezende Costa**, **Pesquisador**, em 25/08/2023, às 11:03 (horário oficial de Brasília), com fundamento no § 3º do art. 4º do Decreto nº 10.543, de 13 de novembro de 2020.

A autenticidade deste documento pode ser conferida no site https://sei.mcti.gov.br/verifica.html, informando o código verificador **11165166** e o código CRC **B0C9F0F2**.

Referência: Processo nº 01340.005301/2023-36 SEI nº 11165166

"One thing I have learned in a long life: that all our science, measured against reality, is primitive and childlike—and yet it is the most precious thing we have."

Albert Einstein
through his letter written in 1951 to Hans Mühsam.

Aos meus pais, ***Antônia Theodora Xavier*** *e* ***João Amaro****, à minha irmã* ***Abinoane Amaro****, às minhas sobrinhas,* ***Alice*** *e* ***Stella****, e à minha psicóloga* ***Raquel****.*

ACKNOWLEDGEMENTS

Parafraseando o físico Isaac Newton, posso dizer que, se fui tão longe, foi por estar apoiado na gigantesca generosidade de pessoas queridas e importantes, às quais sou eternamente grato. Entre elas, devo começar por minha mãe, Antônia Theodora, que sempre me incentivou e me mostrou meu potencial, além de ter me ajudado em situações difíceis inúmeras vezes. Também faço menção ao meu pai, João Amaro, que me incentivou e me apoiou bastante desde que fui aprovado no exame de admissão a este curso de doutorado. De igual modo, lembro com carinho do apoio da minha irmã Abinoane, da Tia Laura, de Jurandir e Patrícia. Também sou grato à minha psicóloga Raquel, que generosamente tem me auxiliado desde fevereiro de 2020. Agradeço ao primo paterno Inácio Rodrigues, que me recebeu aqui em São José dos Campos-SP e tem sido muito hospitaleiro comigo. Também agradeço à Rita, pelo apoio e pelas dicas de língua inglesa.

Como filho da Universidade Federal do Rio Grande do Norte (UFRN), agradeço ao Dr. Enivaldo Bonelli (meu orientador de mestrado), ao Dr. Gilvan Borba (meu co-orientador de mestrado) e ao Dr. José Henrique Fernandez, que me recomendaram a este doutorado.

No INPE, agradeço ao Dr. Marlos Rockenbach por sua dedicação em supervisionar meu trabalho. Também agradeço ao Dr. Joaquim Costa, que pacientemente me orientou na condução desta tese. Agradeço ao amigo Alexandre José, que apresentou o SSW e me ajudou a instalar esse programa. Sou grato ainda ao Dr. Alisson Dal Lago por seus conselhos, que têm me ajudado a planejar melhor meus próximos passos. Agradeço também ao Dr. Luiz Vieira por abrir as portas do seu grupo do telescópio solar Galileu. Também devo meus agradecimentos aos meus professores: os doutores Severino Dutra, Odim Mendes Jr., Jonas de Souza, Alisson Dal Lago, Renato Dallaqua, Cristiano Wrasse, Alicia Gonzalez, Eurico de Paula e Fábio Guedes. Agradeço às secretárias Filó e Yasmim pelo zelo e dedicação aos serviços prestados; aos colegas Lucas Vieira, Sony Chen, Diego Prado Barroso, Hadassa Jácome, Isabela Martins, Patrick Essein e Solomon Lomotey; à equipe da Biblioteca, em especial ao André Fernandes e à Simone Barbedo, pelo excelente trabalho e pela disposição em tirar minhas dúvidas sobre a adequação deste trabalho às normas da ABNT.

Concernente às instituições, devo minha gratidão: ao Instituto Nacional de Pesquisas Espaciais (INPE), em especial à sua Diretoria, à Secretaria de Pós-Graduação (SPG), à graduação em Geofísica Espacial e à Divisão de Heliofísica, Ciências Planetárias e Aeronomia (DIHPA), por criarem um ambiente propício ao desenvolvimento de

pesquisa de fronteira; à Agência Espacial Brasileira (AEB), pelo suporte financeiro ao INPE; à Coordenação de Aperfeiçoamento de Pessoal de Nível Superior (CAPES), por fomentar meu trabalho de doutorado; ao *Nobeyama Solar Radio Observatory*, ao *National Astronomical Observatory of Japan* (*NAOJ*), e ao *International Consortium for the Continued Operation of Nobeyama Radioheliograph* (*ICCON*), pelos mapas solares em 17 GHz sintetizados pelo *Nobeyama Radioheliograph* e utilizados nesta tese; e à *National Aeronautics and Space Administration* (*NASA*) pelos magnetogramas gerados pelo *Solar Dynamics Observatory* (*SDO*) também utilizados nesta pesquisa.

Agradeço a S. L. Freeland e B. N. Handy por desenvolver e legar, para a comunidade da Física Solar, o *SolarSoftWare* (*SSW*), utilizado neste trabalho.

Por fim, agradeço à Banca examinadora por avaliar este trabalho e pelas sugestões de melhorias para minha tese.

ABSTRACT

The gyroresonance-driven control over the radio brightness temperature (T_b) coming from active regions is a fact recognized by several authors over the past decades. However, until the present work, there was no clarity regarding the relationship between such a radio mechanism and the brightness temperature gradient ($\vec{\nabla}T_b$). Furthermore, the direct association of specific magnetic field strengths with the opacity of the medium affected by gyroresonant electrons has led this work to consider the magnetic control not only of the radio brightness but also its gradient. Demonstration of this control, then, may be useful in better identifying sources of gyroresonance. Therefore, among the HMI magnetograms from the Solar Dynamics Observatory (SDO), this work selected 8 large active regions on the 1st half of the 24th solar cycle. Correspondent to these selected regions, 17 GHz maps synthesized by the Nobeyama Radioheliograph (NoRH) were also obtained. We then analyzed each active region through its simultaneous data: photospheric magnetic field and 17 GHz brightness. For each active region, after fitting the magnetograms with the brightness maps (both within a few minutes of each other), we found that the contours of magnetic field strengths associated with the 3rd and 4th harmonics of the gyrofrequency for 17 GHz are partially or completely enveloped by brightness bumps. These bumps were identified both by BT maps, with a brightness temperature distribution, and by BTG maps, with a brightness temperature gradient field. In both types of maps, most of the bumps exhibit a (semi) circular morphology of brightness contours, and an intense degree of circular polarization (r_c), of modulus above 30%, characterizing a gyroresonance source. We also found that both T_b and $|\vec{\nabla}T_b|$ are strongly correlated with $|r_c| \geq 30\%$ in most of the cases, whereas their correlation with $|r_c| < 30\%$ can be classified as weak to moderate in all the cases. During the occurrence of flares and/or at times close to such an event, the correlation between these brightness variables with $|r_c| \geq 30\%$ tends to drop, assuming weak or moderate values. Even under these conditions, the bumps remained with a high degree of circular polarization, opening the possibility of the joint influence of other emission mechanism(s) not investigated in this work. The present thesis also found bumps without a high degree of polarization and outside the influence of flares, which we consider as the bremsstrahlung effect, given the intensification of charge carrier shocks in a plasma confined in strong magnetic fields. However, considering the aforementioned strong correlations associated with highly polarized bumps with magnetic fields corresponding to gyroresonance, this work was able to demonstrate the predominant role of such a radio mechanism on the process of brightness intensification at 17 GHz.

Keywords: gyroresonance. solar active region. bremsstrahlung. circular polarization degree. brightness temperature gradient.

ESTUDO SOBRE O PAPEL DA GIRO-RESSONÂNCIA NO GRADIENTE DE TEMPERATURA DE BRILHO EM 17 GHZ DE REGIÕES ATIVAS SOLARES

RESUMO

O controle da temperatura de brilho (T_b) em rádio liderada pela giro-ressonância proveniente de regiões ativas é um fato reconhecido por vários autores nas últimas décadas. No entanto, até o presente trabalho, não havia clareza sobre a relação entre esse mecanismo de rádio e o gradiente de temperatura de brilho ($\vec{\nabla}T_b$). Além disso, a associação direta da intensidade de campos magnéticos específicos com a opacidade do meio afetado por elétrons giro-ressonantes levou este trabalho a considerar o controle magnético não apenas do brilho em rádio, mas também do seu gradiente. A demonstração desse controle pode, portanto, servir para identificar melhor as fontes de giro-ressonância. Assim, entre os magnetogramas *HMI* do *Solar Dynamics Observatory (SDO)*, este trabalho selecionou 8 grandes regiões ativas da 1ª metade do 24º ciclo solar. Correspondentes a essas regiões selecionadas, foram também obtidos mapas de 17 GHz sintetizados pelo *Nobeyama Radioheliograph (NoRH)*. Analisamos, então, cada região ativa através dos seus dados simultâneos: campo magnético fotosférico e brilho em 17 GHz. Para cada região ativa, após ajustarmos os magnetogramas com os mapas de brilho (ambos com poucos minutos de diferença), verificamos que os contornos de intensidade dos campos magnéticos associados aos 3º e 4º harmônicos da giro-frequência para 17 GHz são parcial ou totalmente envolvidos por saltos de brilho. Tais intensificações de emissão foram identificadas tanto por mapas BT, com uma distribuição da temperatura de brilho, como por mapas BTG, com um campo de gradiente de temperatura de brilho. Em ambos os tipos de mapas, a maioria das regiões de forte salto de brilho exibem uma morfologia (semi) circular de contornos de brilho e um intenso grau de polarização circular (r_c) de módulo acima de 30%, caracterizando uma fonte de giro-ressonância. Também verificamos que tanto T_b quanto $|\vec{\nabla}T_b|$ estão fortemente correlacionados com $|r_c| \geq 30\%$ na maioria dos casos, enquanto sua correlação com $|r_c| < 30\%$ pode ser geralmente classificada entre fraca e moderada. Durante a ocorrência de flares e/ou em momentos próximos a tal evento, a correlação entre essas variáveis de brilho com $|r_c| \geq 30\%$ tende a cair, chegando a assumir valores fracos ou moderados. Mesmo nestas condições, os bumps permaneceram com um alto grau de polarização circular, abrindo a possibilidade para a influência conjunta de outro(s) mecanismo(s) de emissão não investigado(s) neste trabalho. A presente tese também encontrou destacadas elevações de brilho sem alto grau de polarização e fora da influência de flares, o que consideramos como efeito do *bremsstrahlung*, dada a intensificação de choques de portadores de carga num plasma confinado em fortes campos magnéticos. No entanto, considerando as altas correlações associadas a elevações de brilho altamente polarizado com campos magnéticos correspondentes à giro-ressonância, este trabalho foi capaz demonstrar o predominante papel de tal mecanismo de rádio sobre o processo de intensificação de brilho em 17 GHz.

Palavras-chave: Giro-ressonância. Regiões ativas. Bremsstrahlung. Grau de polarização circular. Gradiente de temperatura de brilho.

LIST OF FIGURES

Page

LIST OF TABLES

Page

LIST OF ABBREVIATIONS

ALMA	–	Atacama Large Millimeter/submillimeter Array.
BIMA	–	Berkeley-Illinois-Maryland Array.
BT map	–	Map of brightness temperature.
BTG map	–	Map of the brightness temperature gradient.
CME	–	coronal mass ejection.
EOVSA	–	Expanded Owens Valley Solar Array.
FITS	–	Flexible Image Transport System.
NAOJ	–	National Astronomical Observatory of Japan.
NASA	–	National Aeronautics and Space Administration.
NoRH	–	Nobeyama Radioheliograph.
NOAA	–	National Oceanic and Atmospheric Administration.
NRAO	–	National Radio Astronomy Observatory.
NRO	–	Nobeyama Radio Observatory.
NSRO	–	Nobeyama Solar Radio Observatory.
GHz	–	Gigahertz.
HMI	–	Helioseismic and Magnetic Imager.
HSC	–	Hinode Science Center Project.
ICCON	–	International Consortium for Continued Operation of Nobeyama Radioheliograph.
IDL®	–	Interactive Data Language.
ISEE	–	Institute for Space-Earth Environmental Research.
LHCP	–	Left-hand circular polarization.
LOS	–	Line of sight.
NU	–	Nagoya University.
RHCP	–	Right-hand circular polarization.
SDO	–	Solar Dynamics Observatory.
SSW	–	SolarSoftWare.
USA	–	United States of America.
UT	–	Universal Time.
VLA	–	Very Large Array.
WSRT	–	Westerbork Synthesis Radio Telescope.

LIST OF SYMBOLS

ω	–	angular frequency.
T_b	–	brightness temperature.
$T_b^{(L)}$	–	Brightness temperature of left-hand circular polarization.
$T_b^{(R)}$	–	Brightness temperature of right-hand circular polarization.
$\vec{\nabla} T_b$	–	brightness temperature gradient.
$\vec{\nabla} T_b^{(L)}$	–	Brightness temperature gradient of left-hand circular polarization.
$\vec{\nabla} T_b^{(R)}$	–	Brightness temperature gradient of right-hand circular polarization.
k_B	–	Boltzmann constant.
r_c	–	circular polarization degree.
$\vec{j}$	–	current density.
ν	–	emission frequency.
$\vec{E}$	–	electric field.
σ_0	–	electrical condutivity.
ν_B	–	emission gyrofrequency.
T_{eff}	–	effective temperature.
m_e	–	electron mass.
Ω_e	–	fundamental angular frequency.
κ_ν	–	absorption coefficient according to emission frequency.
j_ν	–	emission coefficient according to emission frequency.
s	–	harmonic level of the gyrofrequency.
$v_{\|\|}$	–	longitudinal component module of electron velocity.
$k_{\|\|}$	–	longitudinal component of wave vector.
γ	–	Lorentz factor.
$\vec{B}$	–	magnetic field.
η	–	magnetic diffusivity.
n	–	number density.
τ_ν	–	opacity coefficient according to emission frequency.
S_ν	–	source function according to emission frequency.
β	–	plasma factor.
h	–	Planck constant.
I_ν	–	radiative intensity according to emission frequency.
c	–	speed of light in vacuum.

CONTENTS

Page

1 INTRODUCTION

Since the Carrington Event in 1859, when a large-scale disturbance in Earth's magnetic field caused damage to a considerable part of Europe and North America's telegraph, the active regions have been seen as a potential source of loss in the electrical systems. Some hours before this event, the astronomers R. C. Carrington and R. Hodgson noted, in the solar disk, a large sunspot associated with a big flare (CARRINGTON, 1859; HODGSON, 1859). Therefore, these observations explain the relation between that magnetic disturbance and active region, expressed by the sunspot through the visible light. Nowadays, the human being has much more to lose during an occurrence of another event of similar magnitude, including resulting problems in pipelines, satellites, GPS, high voltage webs, VHF communication, and so on, which would be an unreasonably greater impact in a civilization of incurable technological dependence.

This vulnerability has required research to understand the active regions to prevent and reduce its harmful effects. Following Carrington (1859) and Hodgson (1859), studies on solar activity and its environment have been developed, providing significant information and models describing how active regions work. The evolution of studies in this field of research has been driven by the advent and development of Sun observation equipment. Sensors of various bands installed in satellites, such as SDO (NASA, 2013b), SOHO, TRACE, RHESSI, Hinode, polarimeters, radio interferometers, among others, made it possible to verify the variety of other forms of radiation from the solar atmosphere (PORFIR'EVA; YAKUNINA, 2013; SHIMOJO; IWAI, 2023). Therefore, the restriction that existed until the mid-twentieth century to white-light observation has been overcome. The mechanisms of the solar atmosphere have become better understood through this new step.

By that time, observation of the Sun using its radio emission was in its very early stages. Supposedly, the first effort at this type of detection was carried out in the late 19th century by O. Lodge, who idealized radio waves coming from the Sun, which was confirmed by a radio frequency capture made by the Bell Laboratories in 1942 (HADDOCK, 1958). In the 1940s, in addition to discovering that the Sun is a potential emitter of radio waves (ASCHWANDEN, 2006), sunspots were found to be intense sources of polarized radio emission (APPLETON EV & HEY, 1946). Since active regions are sources of intense radio emissions (COVINGTON, 1947; VOURLIDAS et al.,2006), the use of radio waves is an important means for the study of such magnetic structures.

One of the radio manifestations is gyroresonance radiation, which is best explained in Chapter 3. Following first Zheleznyakov (1962) and Kakinuma and Swarup (1962), we can state that gyroresonance emission comes from sunspots. Therefore, this kind of radiation is a unique mechanism of active regions in the solar atmosphere. According to Vourlidas et al. (2006), this emission is the principal means of estimating the magnetic field of the solar upper atmosphere. In his review, White and Kundu (1997) show the advantageous property possessed by this radiation, of making corona opaque in a magnetic field between 20 and 2000 G. Due to this property, the identification of coronal regions emitting gyroresonant radiation would be viable (WHITE, 2004) and, according to Lee (2007), we can determine the temperature of the corona. Therefore, as explained in Chapter 3, gyroresonance emission has been useful to many authors in comprehending the magnetic nature of the solar atmosphere. The model presented by Selhorst et al. (2008) already highlights a close relationship between the brightness temperature from gyroresonant emission and the magnetic field in active regions. However, models are built on simplifications of nature. In this case, potential and force-free extrapolations consider scenarios where the local solar atmosphere has, respectively, the null current density in the photosphere and a huge magnetic force per unit area compared to the hydrostatic pressure gradient and the volume density of the gravitational force (ASCHWANDEN, 2006; SELHORST, 2007).

Through various works (*e.g.* GINZBURG; ZHELEZNYAKOV, 1961, ZHELEZNYAKOV, 1962), it has been noted the relevant role of multi-frequency gyroresonance on the opacity and temperature of the solar atmosphere at the height of the chromosphere, transition region, and corona base. On the other hand, until the present work, it has not been clear what role gyroresonance plays on the 17 GHz brightness bumps (Figure 1.1) revealed by maps synthesized by Nobeyama Radioheliograph (NoRH). The central question of this work lies in such bumps since other mechanisms, such as bremsstrahlung and gyrosynchrotron, could (and may) contribute to their emergence and maintenance since such radiative processes also affect the opacity of the medium. Hence, the line of research assumed by this thesis is on the relationship between gyroresonance and radio brightness intensification, shown by the brightness temperature gradient. For this research, the main objective was to provide a solution to the question: **Among the incoherent emission mechanisms, what is the order of importance of gyroresonance in controlling the 17 GHz brightness temperature increase?** Therefore, considering the characteristics of gyroresonance, the questions that this work is answering are as follows:

Figure 1.1 - Synthesized by NoRH, Figure (a) shows an image of the entire solar disk at 17 GHz, highlighting a brightness temperature bump inside the white square. As a result of the processing of Figure (a), Figure (b) is a close-up of the brightness temperature gradient of such a highlight.

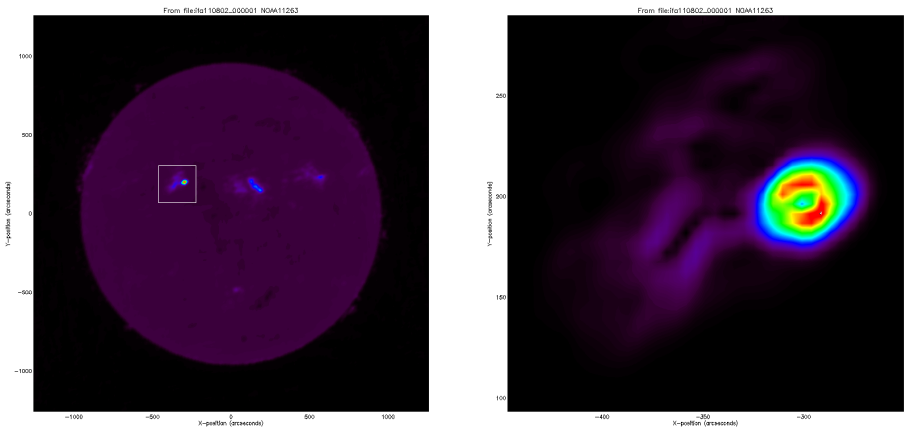

(a) (b)

Source: Figure (a): Adapted from NoRH (2011).

- In the 17 GHz maps of the analyzed active regions, do the brightness bumps have a degree of polarization corresponding to the gyroresonance emission?
- What level of correlation do the brightness temperature and its gradient have with the demarcating circular polarization modulus of the gyroresonance?
- During the occurrence of flares, characterized by the (almost) absence of the gyroresonance, what happens to such correlation?
- Is it possible to establish ranges of brightness temperature and its gradient that are useful for demarcating gyroresonance emission source(s)?
- Do such bumps coincide with specific magnetic fields of the gyroresonance at 17 GHz in the 3rd and 4th harmonics?

Answering such questions is motivated by making it possible to:

- Developing a technique to better estimate the magnetic field above the photosphere without magnetogram extrapolation, basically using brightness maps of highly polarized regions.

- To analyze the evolution of the magnetic field associated with the gyroresonance using the technique of the previous item.

In anticipation, then, of Chapters 5 and 6, focused on the procedures of this work and its results, respectively, the following Chapters address the state-of-the-art topics that support the understanding of this research. Thus, Chapter 2 briefly characterizes the solar atmosphere and its active regions; Chapter 3 deals with the incoherent radio mechanism developed by active regions; and Chapter 4 talks about instruments that are the sources of the data used in this work.

2 ON THE SOLAR ATMOSPHERE AND ITS ACTIVE REGIONS

To comprehend the solar mechanisms of radio emission, it is essential to understand the environment in which such processes take place and their boundary conditions. Depending on the combination of factors, such as magnetic field strength, temperature, and density, different regions of the solar atmosphere can become conducive to the occurrence of one of the different incoherent emission processes, which is best explained in Chapter 3. This chapter, therefore, briefly discusses these factors.

The most basic of radio emissions from the solar atmosphere occurs through a fundamental oscillation of the charges in the plasma at a frequency ν_p, which depends on the electron density n_e, so that $\nu_p = 8980\sqrt{n_e}$ (WHITE; KUNDU, 1997). As Dulk (1985) explained, if it reaches the value of ν_p, the frequency of shocks between particles of the same and opposite charge, which is driven by the temperature of the medium and the concentration of electrons, the oscillatory system goes into resonance, which can lead to the transformation of part of the thermal energy into coherent emission.

Bremsstrahlung and gyro emissions are mechanisms associated with the adherence of the solar plasma to the magnetic field. This implies that such radiation mechanisms are best provided in an environment with a higher concentration of electrons around magnetic field lines. This concentration of electrons depends on the balance between the thermal pressure $p_{th} = nk_BT$ and the magnetic pressure $p_B = B^2/(8\pi)$, which defines the plasma factor $\beta = p_{th}/p_B$ (considering that n is the number density of electrons, k_B is the constant of Boltzmann, T indicates the temperature, while B is the strength of magnetic field), and thus, in the condition where $p_{th} << p_B$ ($\beta << 1$), electrons are much more cohesive to magnetic field lines than in an opposite situation, where $\beta >> 1$ (ASCHWANDEN, 2002). Considering the definition of the β factor, the value of such an index can be obtained by the relation:

$$\beta = 8\pi k_B nT/B^2. \tag{2.1}$$

2.1 The solar atmosphere as frozen plasma

The solar atmosphere is a plasma immersed in a magnetic field, and such magnetic adhesion of the electrons in the medium is predicted by the theory of plasma freezing

to the field lines. The formalism of this theory is based on generalized Ohm's law:

$$\vec{j} = \sigma_0 \left[\vec{E} + \left(\vec{U} \times \vec{B} \right) / c \right], \tag{2.2}$$

considering that $\vec{j}$ is current density, σ_0 is the electrical conductivity reduced to a scalar form, $\vec{E}$ is the intrinsic electric field, $\vec{U}$ is the velocity of a moving cloud of plasma immersed in a magnetic field $\vec{B}$. From the perspective of a referential moving with the same velocity $\vec{U}$, the vector $\vec{U} \times \vec{B}$ equals an electric field. By applying the rotational operator $(\vec{\nabla}\times)$ to Equation 2.2, we have:

$$\vec{\nabla} \times \vec{j} = \sigma_0 \left[\vec{\nabla} \times \vec{E} + \vec{\nabla} \times (\vec{U} \times \vec{B})/c \right]. \tag{2.3}$$

Considering, then, Faraday's law $\left(\vec{\nabla} \times \vec{E} = -\frac{1}{c} \frac{\partial \vec{B}}{\partial t} \right)$ and Ampère's law $\left(\vec{\nabla} \times \vec{B} = 4\pi \vec{j}/c \right)$, we have:

$$\frac{c}{4\pi\sigma_0} \vec{\nabla} \times \left(\vec{\nabla} \times \vec{B} \right) = -\frac{1}{c} \frac{\partial \vec{B}}{\partial t} + \vec{\nabla} \times \left(\vec{U} \times \vec{B} \right) / c. \tag{2.4}$$

By swapping the first two terms in place and then applying the vector identity $\vec{\nabla} \times (\vec{\nabla} \times \vec{B}) = \vec{\nabla}(\vec{\nabla} \cdot \vec{B}) - \vec{\nabla}^2 \vec{B}$, considering Gauss's law of magnetism $\left(\vec{\nabla} \cdot \vec{B} = 0 \right)$ and $\eta = \frac{c^2}{4\pi\sigma_0}$ as magnetic diffusivity, we then have the induction equation:

$$\frac{\partial \vec{B}}{\partial t} = \eta \vec{\nabla}^2 \vec{B} + \vec{\nabla} \times \left(\vec{U} \times \vec{B} \right). \tag{2.5}$$

Its interpretation must consider whether one of the terms arranged to the right of the equal sign is much larger than the other so that, under this condition, the term in advantage is dominant. If this is the case for the first term, then the Equation 2.5 is deduced to the diffusion equation:

$$\frac{\partial \vec{B}}{\partial t} \simeq \eta \nabla^2 \vec{B}, \tag{2.6}$$

indicating that, in this case, the lines of a magnetic field diffuse into the plasma. For the same spatial coordinate of the plasma, $\vec{B}$ changes with time. On the other hand, if the second term of the Equation 2.5 is much larger than the first term, the same equation is reduced to:

$$\frac{\partial \vec{B}}{\partial t} \simeq \vec{\nabla} \times \left(\vec{U} \times \vec{B} \right), \tag{2.7}$$

meaning that for an observer with the same velocity ($\vec{U}$) of a magnetized plasma mass, $\vec{B}$ does not vary in time, which defines the condition of freezing of magnetic field lines to the plasma. Since the magnetic diffusivity η (in the Equations 2.5 and 2.6) is inversely proportional to the electrical conductivity σ_0, highly conductive plasma clouds are environments conducive to freezing.

The demonstration of Equations 2.5, 2.6, and 2.7, as well as their discussion and meanings, corroborates with the textbook by Mullan (2009), in which it is also discussed that the diffusion Equation (2.6) predicts results that are wildly divergent from the observed magnetic field fading time of active regions. Applying to the solar atmosphere case means that Equation 2.7 is a more appropriate approximation, which predicts plasma freezing and thus considerable cohesion between electrons and magnetic field lines.

2.2 Stratification of the solar atmosphere

The profile of the solar atmosphere has led it to be subdivided into the following layers: photosphere, chromosphere, and corona. Given its steep temperature curve, the transition region between the last two strata has been the subject of special attention, which can also give it the status of a layer. This division is not strictly based on the height range at which these layers are found, which depends on the local magnetic field strength but is based on their characteristics that vary in the vertical dimension (PRIEST, 2014). As suggested by the temperature profile described by Vernazza et al. (1981), and better presented by Yang et al. (2009) (Figure 2.1), the solar-atmospheric strata are thus fundamentally characterized: the photosphere is mainly defined by a drop in its temperature as height increases, marking its upper edge around 460 km height, where its minimum temperature occurs; from that point on, the chromosphere begins, with an almost exponentially increasing temperature profile over 1400 km height until the temperature growth rate becomes profoundly accentuated, characterizing the transition region; the corona, in turn, begins at the inflection point of this sharp profile.

For each layer, Avrett and Loeser (2008) presented a model with several parameters, including temperature and plasma density, according to height. In this model, then, up to a height of 450 km, the temperature decreases from 6583 to 4485 K, and the hydrogen[1] density decreases from 1.188×10^{17} to 4.324×10^{15} cm^{-3}; between 450 and 1722 km height, the temperature increases and reaches 6643 K, while the

[1]Hydrogen is the element that is proportionally most present in the solar plasma.

hydrogen density continues to decrease, reaching 2.864 $\times$ 10^{11} cm^{-3}; from 1750 to 11596.2 km the temperature continues to rise until it reaches 865000 K, while the electron density, in decline, reaches 2.667 $\times$ 10^{8} cm^{-3}. The photosphere is the layer with the strongest magnetic fields in the solar atmosphere, commonly around 300 G in the quiet regions (KHOMENKO et al., 2003), followed by the chromosphere, typically between 40 and 200 G (BOGOD et al. 2015), and the corona with fields in the tens of Gauss scale (LIN et al., 2000; PRIEST, 2014). Taking Equation 2.1 and the data presented in this paragraph, then, we can verify that: at the base of the photosphere, with $B = 300$ G, $\beta = 30.2$, becoming 1.68 at the boundary with the chromosphere, considering $B = 200$ G; at the top of the chromosphere, with $B = 40$ G, we have $\beta = 0.041$; and in the corona, assuming $B \sim 10$ G, we have $\beta = 5.8 \times 10^{-6}$.

Figure 2.1 - Solar atmosphere profile (YANG et al., 2009).

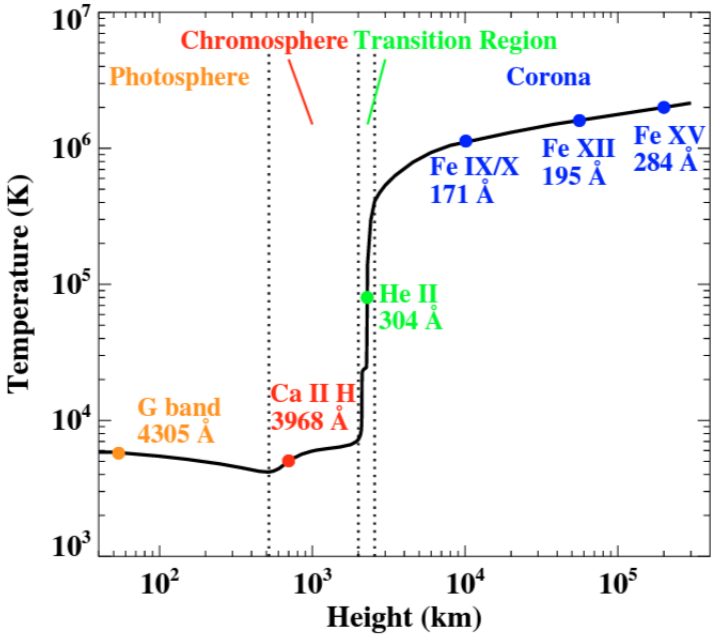

Source: Yang et al. (2009).

Such results, therefore, indicate that at the base of the photosphere, the plasma is dominated by the thermal pressure p_{th} against the magnetic pressure p_B; at the transition from the photosphere to the chromosphere, p_{th} has a small advantage over p_B, which does not characterize dominance of some of these pressures; at the transition from the chromosphere to the corona, until its top, the magnetic pressure is locally

dominant. Taking numerical density, temperature, and magnetic field strength data characteristic of several other intermediate heights of the solar atmosphere, we can see that $\beta >> 1$ in the photosphere, while $\beta << 1$ in the chromosphere, the transition region, and at the base of the corona (see Figure 2.2) (ASCHWANDEN, 2006; PRIEST, 2014). This makes the upper layers the best-conditioned environments for developing gyro emission mechanisms.

Figure 2.2 - Plasma β profile (ASCHWANDEN, 2006).

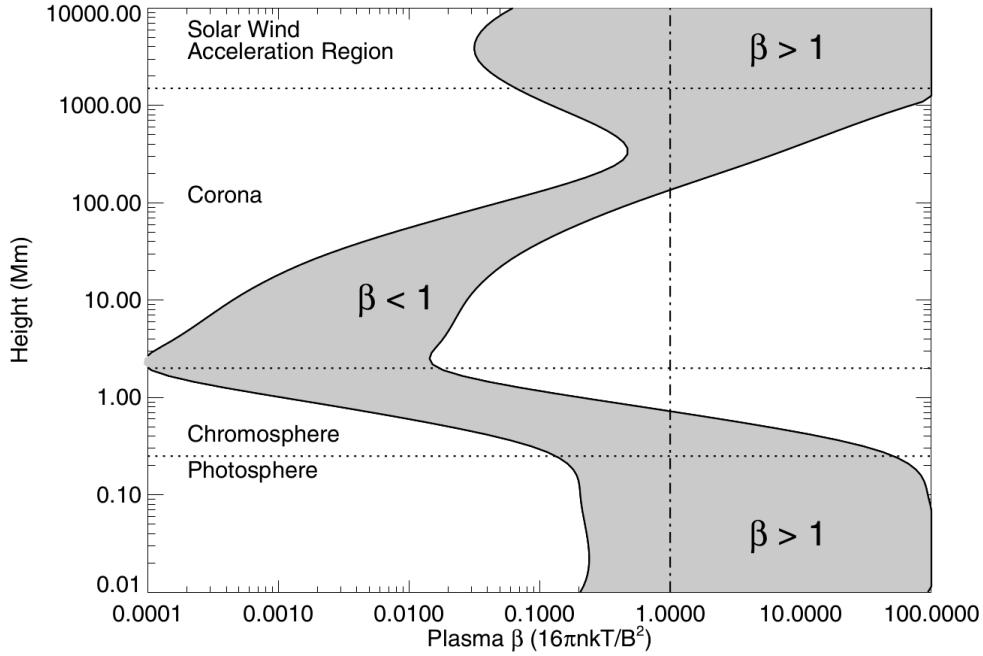

Source: Aschwanden (2006).

Due to its high density, thermal pressure dominance occurs in the photosphere despite strong magnetic fields and a much lower temperature than in the last layer. In the corona, the predominance of magnetic pressure is mainly due to the very low local density, which compensates for the very high temperature and low magnetic field strength.

2.3 On the active regions

According to Kiepenheuer (1968), an active region is a set of all phenomena, seen in white light, EUV, radio, and X-ray, involving the appearance of sunspots (see Figure 2.3). From this definition and based on multi-band observations, Driel-Gesztelyi and

Green (2015) extended the range of frequencies in which such phenomena can be observed to the entire electromagnetic spectrum. Priest (2014) described the active regions as one type of magnetic manifestation among others of different intensities of the photosphere. For him, active regions are magnetic structures whose flux can reach 10^{23} Mx[2] and whose appearance happens with convection inhibition and without the need for supergranules. According to Driel-Gesztelyi and Green (2015), the minimum flux for an active region is 10^{20} Mx.

Figure 2.3 - The arched lines shown in Figure (a), an image at 171 Å obtained by SDO (NASA, 2023), and depicted in Figure (b) (KONTAR et al., 2017) exemplify well the occurrence of active regions in the solar atmosphere.

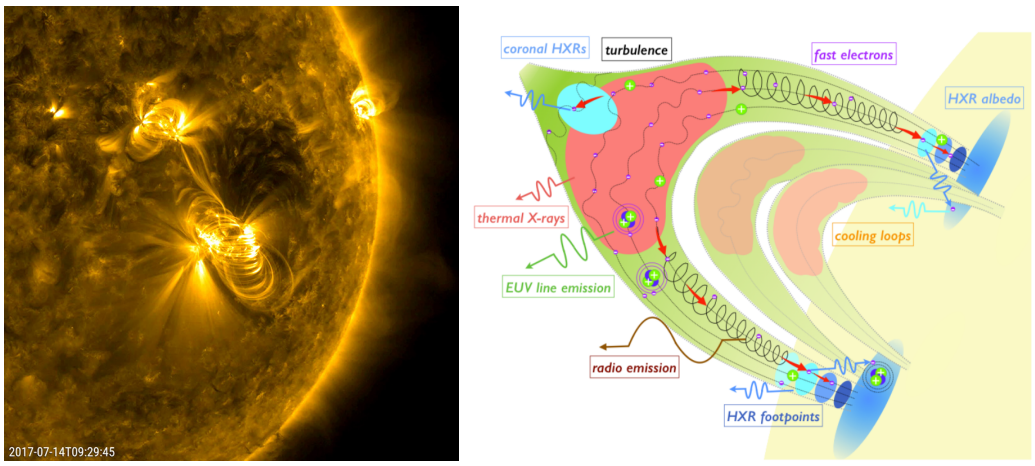

(a) (b)

Source: Figure (a): NASA (2023); Figure (b): Kontar et al. (2017).

Combining such definitions and characteristics, we can state that active regions are tubes of intense magnetic flux emerging from the photosphere, usually with a magnetic field strong enough to inhibit local photosphere convection in such a way as to create sunspots. However, as shown by Selhorst et al. (2014), it is possible to find active regions that do not produce sunspots, given possible not-so-intense magnetic field conditions in the flux tube. Both ends of these magnetic emanations are usually concentrated where sunspots are located (DRIEL-GESZTELYI; GREEN, 2015). Therefore, sunspots are the magnetic poles of active regions.

The appearance of active regions is directly associated with the 11-year solar cycle, in which the solar magnetic field in its dipolar form is reversed. In this reversal

[2]Mx (Maxwell) is the unit in cgs for magnetic flux and is equivalent to 1 G cm^2.

process, the magnetic field lines, frozen to the solar plasma, are deformed due to the Sun's differential rotation, which leads to the torsion of these lines, resulting in the outcropping of arcuate flux tubes in the solar atmosphere. The twisting experienced by the field lines contributes to the accumulation of a large amount of energy, whose release, which occurs through reconnection, results in coronal mass ejection (CME) and the occurrence of flares (BENZ, 2016).

3 INCOHERENT RADIO MECHANISMS DEVELOPED BY ACTIVE REGIONS

As presented in the previous Chapter, active regions are magnetic manifestations of the solar atmosphere and such an environment, as well as in stars of the same kind (framed in the main sequence[1]) is highly capable of developing radio emission mechanisms that fall into two broad classifications: coherent, which groups plasma emission and electron-cyclotron maser, and incoherent, which includes free-free bremsstrahlung and the thermal gyro emissions (DULK, 1985; ASCHWANDEN, 2002). Originally, coherent emissions are considered to be waves that propagate in phase (GANGADHARA et al., 2021), unlike incoherent emissions. The free-free bremsstrahlung process is based on the collision between electrons and nuclei of atoms, in which each electron is as free before the collision as it is after. At the same time, the gyro emission occurs through the spiraling motion of electrons around magnetic field lines (NINDOS, 2020).

Among the gyro emissions, we can find, as described by Dulk (1985): the synchrotron, of high energy ($\gamma >> 1$)[2]; the gyrosynchrotron, of moderate energy ($1 < \gamma < 3$); and gyroresonance, whose power is considered low ($\gamma \simeq 1$). Due to this low energy characteristic, the density of gyroresonance emission source electrons is commonly described by a thermal distribution, meaning that the electrons from the emission source have no predominant direction. Emissions originating in the bremsstrahlung can also be of thermal origin. The environment conducive to the development of these last two mechanisms has therefore been described from their Maxwellian distribution, although different distributions have been presented (FLEISHMAN; KUZNETSOV, 2014).

For a given frequency ν, the data obtained from such emission processes occur by reading its radiative intensity I_ν, defined as the signal strength (measured in erg s^{-1}) per unit area (cm^2), radiation frequency (Hz) and solid angle (ster) (RYBICKI; LIGHTMAN, 1991). The detection of I_ν, then, must consider that the detected radiation has passed through plasma clouds capable, at least partially, of absorbing and re-emitting the energy of that radiation, which gives such a medium absorption coefficient κ_ν and emission coefficient j_ν, leading to the equation of the radiation

[1] In the Hertzsprung-Russell (H-R) Diagram, which defines the spectral class of stars, the main sequence groups all stars that maintain their hydrostatic equilibrium through the thermonuclear fusion of Hydrogen. The Sun holds its own in this stellar classification.

[2] γ is the Lorentz Factor $\left(1/\sqrt{1 - v^2/c^2}\right)$, which is high ($>> 1$) when the speed v is around the speed of light c, while it is low when the speed v represents a very low percentage of the speed of light c.

transfer rate through the l path to the observer (DULK, 1985; NINDOS, 2020):

$$\frac{dI_\nu}{dl} = -\kappa_\nu I_\nu + j_\nu. \tag{3.1}$$

The absorption coefficient (κ_ν) of the propagation medium indicates how much of the power I_ν (of the signal) is absorbed per unit length along the path within such a medium. In the cgs system, such an index is expressed in cm^{-1}. The emission coefficient (j_ν) indicates the derivative of I_ν with respect to the length of that path, so its unit in the cgs system is erg s^{-1} cm^{-1}. The integration of the absorption coefficient along the path of the radiation beam in the propagation medium defines the opacity τ_ν, also known as optical depth (τ_ν=$\int \kappa_\nu dl$), which contributes significantly to the brightness temperature (T_b) of such medium, given the principle of blackbody radiation that the higher the absorption, the higher its temperature and emission. A given medium can be optically thin (transparent) or thin (opaque) for a given frequency. Depending on the propagation medium, such a classification can also be given to the radiation.

Considering, then, the meanings of the coefficients in Equation 3.1, it can be given by:

$$\frac{dI_\nu}{d\tau_\nu} = -I_\nu + S_\nu, \tag{3.2}$$

where $S_\nu = j_\nu/\kappa_\nu$, called the source function, is an index that indicates how much of the absorbed radiation was emitted. For a uniform medium, taking S_ν as a constant, Equation 3.2 implies that[3]

$$I_\nu = I_0 e^{-\tau_\nu} + \left(1 - e^{-\tau_\nu}\right) S_\nu, \tag{3.3}$$

where I_0 is the signal strength at the source location, while I_ν is the measurement made by the observer. Once the I_ν value is obtained, the brightness temperature T_b can be calculated. The relationship between such quantities can be given by Planck's Equation (3.4) in the case where the propagating medium has a condition close to that of a blackbody, where the absorbed energy is approximately equal to the emitted energy. In such an equation, then, I_ν is given by (PLANCK, 1900):

$$I_\nu(T_b) = 2\frac{h\nu^3}{c^2}\frac{1}{exp\left(\frac{h\nu}{k_B T_b}\right) - 1}, \tag{3.4}$$

[3]The solution 3.3 can be demonstrated by the Laplace transform applied to Equation 3.2: $\mathcal{L}\{I'_\nu\}$=-$\mathcal{L}\{I_\nu\}$+$\mathcal{L}\{S_\nu\}$ $\Rightarrow$ $s\mathcal{L}\{I_\nu\}$-I_0=-$\mathcal{L}\{I_\nu\}$+S_ν/s $\Rightarrow$ $(s+1)\mathcal{L}\{I_\nu\}$=$I_0$+$S_\nu/s$ $\Rightarrow$ $\mathcal{L}\{I_\nu\}$=$(I_0$+$S_\nu/s)/(s+1)$ $\Rightarrow$ I_ν=$\mathcal{L}^{-1}\{(I_0$+$S_\nu/s)/(s+1)\}$.

where h and k_B are, respectively, the constants of Planck and Boltzmann, while c is the speed of light in a vacuum. Considering the MacLaurin series expression for $exp\left(\frac{h\nu}{k_B T_b}\right) - 1$,

$$exp\left(\frac{h\nu}{k_B T_b}\right) - 1 = \frac{h\nu}{k_B T_b} + \frac{1}{2!}\left(\frac{h\nu}{k_B T_b}\right)^2 + \frac{1}{3!}\left(\frac{h\nu}{k_B T_b}\right)^3 + ..., \tag{3.5}$$

the terms of order ≥ 2 are negligible under the condition that $k_B T_b >> h\nu$, leading to $exp\left(\frac{h\nu}{k_B T_b}\right) - 1 \approx \frac{h\nu}{k_B T_b}$. Then, Equation 3.4 can be written as:

$$I_\nu(T_b) = 2\frac{\nu^2}{c^2} k_B T_b. \tag{3.6}$$

If the propagating medium can be considered an ideal blackbody, the brightness temperature will equal the local effective temperature (T_{eff}). Otherwise, if the condition of such a medium can be approximated to the blackbody model, one can consider that the local opacity does not affect the propagating signal strength: $dI_\nu/d\tau_\nu \approx 0$. Assuming this approximation, Equation 3.2 implies that $I_\nu \approx S_\nu$. Since the brightness temperature is information obtained from the signal I_ν and the local effective temperature is a datum intrinsic to the medium, such an approximation implies that:

$$S_\nu(T_{eff}) = 2\frac{\nu^2}{c^2} k_B T_{eff} \tag{3.7}$$

Applying then Equations 3.6 and 3.7 to Equation 3.2, one has:

$$\frac{dT_b}{d\tau_\nu} = -T_b + T_{eff}. \tag{3.8}$$

Thus, since Equation 3.3 is a solution of Equation 3.2, Equation 3.8 results in:

$$T_b = \left(1 - e^{-\tau_\nu}\right) T_{eff}. \tag{3.9}$$

Performing MacLaurin's series expansion of $(1 - e^{-\tau_\nu})$, one has:

$$1 - e^{-\tau_\nu} = \tau_\nu - \frac{1}{2!}\tau_\nu^2 + \frac{1}{3!}\tau_\nu^3 + ..., \tag{3.10}$$

so that the terms of order $\geq$ two can be disregarded in the case where $\tau << 1$, characterizing an optically thin medium, leading to the approximation $(1 - e^{-\tau_\nu}) \approx \tau_\nu$ and thus $T_b = \tau_\nu T_{eff}$. On the other hand, in the case where $\tau >> 1$, characterizing an optically thick medium, the exponential term practically cancels out, and thus $(1 - e^{-\tau_\nu}) \approx 1$, leading to $T_b = T_{eff}$. Considering that each emission mechanism has

its particular opacity for a given set of conditions in a medium, an opaque plasma cloud will provide different brightness temperature profiles for a given effective temperature, depending on the radiation process considered.

This session's mathematical construction is corroborated by Dulk (1985) and Nindos (2020).

Another important characteristic of radio emission is its circular polarization, which is also a fundamental data class in this work, as is explained further on. Circular polarization refers to the angular orientation of the electromagnetic vector of the emission, which may be left-hand or right-hand and can originate in the rotating motion of the charge carrier around the magnetic field line. If the wave vector is pointed toward the observer, the left-hand direction means clockwise, while the right-hand sense implies counterclockwise. Conversely, in the case where the wave vector is pointing in the backward direction of the observer, left-hand sense indicates clockwise, while right-hand sense is the same as clockwise. Circular polarization defines the modes of propagation, which can be ordinary (O) or extraordinary (X). In the O mode, the angular orientation of the electromagnetic vector is contrary to the direction of rotation of the spiraling electron around the magnetic field line, while in the X mode, both directions are the same (WHITE; KUNDU, 1997).

According to Lee (2007), NRO (2013) and ICCON (2015), the degree of circular polarization can be obtained by the equation:

$$r_c = \left(T_b^{(R)} - T_b^{(L)}\right) / \left(T_b^{(R)} + T_b^{(L)}\right), \tag{3.11}$$

where $T_b^{(R)}$ and $T_b^{(L)}$ are the brightness temperatures for its right-hand and left-hand polarization, respectively. According to DULK (1985), r_c can be associated with the quotient between the emission frequency ν and the gyrofrequency ν_B, depending also on the tilt angle (θ) between the observer's line of sight and the magnetic field line:

$$r_c \approx 2\frac{\nu_B}{\nu} cos\theta, \tag{3.12}$$

implying that for a given constant ν_B/ν, the degree of circular polarization decreases with increasing tilt. The gyrofrequency ν_B results from the interaction of the magnetic field $\vec{B}$ with the moving electric charge $e = 4.80 \times 10^{-10}$ cm$^{3/2}$ g$^{1/2}$ of mass $m_e = 9.11 \times 10^{-28}$ g, so that the fundamental angular frequency Ω_e is given by (DULK, 1985):

$$\Omega_e = 2\pi\nu_B = \frac{eB}{m_e c} \simeq 1.76 \times 10^7 B, \tag{3.13}$$

considering $c = 3.00 \times 10^{10}$ cm s^{-1} and that B is given in Gauss unit.

3.1 The solar bremsstrahlung

Among the mechanisms of radio emission, bremsstrahlung is the predominant one in quiet Sun conditions, i.e., in the regions of the solar atmosphere without the occurrence of flares or CMEs. The relation of such a mechanism to the magnetic field, not as close as in gyroresonance, can be understood through the theory of freezing of magnetic field lines in the plasma of the solar atmosphere (see the Section 2.1): the stronger the magnetic field, the higher the concentration of electrons cohesive to such lines, and therefore the higher the frequency of shocks between electrons and ions. Therefore, this mechanism is expected to cause subtle spikes in the 17 GHz brightness temperature gradient at the edges of active regions. The opacity of the bremsstrahlung at frequencies above 3 GHz is low where the magnetic field strength is less than 400 G, becoming quite significant where such magnetic intensity is higher (NINDOS, 2020).

3.2 The solar gyroresonance

When electrons accelerate around magnetic field lines, they produce circularly polarized radiation. By interacting with other gyromagnetic electrons, the electric field of this radiation can attenuate or intensify its gyrofrequency, depending on the sense of the transverse[4] component of the electron velocity and the sense of the electric field. If they have the same sense, there will be deceleration; if they have opposite senses, there will be reinforcement in the gyrofrequency. In the latter situation, where the interaction radiation frequency approaches the electrons' gyrofrequency, the latter behaves like a forced harmonic oscillator at resonance. The gyroresonance emission is, therefore, the radiation produced by this resonant interaction, implying that the electron velocity and the wave vector of the interacting radiation have nonzero components in the direction of the magnetic field. Under this condition, the angular frequency ω of the electron is given by (MELROSE, 2017):

$$\omega = v_{||} k_{||} + s\frac{\Omega_e}{\gamma}, \tag{3.14}$$

assuming that $v_{||}$ and $k_{||}$ are the longitudinal[5] components of the electron velocity and the wave vector of the interacting radiation, respectively, and s is the natural number indicating the order of the fundamental gyrofrequency harmonic. The pres-

[4] Orthogonal to the magnetic field.
[5] Parallel to the magnetic field.

ence of the Lorentz factor (γ) in a denominator, in Equation 3.14, indicates that the second term is considered in the condition of low velocities, where $v << c$.

This emission mechanism is highly important in the study of the solar atmosphere, given its close relationship with magnetic fields from active regions and its high opacity at specific harmonics s, meaning that the susceptibility of the propagation medium to radiative absorption and influence on the local brightness temperature occurs for frequencies ν with values equal to integer multiples of the gyrofrequency (ν_B) (WHITE, 2004):

$$\nu = s\nu_B. \tag{3.15}$$

Such a fact means that in the solar atmosphere, the medium between the gyroresonant source and the observer tends to be much brighter at these specific frequencies and, therefore, detectable. This characteristic, which marks the association of gyroresonance with its propagation medium populated by thermal electrons, gives this radio mechanism a discrete power spectrum, unlike gyrosynchrotron radiation, whose spectrum is continuous. The opacity of the gyroresonance also depends on the inclination (θ) between the observation line and the magnetic field line (WHITE; KUNDU, 1997; VOURLIDAS et al., 2006; NINDOS, 2020). Such a relationship implies that an increase in this inclination tends to be accompanied by an increase in opacity, which can contribute to the rise in the brightness temperature. Considering only this relationship and Equation 3.12, the growth in the degree of polarization should occur while the brightness temperature decreases. If, on the other hand, the brightness temperature strongly correlates with the circular polarization modulus, then another factor, other than θ, controls the opacity. Considering Equation 3.12, this factor is probably the gyrofrequency (ν_B) in an analysis where ν is constant. In this case, given Equation 3.13, the magnetic field strength B is the variable whose growth results in the increase of the brightness temperature. In summary, therefore, for constant θ and ν, larger B leads to larger ν_B, which leads to larger r_c and larger T_b. Stronger magnetic fields result in greater electron acceleration, resulting in more intense radiation, corroborating with the theory of gyroresonance control over the brightness temperature in radio emission since such a mechanism is defined by the control of low-energy thermal electrons promoted by the magnetic field. Given the results presented by this work, this issue is of fundamental relevance in the discussions. However, in gyroresonance, such effects are observed only in discrete variations of ν_B and B.

Another important feature of gyroresonance lies in the fact that its sources are formed in higher layers, namely the chromosphere and transition region, where the

magnetic field is much less known than in the photosphere since $\beta << 1$ in such strata (ASCHWANDEN, 2002), as explained in Chapter 2.

Given such characteristics of gyroresonance, once one locates its sources, the magnetic field strength can be calculated in the following equation, deduced from the Equations 3.13 and 3.15, considering ν given in Hz and B in Gauss:

$$B = 3.57 \times 10^{-7} \nu / s. \tag{3.16}$$

According to this equation, considering a given frequency ν, each magnetic field line where B is constant and associated with the gyroresonance constitutes a layer identified by the sth harmonic of its electron gyrofrequency. Thus, assuming the magnetic field tends to decrease with height, the higher harmonic layers are those of higher order s. Models of gyroresonant emission sources, such as the one presented by White and Kundu (1997), indicate the distribution of such layers in an active region. According to these authors, the 2nd and 3rd harmonics usually produce a highly opaque X mode emission in the corona. However, in active regions, between the chromosphere and the base of the transition region, the 3rd and 4th harmonics are responsible for the gyroresonant emission that escapes from the solar atmosphere. The upper layers absorb the radiation originating from the 1st and 2nd harmonics, coming from deeper regions at stronger field strengths. Emissions from harmonics above the 4th are very weak.

3.3 Summary review of important steps in gyroresonance research

Solar gyroresonance first became noticeable in the years between the late 1950s and early 1960s, when Ginzburg and Zheleznyakov (1961) discussed the nature of a transient incoherent radio emission originating in a medium of high magnetic activity, such as in active regions. The authors highlighted the increased capacity of such (so far new) emission to be absorbed by the medium without considerably triggering a coherent mechanism in the plasma, characterizing an incoherent process.

Kakinuma and Swarup (1962) concluded the existence of the gyroresonance from the incompatibility of their results with the magneto-ionic model. Analyzing data from an interferometer calibrated for 2.8, 3.3, 4.0, and 9.4 GHz, they found that, contrary to what the model predicted, the power per unit area of the signal from various regions and its circular polarization index attenuate as the frequency increases below 10 GHz.

Zheleznyakov (1962), in turn, identified the strong relationship between 1.5-30 GHz gyroresonance from 2nd-3rd harmonic and specific characteristics of the propagation medium, such as temperature, the circular polarization direction, and the strong relationship between the emission frequency and the circular polarization index. According to the same paper, however, the dominance over radio emission can be assumed by the bremsstrahlung for frequencies below 1.5 GHz originating from a high electron density medium over radio sources in the 2nd-3rd harmonics since the participation of this mechanism in radio emission rises under such conditions.

Kundu et al. (1977) have shown a close relationship between the intensity of radio emission and its degree of polarization. They observed four active regions with the Westerbork Synthesis Radio Telescope (WSRT) at 6 cm wavelength (corresponding to 5.0 GHz). They obtained contour maps for the intensity I and for the degree of polarization r_c, respectively, by which it can be seen that the intensification of I is accompanied by an increase in r_c (see Figure 3.1).

Figure 3.1 - Maps of an active region at 6 cm, where we have the contours for the emission intensity in the Figure (a) and the contours for the circular polarization degree in the Figure (b) (KUNDU et al., 1977).

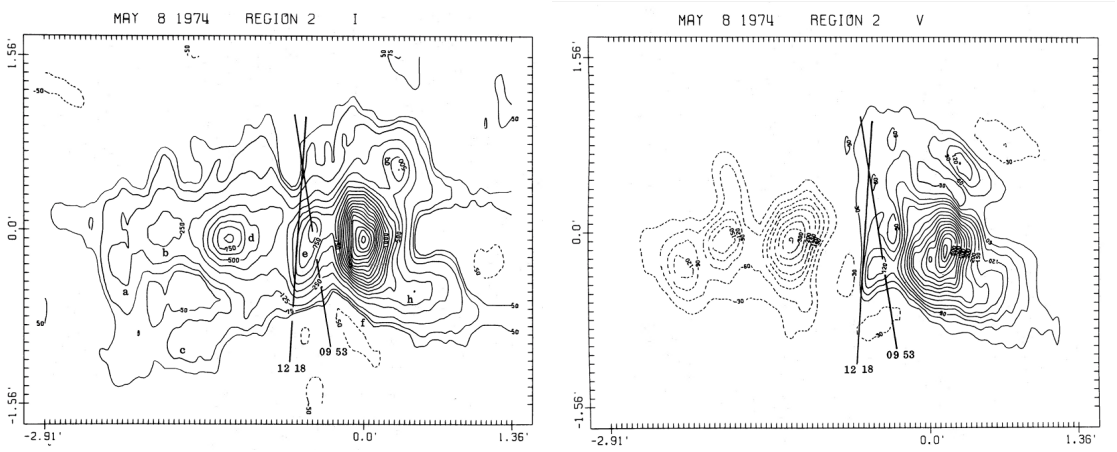

(a) (b)

Source: Kundu et al. (1977).

Similar to the previous work, Alissandrakis et al. (1980), using WSRT data, observed the intensity and polarization of the radiation at 6 cm from active regions. Using magnetogram extrapolation of these regions and radiative transfer calculations for bremsstrahlung and gyroresonance, they simulated the upper layers' temperature,

density, and magnetic field conditions to reconstruct the emission and polarization maps. The results of such a paper indicated that gyroresonance is primarily responsible for rebuilding the emission's intensity and circular polarization maps at 6 cm.

Also, analyzing the emission at 6 cm from active regions around the central meridian, Alissandrakis and Kundu (1982) observed the direct association between a ring morphology in the distribution of the detected radiation intensity and sunspots at Hα. For each observed active region, they plotted its emission intensity contours of such wavelength over its Hα images and magnetogram. The authors found that around the observed sunspots, the brightness temperature was increasing at the periphery of the intensity contours, while at the center, where the sunspots were located, the brightness temperature was decreasing (see Figures 3.2(a) and 3.2(b)). The authors interpreted this reduced brightness intensity in the central region of the contours as the result of a less optically thick gyroresonance in the sunspots due to the small (or zero) inclination between the magnetic field lines and the observation line.

Figure 3.2 - As explained by Alissandrakis and Kundu (1982), in the peripheral regions of the contours, the brightness temperature is increasing, but the central contours evidence a decrease in this variable over the observed sunspots.

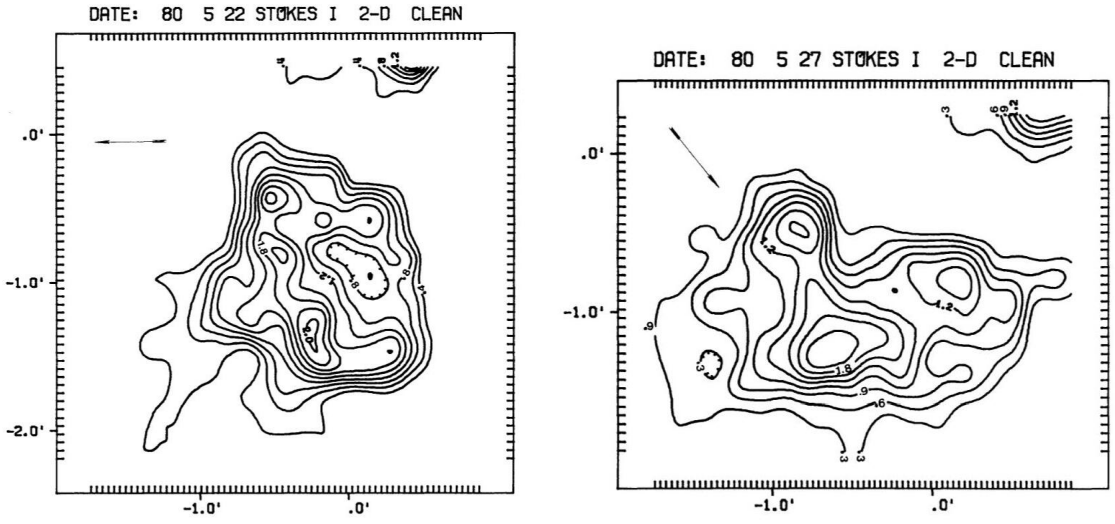

(a) (b)

Source: Alissandrakis and Kundu (1982).

Analysis of sunspot maps at 6 cm synthesized by WSRT was also performed by Lang

and Willson (1982). Some years earlier, like Kundu et al. (1977) and Alissandrakis et al. (1980), they had already identified regions of intensified and highly polarized radio emission and short angular extent that were directly associated with gyroresonance (LANG; WILLSON, 1979). By mapping brightness intensity contours, circular polarization, and magnetic field strength from the photosphere, Lang and Willson (1982) then identified in the polarization mapping a formation they called "horseshoe" characterized by a concavity between the contours (see Figure 3.3, dashed lines of map B). The authors also found that the observed emission from the horseshoe area, identified as the umbra of a sunspot, exhibited an extremely high-temperature peak on the scale of 10^6 K, surrounded by contours of lower temperatures in the area corresponding to the sunspot penumbra (see map A of Figure 3.3). As the authors themselves indicate, the inner area of the horseshoe, then, is not visibly polarized. However, the surrounding area exhibits degrees of polarization between 15% and 95%, which the authors interpret as solid evidence of gyroresonance (LANG; WILLSON, 1982). They further argue that the high-intensity peak is due to the longitudinal arrangement of the field lines over the umbra and its high magnetic intensity. According to the authors, this leads the emission from the 3rd harmonic to reach the corona, characterized by the highest temperature and lowest temperature gradient in the sunspot. The authors further explain that over the penumbra, the magnetic field is weaker and should form more veined lines so that the observed 3rd harmonic emission comes from lower heights, characterized by lower temperatures and higher temperature gradient than in the umbra.

Vourlidas et al. (2006) made significant findings about the relation of gyroresonance with its degree of polarization and the magnetic field for a given harmonic of the gyrofrequency. In their statistical analysis of the emission at 17 GHz from a sample of active regions, they found that at this frequency, gyroresonance is produced from the 3rd harmonic and can also be associated with the 2000 G magnetic field strength, and, furthermore, such a mechanism can be identified by its circular polarization degree modulus above 30%. Also, among the main results of these authors is the control that the tilt angle between the magnetic field and the observation line exerts on the opacity of the regions observed at 17 GHz.

Figure 3.3 - Mapping of the active region 3159: The contours indicate, according to Lang and Willson (1982), the levels of emission intensity at 6 cm in map A, circular polarization in map B, and magnetic field from photosphere in map C. Notice, in the dashed lines of map B, the outermost (and lowest level) contour forming a concavity called a "horseshoe" by the authors (LANG; WILLSON, 1982). Corroborating with them, looking at maps A, B, and C, notice also that in the area around the "horseshoe", the intensity of brightness intensifies towards the inner area, as does the magnetic field, whose modulus grows from 200 to 800 G (LANG; WILLSON, 1982).

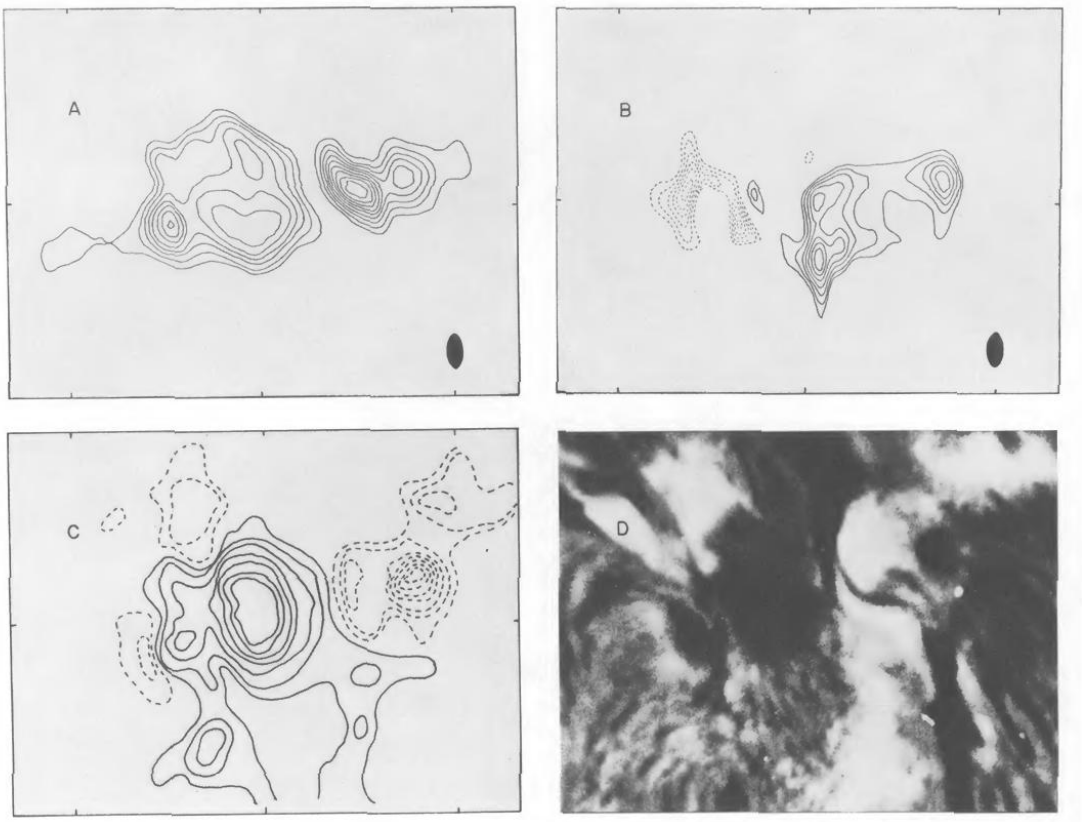

Source: Lang and Willson (1982).

Through their model of a high circular polarization index active region, using 17 and 34 GHz maps from the Nobeyama Radioheliograph (see Chapter 4), Selhorst et al. (2008) demonstrated the high susceptibility of factors such as electron density and brightness temperature to the magnetic field associated with gyroresonance. Using the radiative transfer equations and opacity coefficients for gyroresonance and bremsstrahlung, they verified such susceptibility by varying the α coefficient of the linear force-free equation ($\vec{\nabla} \times \vec{B} = \alpha \vec{B}$) in the MDI magnetogram extrapolation of region NOAA 10008. They carried out this procedure until they obtained a considerable approximation of this region's polarization, temperature, and den-

sity profiles. As explained by Aschwanden (2006) in his textbook, this method of reconstructing the magnetic field above the photosphere first assumes a hydrostatic equilibrium condition where the pressure gradient $\vec{\nabla}p$ and the force of gravity per unit volume $\rho\vec{g}$ are much smaller than the magnetic force per unit volume $\vec{j} \times \vec{B}$, so that the hydrostatic equilibrium equation, given by $-\vec{\nabla}p + \rho\vec{g} + \vec{j} \times \vec{B} = \vec{0}$, reduces to $\vec{j} \times \vec{B} = \vec{0}$, considering that p is the pressure of the medium, ρ is the density, $\vec{g}$ is the local gravitational acceleration, and $\vec{j}$ is the current density. Applying Ampère's law ($\vec{\nabla} \times \vec{B} = \mu_0\vec{j}$) to the latter equation, one has $(\vec{\nabla} \times \vec{B}) \times \vec{B} = \vec{0}$, which implies that $\vec{\nabla} \times \vec{B} = \alpha\vec{B}$, where α is a constant or variable value (ASCHWANDEN, 2006).

Similarly, Silva et al. (2022) used, from NoRH, 17 GHz maps, and, from ALMA radio interferometer, 100 and 230 GHz maps to develop a new model of an active region's electron distribution and temperature profile. They used a genetic algorithm to adjust the extrapolated magnetic field from an HMI/SDO magnetogram until they obtained a simulation satisfactorily close to the original maps, demonstrating the close relationship between the magnetic field and the radio brightness of an active region case.

4 THE NOBEYAMA RADIOHELIOGRAPH (NoRH)

The observation of the solar radio emission mechanisms presented in the previous Chapter required the development of apparatuses capable of receiving and filtering low-frequency signals from the Sun. One of the most practical techniques in radio (and optical) observation is interferometry, where several receivers act together as a single giant antenna (or telescope) to observe a target. Compared to using only one antenna/telescope, this technique can capture more power from the detected signal. It allows a higher-resolution reconstruction of the image of the observed object. In interferometry, each receiver is arranged so that the antenna/telescope array simultaneously picks up equivalent parts of the same wave emitted by the source since such parts are originally offset by an integer number of wavelengths of the sensed radiation (see Figure 4.1). The data received simultaneously by the array is then gathered in the correlator, which synthesizes the images (NAKAJIMA et al., 1994).

Figure 4.1 - Schematic of a radio image reconstruction from interferometry performed by an antenna array (SCHEDIWY, 2013).

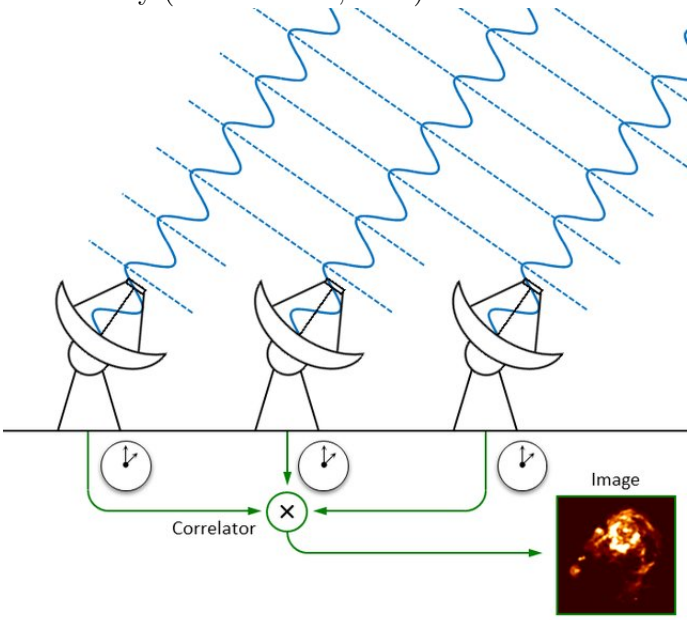

Source: Schediwy (2013).

In various places on the Planet, radio interferometers have been installed to observe the Sun at different frequency ranges, such as the Atacama Large Millime-

ter/submillimeter Array (ALMA), which operates at 35-950 GHz in Chile (SHIMOJO et al., 2017); the Berkeley-Illinois-Maryland Array (BIMA), at 100-250 GHz (LUGTEN, 1995) in California (USA) (WELCH et al., 1996); the Expanded Owens Valley Solar Array (EOVSA), at 1-18 GHz (EOVSA, 2023) in California (USA); the Nançay Radioheliograph, at 150-450 MHz (KERDRAON; DELOUIS, 1997) in France; the Nobeyama Radioheliograph (NoRH), at 17 and 34 GHz, in Japan (TAKANO et al., 1997); and the Very Large Array (VLA), at 1-50 GHz in New Mexico (USA) (NRAO, 2023). Each frequency band is more or less conducive to observing a particular layer of the solar atmosphere since higher frequencies are used to analyze deeper layers, as lower frequency emissions tend to fade more. The 17 GHz frequency, especially used by NoRH, is suitable for observing the layer where the gyroresonance develops. Moreover, gyroresonant radiation of such frequency is associated with relatively more accessible magnetic fields in magnetograms. The NoRH, therefore, is the instrument chosen by this work to obtain the radio maps of the analyzed active regions.

The NoRH data used in this thesis were produced at a time when this interferometer was controlled by the National Astronomical Observatory of Japan (NAOJ), a period that lasted until April 2015, when the International Consortium for Continued Operation of Nobeyama Radioheliograph (ICCON) took control of this instrument through direct action by the Institute for Space-Earth Environmental Research (ISEE) at Nagoya University (NU) (NSRO, NRO, NAOJ, 2015; HSC, ISEE, NU, ICCON, 2020). The supply of NoRH data continued to be provided by NAOJ after this transition of control (NSRO, NRO, NAOJ, 2015).

NoRH was installed in the Negano region (Japan) and started operating in 1992 as a T-shaped array (Figure 4.2) composed of 84 antennas of 80 cm diameter (each) spanning 220 m along the north-south axis and 490 m along the east-west axis, with a daily routine of observations of the Sun for eight consecutive hours, producing images of 10 arcsec spatial resolution every 50 ms containing brightness temperature data for right and left circular polarization (NAKAJIMA et al., 1994). The distribution of the antennas is 28 dishes for each branch starting from the center (see Figure 4.2) and follows the model of geometric growth of the distance in each pair, in which the closest dishes in the center of the T array are about 1.5 m apart (distance D), enough to cover the apparent solar extent (NAKAJIMA et al., 1995). For each pair of nearby antennas, then, the mutual distance between them is increasing according to the sequence $2^n D$[1], which results in an efficient application of the FFT (NAKAJIMA

[1] n is a natural number.

et al., 1994).

Figure 4.2 - Schematic (seen from above) of the antenna array formed by the NoRH (NAKAJIMA et al., 1994; KOSHIISHI et al., 1994).

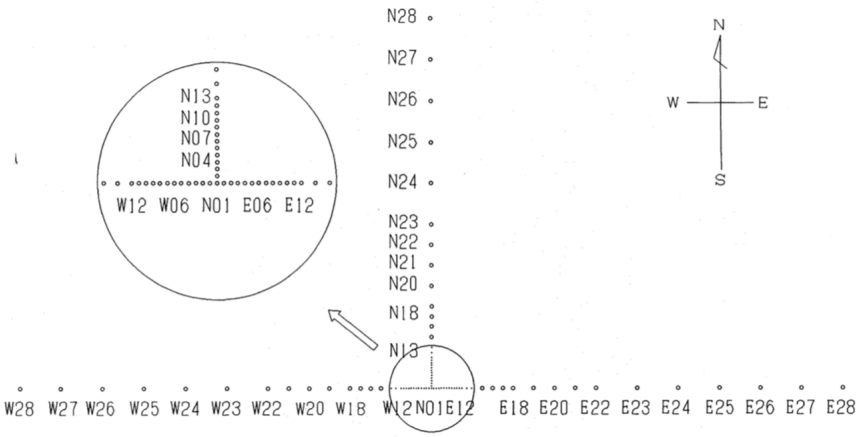

Source: Nakajima et al. (1994); Koshiishi et al. (1994).

5 PROCEDURES OF THIS RESEARCH

As shown by Chapter 3, several works have been conducted to detect and characterize the gyroresonance sources, given their association with magnetic fields in the solar atmosphere. As far as it is concerned, this work identified such radio sources by observing the module of the brightness temperature gradient $\left|\vec{\nabla}T_b\right|$ obtained from the solar maps at 17 GHz from NoRH. First, it was hypothesized that the prominent brightness bumps at this frequency could be caused by magnetic fields associated with gyroresonance at the 3rd and 4th harmonics and bremsstrahlung. This hypothesis was justified by the magnetic control on the radio emission variation that came from the resonant layers. As shown in the Chapter 6, such a hypothesis was confirmed. This result relied on data predominantly processed using IDL®[1] codes, including some SolarSoftWare (SSW)[2] routines, and programs from Coyote[3] Library. The following sections present the procedures adopted in this research.

5.1 The selection of active regions

This work selected active regions among the first observations performed by the Solar Dynamics Observatory (SDO), from NASA, along the first half of the 24th solar cycle: 2011, 2012, and 2013. This selection first looked for active regions that preceded flare(s), considering that such environments have magnetic fields intense enough to generate gyroresonance emission. To compose the sample of active regions prone to be analyzed, it was necessary to consider the difference in resolution between both groups of data used in this work: HMI magnetograms (from SDO)[4], where each file carries a 4096^2 pixels' matrix (LIU et al., 2012), and the maps of the Sun at 17 GHz (from NoRH), each composed of a 512^2 pixels' matrix (NITTA et al., 2013; NRO, 2013; ICCON, 2015). The magnetograms contain photospheric magnetic field data, while the NoRH maps contain brightness temperature data at 17 GHz. To perform joint analyses of files from different groups, it was necessary to reduce the matrix size of each selected magnetogram to the exact dimensions

[1] At the time this thesis was written, L3Harris Technologies, Inc. held the rights to the IDL® trademark. See https://www.nv5geospatialsoftware.com/portals/0/pdfs/IDL-Legal-Copyrights.pdf.

[2] Developed by Freeland and Handy (1998), SSW is a set of IDL® routines for processing the Sun study data (FREELAND; HANDY, 1998). During this research, the SSW installation was available on the site https://www.lmsal.com/solarsoft/ssw_install.html, from Lockheed Martin Solar and Astrophysics Laboratory (LMSAL).

[3] The Coyote Library programs used in this work were obtained from http://www.idlcoyote.com/ given by Fanning (2018).

[4] To download the SDO data, this work used Python resources from The SunPy Community et al. (2020).

of the NoRH images or expand the NoRH maps to fit the precise dimensions of the magnetograms. Therefore, selecting large active regions was important because it was expected that the number of pixels representing such regions in the NoRH images and the reduced magnetograms would provide a minimally adequate analysis. Because of this fact, this work selected active regions of area $\geq 10^{-4}$ of the solar disk. First, a 1400 G contour was used as a polarity boundary to find active regions with such a characteristic. Next, the area of the inner part of the contour was measured using IDL® command lines.

5.2 The searching for solar gyroresonance sources through 17 GHz brightness temperature gradient

Once the largest active regions were selected among the downloaded SDO-HMI magnetograms, the next step was to obtain the solar images at 17 GHz synthesized by NoRH[5]. This work then obtained the radio maps corresponding to the time of the selected magnetograms. As the original source, in this work, of information on brightness temperature and its gradient, and circular polarization degree, the NoRH data were then used to produce the BT and BTG maps, their circular polarization contours, the statistical analysis, and the scatter plots. As the original source of magnetic field information in this research, the SDO data were used to produce the photospheric magnetic field contours, the magnetogram extrapolation, the cosine contours, and the magnetic field height tables.

5.3 Centering and resizing of maps

The analysis of this data required the compilation of each NoRH map with a magnetogram of the same active region corresponding to the same time or very close times. This compilation aimed to have, on the same map, the simultaneous radio and magnetic data of a given region at a given time.

Since, for each dimension, the number of pixels in the NoRH and SDO maps is 512 (NITTA et al., 2013; NRO, 2013; ICCON, 2015) and 4096 (LIU et al., 2012), respectively, it was necessary to reduce the magnetograms to the size of the radio images or to expand the smaller maps to the dimensions of the larger ones. Initially, we intend to adopt the first resizing option, justifying the selection criteria explained earlier. However, the first strategy significantly degrades the magnetic field data. We, therefore, decided to adopt the second strategy solely to visualize: the contours of the

[5]For this work, the following link was used to download the NoRH data: https://solar.nro.nao.ac.jp/norh/images/10min/.

magnetograms adequately located on the BTG maps; and the level lines originating from the magnetogram extrapolation on such maps. Then we have also kept the original versions of the NoRH maps for data analysis.

For the resizing, first, we created a matrix with the same dimensions as the magnetograms and coordinates (ix_norh, jy_norh) given by:

$$ix\_norh = factor\_norh \cdot (ii\_sdo - x0\_sdo) + sz\_norh/2.0, \tag{5.1}$$

$$jy\_norh = factor\_norh \cdot (jj\_sdo - y0\_sdo) + sz\_norh/2.0, \tag{5.2}$$

$$factor\_norh = raio\_norh/raio\_sdo, \tag{5.3}$$

where ii_sdo and jj_sdo are, respectively, the horizontal and vertical coordinates for the pixels on the magnetogram; $x0\_sdo$ and $y0\_sdo$ are, respectively, the horizontal and vertical position of the solar center on the SDO map; sz_norh is the pixel size of the dimensions of the NoRH image. We then interpolated the original data matrix of the NoRH map to fit the matrix of coordinates (ix_norh, jy_norh).

5.4 Definition of the magnetogram levels associated with the gyroresonance emission at 17 GHz

The following step was to compile NoRH and SDO maps corresponding to the same active region and the same time or very close times. Such compilation included plotting, on the BTG maps, magnetogram magnetic field contours related to the 17 GHz gyroresonance. This contour plot aimed to demonstrate whether the magnetic field associated with the gyroresonance emission would occupy the same area occupied by brightness bumps on the solar disk. To define, then, the levels of these contours, we considered that the brightness coming to us from the gyroresonance emission comes predominantly from the 3rd and 4th harmonics of the gyrofrequency (VOURLIDAS et al., 2006). We then used Equation 3.16 to evaluate the magnetic field strength corresponding to such harmonic levels at 17 GHz. Considering Doppler broadening effects, we also stipulated a margin of $\pm 10\%$ from the result of this Equation. We, therefore, defined as contour levels (in Gauss) the following values: 1365.525, 1517.25, 1668.975, 1820.7, 2023, and 2225.3. In this thesis, we call the photospheric magnetic field with such values the characteristic magnetic field(s).

5.5 Linear force-free extrapolation

Although initially magnetic mapping magnetograms were important in locating photospheric fields strong enough for gyroresonance in higher layers and to associate the 17 GHz bumps with such radio mechanism, this work needed to have greater clarity about magnetic conditions at the height of the gyroresonant sources. Therefore, this work chose an SDO-HMI magnetogram for each region/day and performed a linear force-free extrapolation. For this procedure, a routine in IDL® was used, having as input parameter the coefficient α (which was null for most cases in this work), the dimensions in a number of voxels for a cube of magnetic field strengths, and the SDO-HMI magnetogram itself with the bounded area around the active region. For this cube, we assumed a Cartesian coordinate system defined by (x, y, z), where x and y refer to the horizontal Cartesian axes, parallel to the surface of the region mapped by the magnetogram, and z refers to the vertical axis, perpendicular to this region surface. As output, this program generated a cube containing, for each voxel/coordinate, the intensities of the extrapolated magnetic field components: B_x, B_y and B_z, which refer respectively to the cube's x, y and z axes. The magnetic extrapolation's total intensity (B) was then calculated for each cube voxel. The result of such a calculation comes from this Equation:

$$B = \sqrt{B_x^2 + B_y^2 + B_z^2}. \tag{5.4}$$

Therefore its result produced the B cube, with the same dimensions as the previous cube, over the same coordinates of the extrapolated magnetogram.

The specific goals of this extrapolation were: to locate the specific lines orthogonal to the family of equipotential magnetic field surfaces; and to identify the slopes of the magnetic field lines relative to the line of sight at the height of the gyroresonance sources.

In this first objective, such specific lines are indicated by magnetic field levels associated with the extended 3rd and 4th harmonics. The broadening of harmonics took into account the effect of Doppler broadening, and therefore, the following broadening rates were tested: 5%, 10%, 15%, 20%, and 30%. From the B cube, all the fields that do not correspond to the extended harmonics at 17 GHz have been annulled. All the values of B located at coordinates (x, y, 0), which correspond to the first height range (up to 350 km), have also been annulled. Finally, for each coordinate (x, y) with non-zero B, the levels of these fields were obtained by measuring the average of total magnetic fields along the vertical dimension of the B cube. This

average only considered voxels with non-null B. A 2-dimensional plot of these levels was then made on an expanded BTG map[6] corresponding to the same magnetogram coordinates and the same or a nearby magnetogram time. These plots are shown alongside their respective extrapolation source magnetograms (see Chapter 6).

Subsequently, for the second objective of this extrapolation, assuming that θ is the angle indicating the inclination of the extrapolated magnetic field to the line of observation, the following calculation was made:

$$cos\theta = B_z/B. \tag{5.5}$$

This Equation was applied to each coordinate of the original B cube[7] where $B \neq 0$. For each coordinate (x, y) with non-zero B, the results of Equation 5.5 were then averaged vertically, considering only the voxels with non-null B. The result of this average was then plotted as contours on expanded BTG maps corresponding to the same extrapolated magnetogram coordinates and time or a time close to it. The values of these plotted contours are among the following numbers: 0.8, 0.82, 0.84, 0.86, 0.88, 0.9, 0.92, 0.94, 0.96, 0.98, and 1.0.

Another important piece of information sought and shown by this work was the estimate of the height ranges of the magnetic fields calculated by this extrapolation. Considering that each vertical pixel of the cube corresponds to a band 350 km high, we verified the localization pixels of B associated with the extended 3rd and 4th harmonics at 17 GHz. In this way, we generated the height tables shown in Chapter 6.

5.6 The brightness variables

For the statistical analysis and the observation of the brightness and its bumps over the 17 GHz maps of the active regions, we obtained two brightness variables from each file downloaded from NoRH: the brightness temperature (T_b) and the brightness temperature gradient $\left(\left|\vec{\nabla}T_b\right|\right)$. Such a procedure was aimed at identifying and characterizing the brightness elevations.

5.7 The BTG maps

The best way to highlight the bumps emerging from the radio emission is to map the brightness temperature gradient of a given NoRH image, since the maps resulting

[6]Expanded BTG maps are explained at the end of Section 5.7.
[7]The original B cube is the one before certain values of B were annulled.

from such a method show only the areas where the brightness is variant (see Figure 5.1) where each color represents a range of gradient values. Then, using an IDL® routine to calculate the brightness temperature gradient in the radio data, this work constructed the BTG maps of each selected active region. The coordinates of these regions were carefully checked to ensure that the area observed on the NoRH map is the same as that shown in the magnetogram.

Figure 5.1 - Originating from the same ifa file (from NoRH), every figure presents the NoRH solar observation at 17 GHz, at 2011/08/02, 00:00:01 UT. Figure (a) is the original picture with the false color of IDL®. As a result of the IDL® process in which the brightness temperature gradient is calculated from Figure (a), Figure (b) is the BTG map of the 1st image. The small square (in both these first images) highlights the active region NOAA 11263, best shown in its BTG map (Figure (c)).

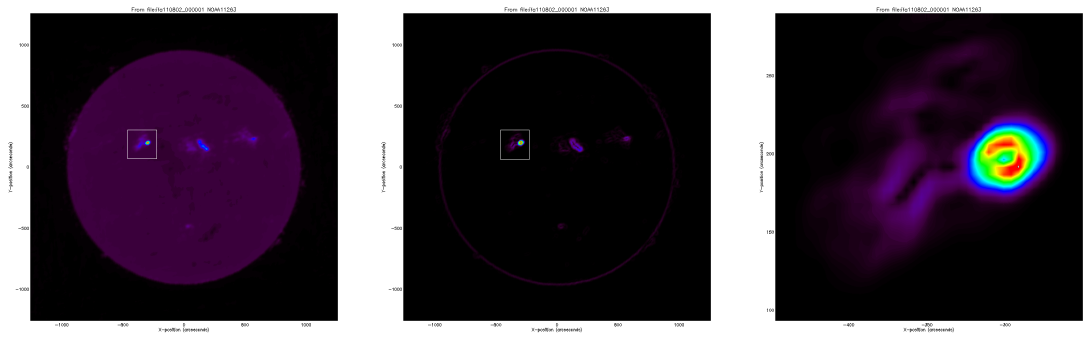

(a) (b) (c)

Source: Figure (a): Adapted from NoRH (2011).

To generate BTG maps for each polarization sense, ifa and ifs files[8] from NoRH were used in a time slot for each region. These files, in FITS format, contain the original NoRH maps (NRO, 2013; ICCON, 2015). The first file contains the brightness temperature defined by $T_b^{(R)} + T_b^{(L)}$, while in the ifs file, the brightness temperature is given by $T_b^{(R)} - T_b^{(L)}$ (NRO, 2013; ICCON, 2015). The matrices of both files of the same region/time were summed with each other, and the result of this sum was divided by 2, giving a matrix with the values of $T_b^{(R)}$. To generate the data matrix $T_b^{(L)}$, the ifs matrix was subtracted from the ifa matrix, and the result of

[8]Respectively, the ifa and ifs files are originally named ifaAABBCC_EEFFGG and ifsAABBCC_EEFFGG, where AA, BB, and CC are double digits that represent, in that order, the last two digits of the year, the month, and the day (NRO, 2013; ICCON, 2015). In turn, EE, FF, and GG are double digits that represent, respectively, the hour, the minute, and the second (NRO, 2013; ICCON, 2015).

this subtraction was divided by 2. After generating the $T_b^{(L)}$ and $T_b^{(R)}$ matrices, we generated their BTG maps by applying the IDL® routine mentioned above (in this section) to these matrices. Corresponding to the $T_b^{(L)}$ matrices, then, the produced BTG maps are called LHCP-BTG maps. Corresponding to the $T_b^{(R)}$ matrices, the produced BTG maps are called RHCP-BTG maps. The so-called LHCP-BT and RHCP-BT maps are, respectively, maps of $T_b^{(L)}$ and $T_b^{(R)}$. The aforementioned expanded BTG maps are the result of applying the IDL® routine for calculating the brightness temperature gradient to expanded NoRH maps at 17 GHz.

5.8 Analysis of polarization degree (r_c)

Finally, just like Vourlidas et al. (2006), this work considered as potential gyroresonance sources those areas where the circular polarization modulus $|r_c|$ was greater than 30% on the 17 GHz map. Based on this finding from that paper, we then plotted, over the 17 GHz maps of each active region, the contours of the degree of polarization according to such a criterion. This method aimed to verify that such outlines would involve the areas of brightness bumps.

The procedure to generate the polarization contours was also based on the NoRH ifa and ifs files for each region in a time slot. To create a polarization map for each region/time, Equation 3.11 was applied using the results of the matrix operations described in Section 5.7. Therefore, in the polarization maps, positive values indicate the right-hand sense (RHCP), while negative values indicate the left-hand sense (LHCP) (NRO, 2013; ICCON, 2015).

In addition to this procedure, we analyzed the correlation between each brightness variable and $|r_c|$ for two conditions: $|r_c| \geq 30\%$ or $|r_c| < 30\%$. We calculated this correlation for each sense of circular polarization. Considering that the increase in the participation of gyroresonant electrons tends to raise the modulus of the polarization degree, in this statistical analysis, we sought to verify whether the rise in the brightness variables would accompany an increasing contribution of the gyroresonance in the emission at 17 GHz.

6 RESULTS AND DISCUSSIONS

Using the method explained in Chapter 5, eight active regions were selected and analyzed by looking at their magnetograms and radio maps. Table 6.1 lists such regions (identified according to NOAA, as shown by the Solar Monitor[1]). This site is also the source of information presented below about the flares mentioned in this Chapter.

Table 6.1 - Table of the selected active regions.

Active region	**time of analyzed data**
NOAA 11263	August 2 and 3, 2011
NOAA 11302	September 26, 2011
NOAA 11384	December 26, 2011
NOAA 11476	May 10, 2012
NOAA 11504	June 14, 2012
NOAA 11520	July 14, 2012
NOAA 11877	October 24, 2013
NOAA 11899	November 16, 2013

As expected, the mapped magnetic fields shared their coordinates with the prominent brightness bumps in several BT and BTG maps (see Figures 6.1 and 6.2). Since they were of a photospheric height, such fields were not sources of the gyroresonance. Still, they indicated the approximate location of the magnetic fields responsible for this mechanism at 17 GHz, in latitude and longitude, for the 3rd and 4th harmonic. Due to said fact, this work performed linear force-free extrapolation of the SDO-HMI magnetogram of a specific time of each active region and, thus, estimated the magnetic field associated with the 17 GHz emission coming from the extended 3rd and 4th harmonic, considering the Doppler broadening. The results then indicate a substantial contribution from the gyroresonance, especially in the extended 4th harmonic.

Another result that corroborates the hypothesis of this work is the high degree of circular polarization of the prominent brightness bumps, especially through the BTG maps. On such maps, the polarization levels greater than or equal to 30% coincide with the strong bumps, which indicates the presence of gyroresonance.

[1] https://solarmonitor.org

Figure 6.1 - The white contours, from SDO-HMI magnetograms, indicate the characteristic magnetic fields, from the photosphere. In all cases, these contours partially or completely coincide with the bumps. As with all BTG maps, these display a header with information on the day and time of the observation and the NOAA identification of the respective active region. Figure 6.2 is a continuation of this one.

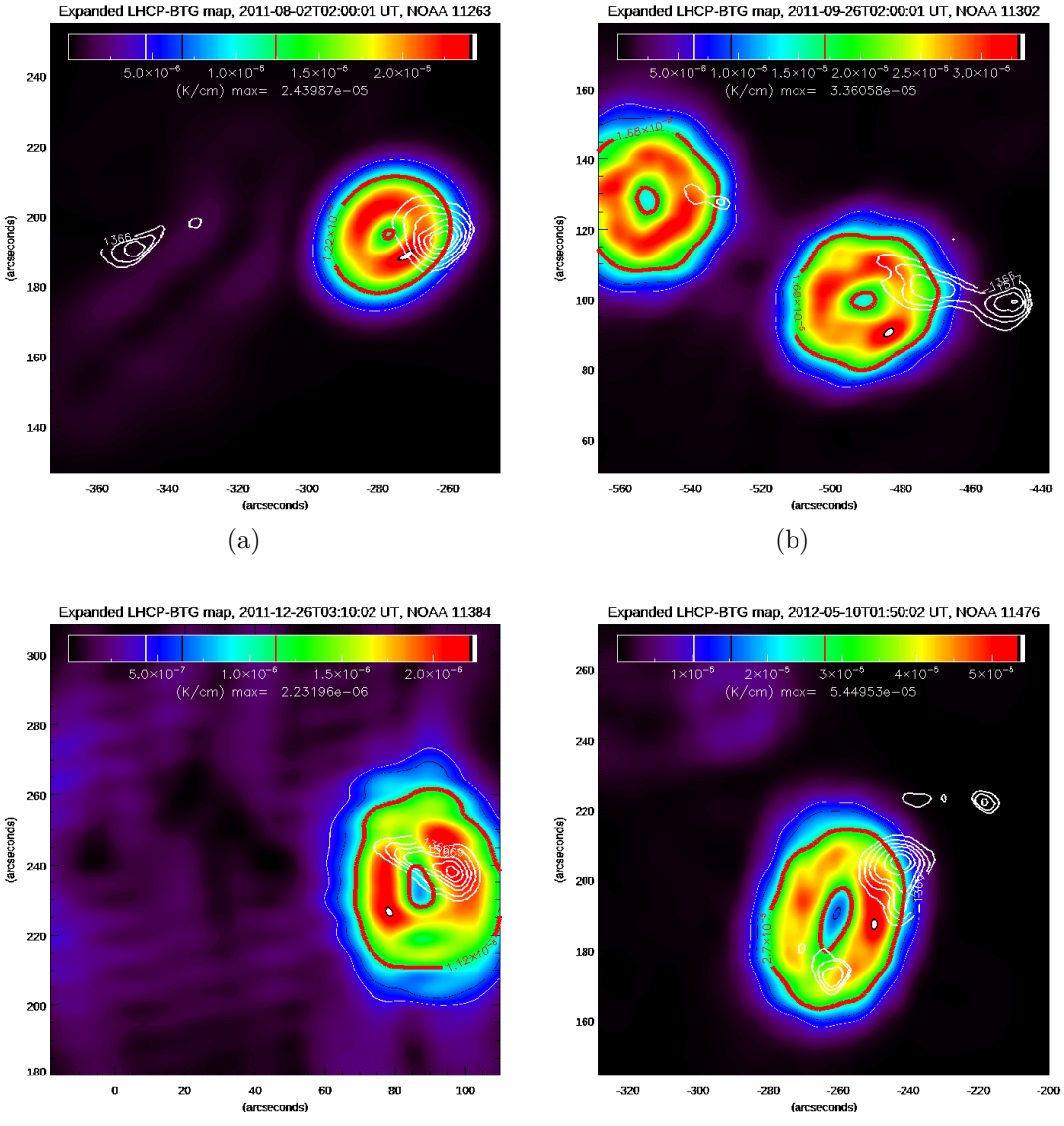

(a) (b)

(c) (d)

Some false positives have also been identified among the results, demonstrating that not all intense brightness intensification is associated with gyroresonance.

It is also essential to report that, according to Solar Monitor[2], some selected active

[2]https://www.solarmonitor.org/

Figure 6.2 - Second sample of BTG maps with white contours originating from SDO-HMI magnetograms indicating characteristic magnetic fields. See the Figure 6.1.

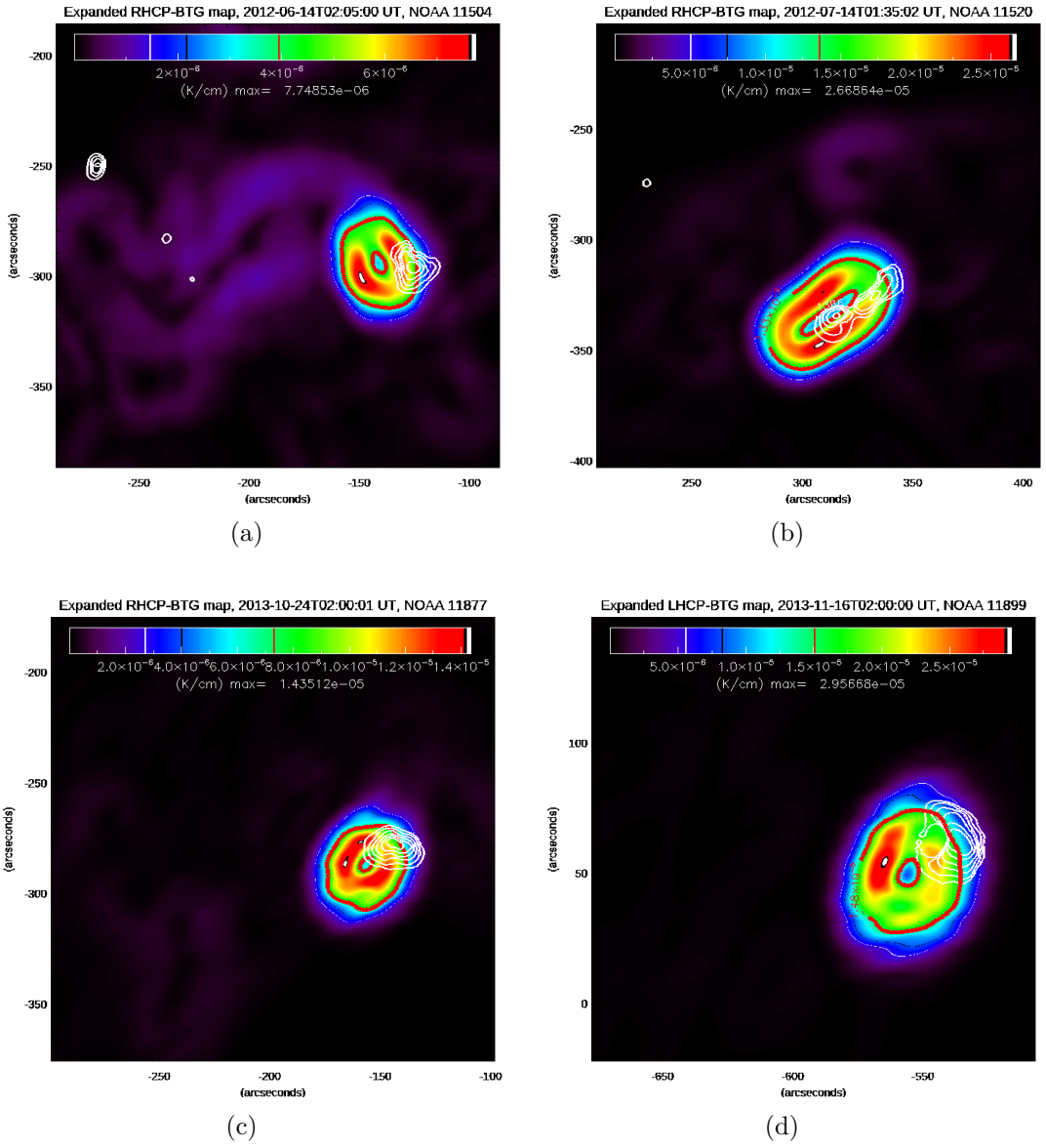

regions produced flare(s) at specific times. This fact opens up the possibility of the gyrosynchrotron mechanism's influence on the bumps occurring at such times. At times without flares, however, the gyroresonance has a higher and stronger probability of being the leading cause of the brightness bumps produced in these regions, given its high degree of polarization and magnetic field profile.

Culminating in such findings, the data analysis has verified, for most of the observed region, a high correlation of $|r_c| \geq 30\%$ (characteristic of gyroresonant emissions)

with the brightness temperature and its gradient. In this same analysis, low polarization ($|r_c| < 30\%$) shows weak or moderate correlations in all observed cases. The following Section details the results from the analysis made for each active region.

6.1 Analysis and characterization of the selected regions

6.1.1 Active region NOAA 11263

6.1.1.1 August 2, 2011

According to the radio maps, on this date, this region was characterized by high left-hand circular polarization ($|r_c| \geq 30\%$) where the brightness was most intensified, as shown in Figure 6.3(a). Such a fact was observed on each of the 39 LHCP-BTG maps of this region referring to this day, where the circular polarization reached (or exceeded) 80%, reaching 90% on some of these maps. On the 02:00:00 UT bump, extrapolation of the SDO-HMI magnetogram referring to 01:59:11 UT indicates, in Figure 6.3(b), a high concentration of magnetic field lines of low inclination with the line of sight, explaining the high polarization revealed in Figure 6.3(a). For such polarization, the brightness intensification ranged from $(2.7 \pm 0.7) \times 10^{-5}$ to $(16.6 \pm 1.4) \times 10^{-5}$ K cm^{-1} where $|r_c| \geq 30\%$, and from $(4.0 \pm 1.2) \times 10^{-8}$ to $(6.3 \pm 1.1) \times 10^{-5}$ K cm^{-1} where $|r_c| < 30\%$, while the range of the brightness temperature was from $(1.0 \pm 0.1) \times 10^4$ to $(22.8 \pm 1.6) \times 10^4$ K for $|r_c| \geq 30\%$, and from $(0.5 \pm 0.0) \times 10^4$ to $(2.9 \pm 0.4) \times 10^4$ K for $|r_c| < 30\%$. These results then show that, for $|r_c| \geq 30\%$, both the averages of the highest peaks, among the maps, of $T_b^{(L)}$ and $\left|\vec{\nabla} T_b^{(L)}\right|$ are, respectively, 680.147% and 164.533% larger than the averages of the maximum values of these same brightness variables, in that order, obtained from the area where $|r_c| < 30\%$ in the maps. On the other hand, the low-polarization brightness variables considerably outperformed the averages of the minimum values of high-polarization brightness variables. For $|r_c| < 30\%$, the averages of the maximum results of ${T_b}^{(L)}$ and $\left|\vec{\nabla} T_b^{(L)}\right|$ from all the maps are, respectively, 185.210% and 131.749% larger than the averages of the minimum values of ${T_b}^{(L)}$ and $\left|\vec{\nabla} T_b^{(L)}\right|$, in that order, of $|r_c| \geq 30\%$.

In addition, for this region, the correlations obtained between each LHCP brightness variable and the modulus of circular polarization degree ($|r_c|$) are based on the dispersion of 65 to 85 points corresponding to $|r_c| \geq 30\%$ and dispersion of 1596 to 1616 points related to $|r_c| < 30\%$. The Figures 6.4(a) and 6.4(b) show a trend of growth of these brightness variables with increasing $|r_c|$. The correlation further reveals that the growth control of ${T_b}^{(L)}$ and $\left|\vec{\nabla} T_b^{(L)}\right|$ was best exerted in the condition

where $|r_c| \geq 30\%$. As presented by the Figures 6.5(a) and 6.5(b), the brightness temperature and its gradient were strongly correlated with $|r_c| \geq 30\%$ and weakly (or moderately) correlated with $|r_c| < 30\%$. For $|r_c| \geq 30\%$, the correlation index ranged from 0.70 to 0.90 for ${T_b}^{(L)}$, and from 0.69 to 0.90 for $\left|\vec{\nabla} T_b^{(L)}\right|$, while, for $|r_c| < 30\%$, the correlation ranged from 0.06 to 0.47 for ${T_b}^{(L)}$, and from 0.18 to 0.52 for $\left|\vec{\nabla} T_b^{(L)}\right|$. The correlation analysis indicated a high significance for $|r_c| \geq 30\%$. For $|r_c| < 30\%$, the significance of the correlations is also strong, except for 2 out of 39 LHCP-BT maps, whose results, in this case, were 0.02 and 0.05.

Figure 6.3 - LHCP-BTG maps of region NOAA 11263 (at August 02, 2011, 02:00:01 UT) on which are white contours of: (a) the high circular polarization and (b) the cosine of the angle between the extrapolated magnetic field and the line of sight. This extrapolation considered $\alpha = 0.20$ and was performed on a cube size of 256^3 voxels over this area. The red thick-line contour indicates half of the maximum value of $\left|\vec{\nabla} T_b^{(L)}\right|$ in the respective map.

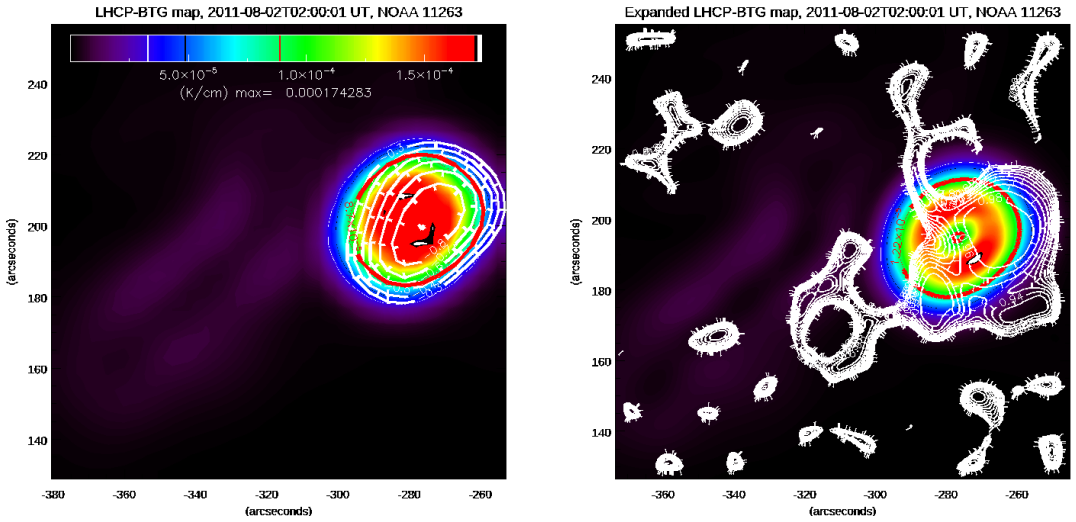

(a) (b)

Another important finding is that a considerable part of the 02:00:01 UT bump corresponds to the extrapolated magnetic fields associated with the 3rd and 4th harmonics plus their broadening rates (see Figure 6.6(b)). The extrapolated magnetogram is shown by Figure 6.6(a).

Figure 6.4 - Scatter plots related to: (a): $T_b^{(L)}$ vs. r_c, and (b): $\left|\vec{\nabla} T_b^{(L)}\right|$ vs. r_c for the active region NOAA 11263, at August 2, 2011, 02:00:01 UT.

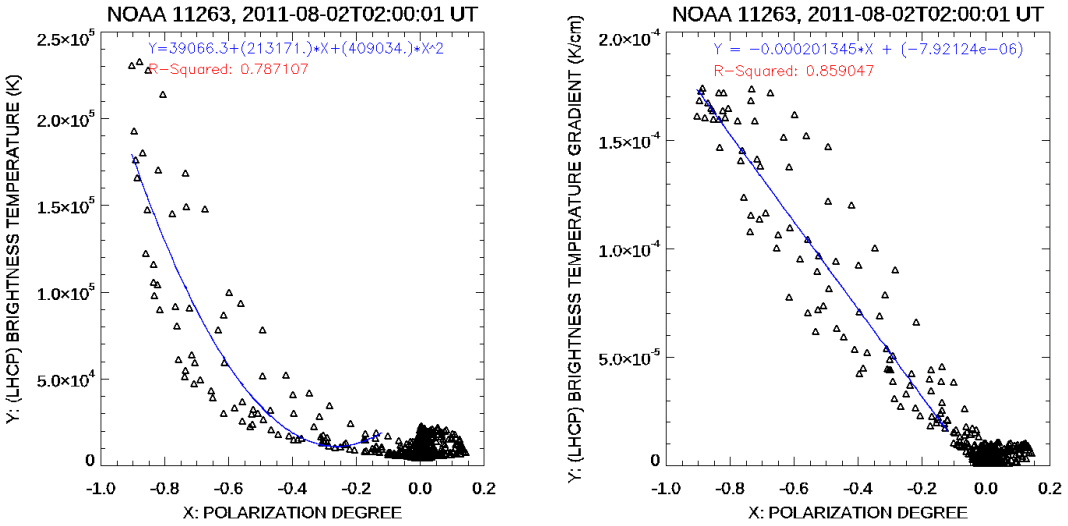

(a) (b)

Figure 6.5 - Degree of Spearman correlation of $|r_c|$ with (a): $T_b^{(L)}$ and (b): $\left|\vec{\nabla} T_b^{(L)}\right|$ for each NoRH map of the region NOAA 11263, at August 2, 2011. The blue triangles represent the correlation with $|r_c| \geq 30\%$, while the red squares indicate the correlation with $|r_c| < 30\%$. Almost all these data showed high significance, except for the 25th and 26th LHCP-BT maps in the correlation with $|r_c| < 30\%$.

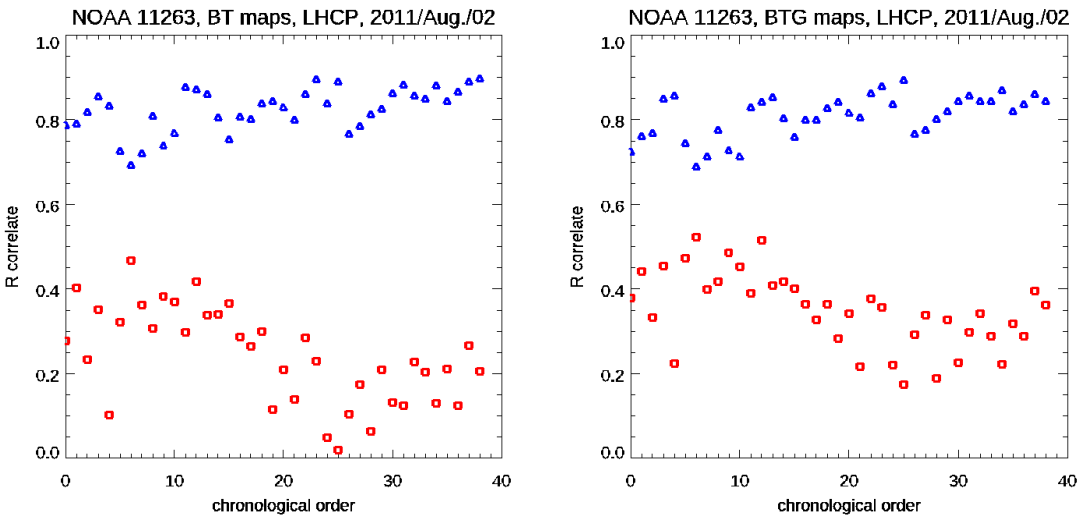

(a) (b)

Figure 6.6 - Region NOAA 11263 at August 2, 2011: (a) SDO-HMI magnetogram (at 01:59:11 UT) and (b) its extrapolated magnetic field level lines over expanded LHCP-BTG map (at 02:00:01 UT). (b): The dotted lines indicate magnetic field strengths corresponding to extended 3rd harmonic, while the thick lines (except the red one) indicate fields associated with extended 4th harmonic. (b): Represented by the colors in the lines, the broadening of the harmonics are +5% (white), +10% (orange), +15% (green), +20% (light blue), and +30% (dark blue).

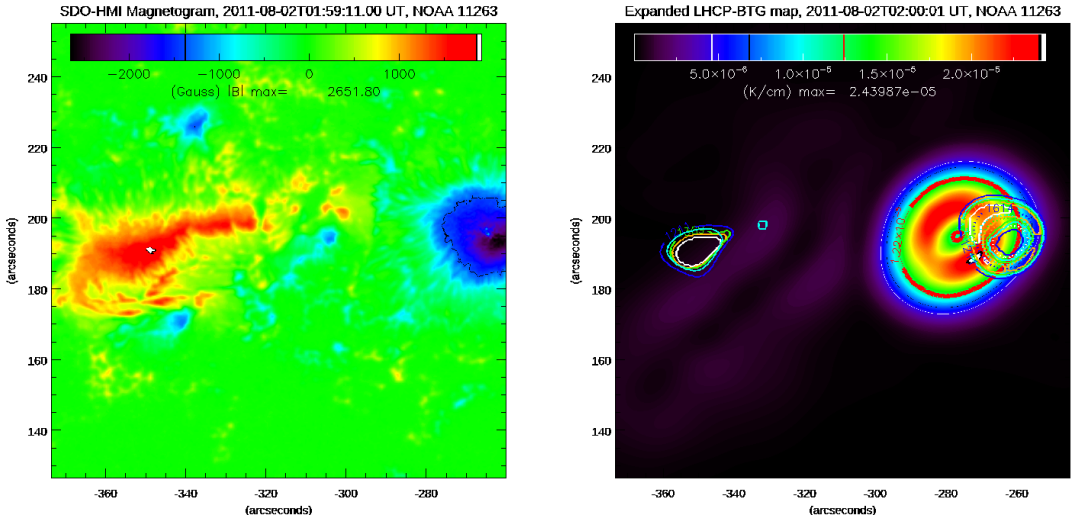

(a) (b)

Source: Figure (a): Adapted from NASA (2011).

In turn, the Solar Monitor[3] indicates the occurrence of a C1.2 class flare from 03:10 to 03:14 UT. The data from this time, which correspond to one map for each brightness variable, probably have a contribution from the gyrosynchrotron mechanism. The remaining maps in this region, therefore, have contributions from the gyroresonance.

6.1.1.2 August 3, 2011

Corresponding to the following day, the NoRH data shows region NOAA 11263 still exhibiting its brightness bump with a high degree of circular polarization (see Figure 6.7(a)). Similarly to the previous day, such a finding was verified in all 39 BTG maps, in which the brightness bump of this region presented maximum circular polarization, between 80% and 90%. As the previous observation, the extrapolation of the region's magnetogram corresponding to 01:59:10 UT (Figure 6.10(a)) indicates lines with a low inclination with the line of sight over the 02:00:02 UT bump, as

[3]https://www.solarmonitor.org/index.php?date=20110802

shown in Figure 6.7(b). Also, the brightness maps for this day show that the more prominent peaks of $T_b^{(L)}$ and $\left|\vec{\nabla} T_b^{(L)}\right|$ of high polarization outweighed the peaks of the low polarization brightness variables (see the Figures 6.8(a) and 6.8(b)).

Figure 6.7 - LHCP-BTG maps of region NOAA 11263 (at August 03, 2011, 02:00:02 UT) on which are white contours of: (a) the high circular polarization and (b) the cosine of the angle between the extrapolated magnetic field and the line of sight. This extrapolation considered $\alpha = 0.20$ and a cube size of 256^3 voxels over this area. The red thick-line contour indicates half of the maximum value of $\left|\vec{\nabla} T_b^{(L)}\right|$ in each map.

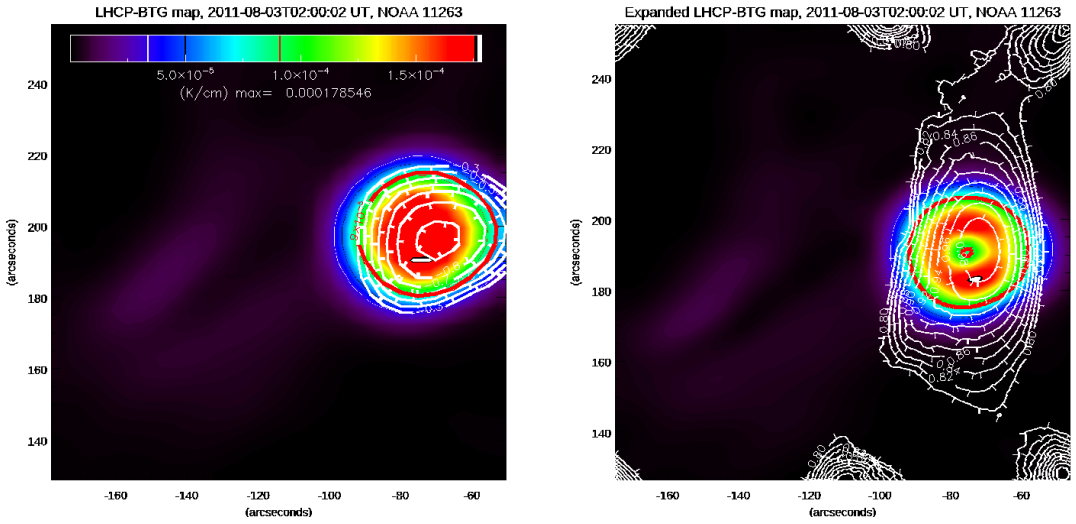

(a) (b)

The range of values assumed by the $\left|\vec{\nabla} T_b^{(L)}\right|$ corresponding to $|r_c| \geq 30\%$, then, lies between $(1.8 \pm 1.3) \times 10^{-5}$ to $(12.9 \pm 3.5) \times 10^{-5}$ K cm^{-1}, whereas for the range corresponding to $T_b^{(L)}$ of similarly intense polarization, the assumed values range from $(1.1 \pm 0.2) \times 10^4$ to $(17.9 \pm 4.2) \times 10^4$ K. On the other hand, corresponding to the low-polarization emission ($|r_c| < 30\%$), $\left|\vec{\nabla} T_b^{(L)}\right|$ and $T_b^{(L)}$, respectively, assumed the following ranges of measurements: from $(4.2 \pm 0.9) \times 10^{-8}$ to $(5.5 \pm 1.2) \times 10^{-5}$ K cm^{-1}, and from $(4.6 \pm 0.3) \times 10^3$ to $(3.3 \pm 0.8) \times 10^4$ K. The advantage of high-polarization brightness variables over low-polarization ones is also indicated by the averages of the maximum values of $\left|\vec{\nabla} T_b^{(L)}\right|$ and ${T_b}^{(L)}$ corresponding to $|r_c| \geq 30\%$ and $|r_c| < 30\%$. The averages of the highest peaks of $\left|\vec{\nabla} T_b^{(L)}\right|$ and ${T_b}^{(L)}$ obtained from the high-polarization emission among the maps are, respectively, 132.461% and 437.959% higher than the averages of the maximum values of $\left|\vec{\nabla} T_b^{(L)}\right|$

and $T_b{}^{(L)}$, in that order, obtained from the low-polarization emission. On the other hand, the averages of the maximum results of $\left|\vec{\nabla}T_b^{(L)}\right|$ and $T_b{}^{(L)}$ obtained from the low-polarization emission, among the maps, indicate advantages of 202.465% and 204.126%, respectively, over the averages of the minimum values of $\left|\vec{\nabla}T_b^{(L)}\right|$ and $T_b{}^{(L)}$, in that order, obtained from the high-polarization emission among the maps.

Figure 6.8 - Scatter plots related to: (a): $T_b^{(L)}$ vs. r_c, and (b): $\left|\vec{\nabla}T_b^{(L)}\right|$ vs. r_c for the active region NOAA 11263 at August 3, 2011, 02:00:02 UT.

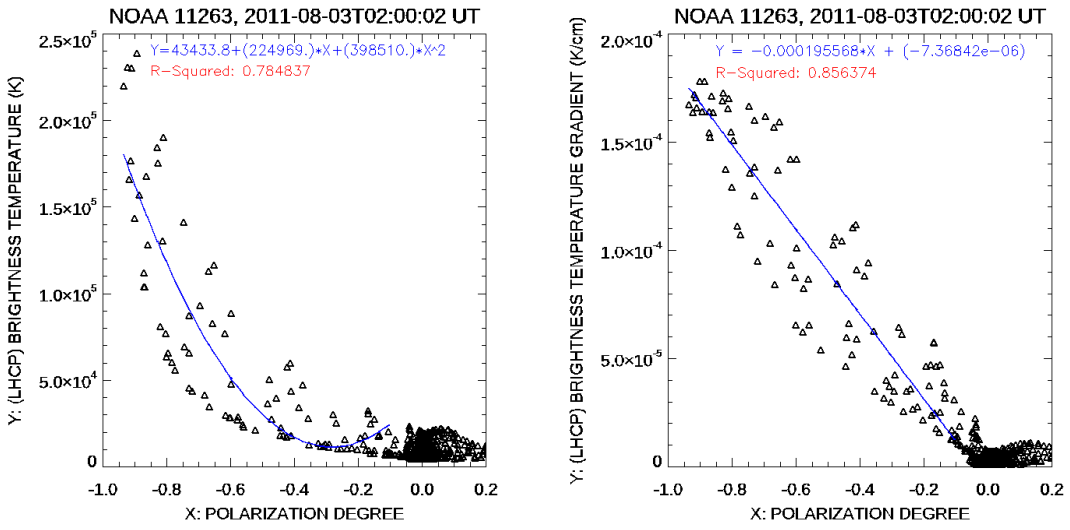

(a) (b)

The correlation analysis, in turn, was performed by processing a data cloud of 61 to 97 points corresponding to the high-polarization emission and 1584 to 1620 points coming from the low-polarization emission. As with the previous day, this day's data still shows the predominance of the strong correlation between the brightness variables and the polarization degree modulus above 30%. As Figure 6.9 reveals, the correlation of $|r_c| \geq 30\%$ with $T_b^{(L)}$ and $\left|\vec{\nabla}T_b^{(L)}\right|$ ranges from 0.76 to 0.94 and from 0.69 to 0.92, respectively, with a high significance. The correlation of $|r_c| < 30\%$ with $T_b^{(L)}$ and $\left|\vec{\nabla}T_b^{(L)}\right|$ varies from -0.10 to 0.39 and from 0.08 to 0.48, respectively, also with a high significance. The correlation is insignificant in only 6 out of 39 LHCP-BT maps and 3 out of 39 LHCP-BTG maps.

Concerning the analysis of the extrapolated magnetic field, this procedure also indicated, over nearly half of the 02:00:02 UT bump, the presence of magnetic field

corresponding to the extended 3rd and 4th harmonics (see the Figure 6.10(b)). The magnetic levels corresponding to the extended 4th harmonic indicate greater participation in the brightness bump than the extended 3rd-harmonic levels. The base magnetogram of this extrapolation is shown in Figure 6.10(a). Table 6.2 shows the estimated heights for each of the extrapolated magnetic fields associated with these extended levels.

Figure 6.9 - Degree of Spearman correlation of $|r_c|$ with (a): $T_b^{(L)}$ and (b): $\left|\vec{\nabla} T_b^{(L)}\right|$ for each NoRH map of the region NOAA 11263 at August 3, 2011. The blue triangles represent the correlation with $|r_c| \geq 30\%$, while the red squares indicate the correlation with $|r_c| < 30\%$. Almost all these data showed high significance, except for the correlation with $|r_c| < 30\%$ in the 19th, 26th, 30th, 31st, 33rd, and 37th LHCP-BT maps, and the 29th, 32nd, and 37th LHCP-BTG map.

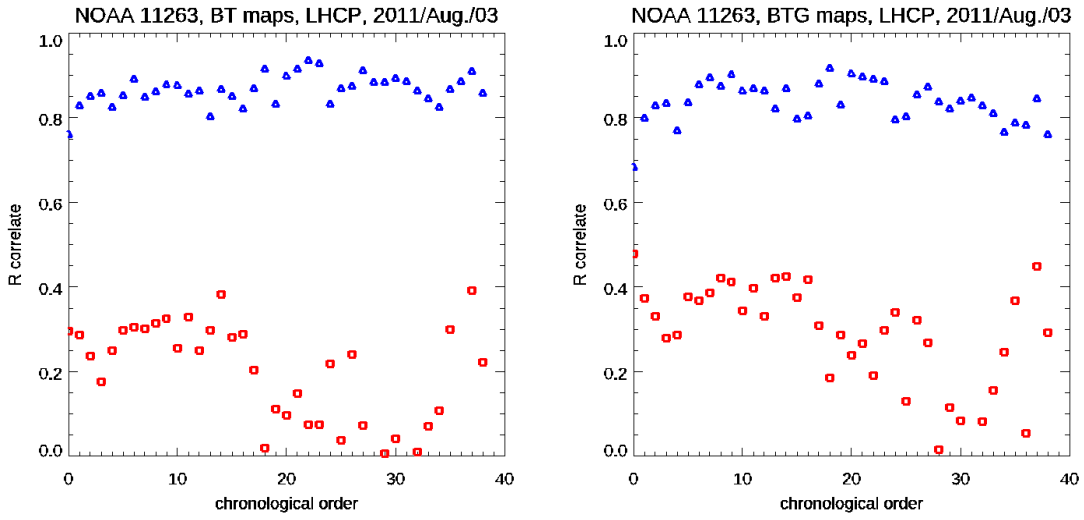

(a) (b)

Table 6.2 - For region NOAA 11263 at August 3, 2011: Height (in Km) of the extrapolated magnetic fields associated with the extended harmonics.

Harmonic	±5%	±10%	±15%	±20%	±30%
3rd	350-700	350-1050	350-1400	350-1750	350-2450
4th	350-2100	350-2450	350-2800	350-3150	350-4200

Figure 6.10 - Region NOAA 11263 at August 3, 2011: (a) SDO-HMI magnetogram (at 01:59:10 UT) and (b) its extrapolated magnetic field level lines over expanded LHCP-BTG map (at 02:00:02 UT). (b): The dotted lines indicate magnetic field strengths corresponding to extended 3rd harmonic, while the thick lines (except the red one) indicate fields associated with extended 4th harmonic. (b): Represented by the colors in the lines, the broadening of the harmonics are +5% (white), +10% (orange), +15% (green), +20% (light blue), and +30% (dark blue).

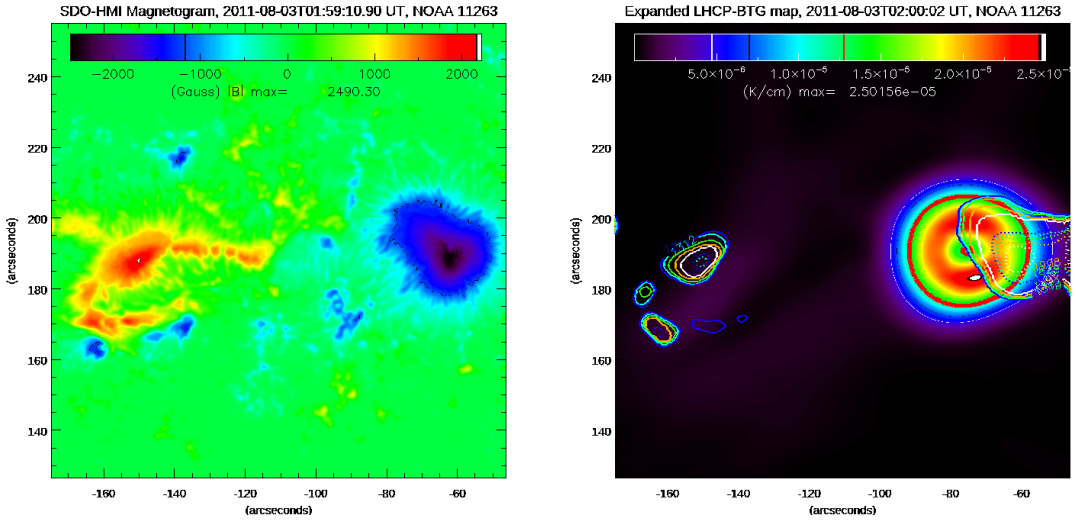

(a) (b)

Source: Figure (a): Adapted from NASA (2011).

Regarding the presence of flares, the Solar Monitor[4] indicates the occurrence of an M1.7 at 04:29 UT, seeming not to have considerably affected the correlation of $|r_c| \geq 30\%$ with $T_b^{(L)}$ and $\left|\vec{\nabla} T_b^{(L)}\right|$. The evolution of the LHCP BT and BTG maps in the time interval in which this flare occurred revealed the appearance of a low-polarization brightness bump that was less intense than the one shown in Figure 6.11. This new bump was preceded by 9 minutes of the occurrence of the flare and did not affect the maintenance of the high-polarization brightness bump.

[4]https://www.solarmonitor.org/index.php?date=20110803

Figure 6.11 - The evolution of 17 GHz $\left|\vec{\nabla}T_b^{(L)}\right|$ of active region NOAA 11263, at August 3, 2011, from 03:40:02 to 04:30:02 UT. Notice a less intense brightness bump emerging next to the coordinates (-150, 150) arcsec and the white contours of the characteristic magnetic field, as shown by the correspondent magnetogram.

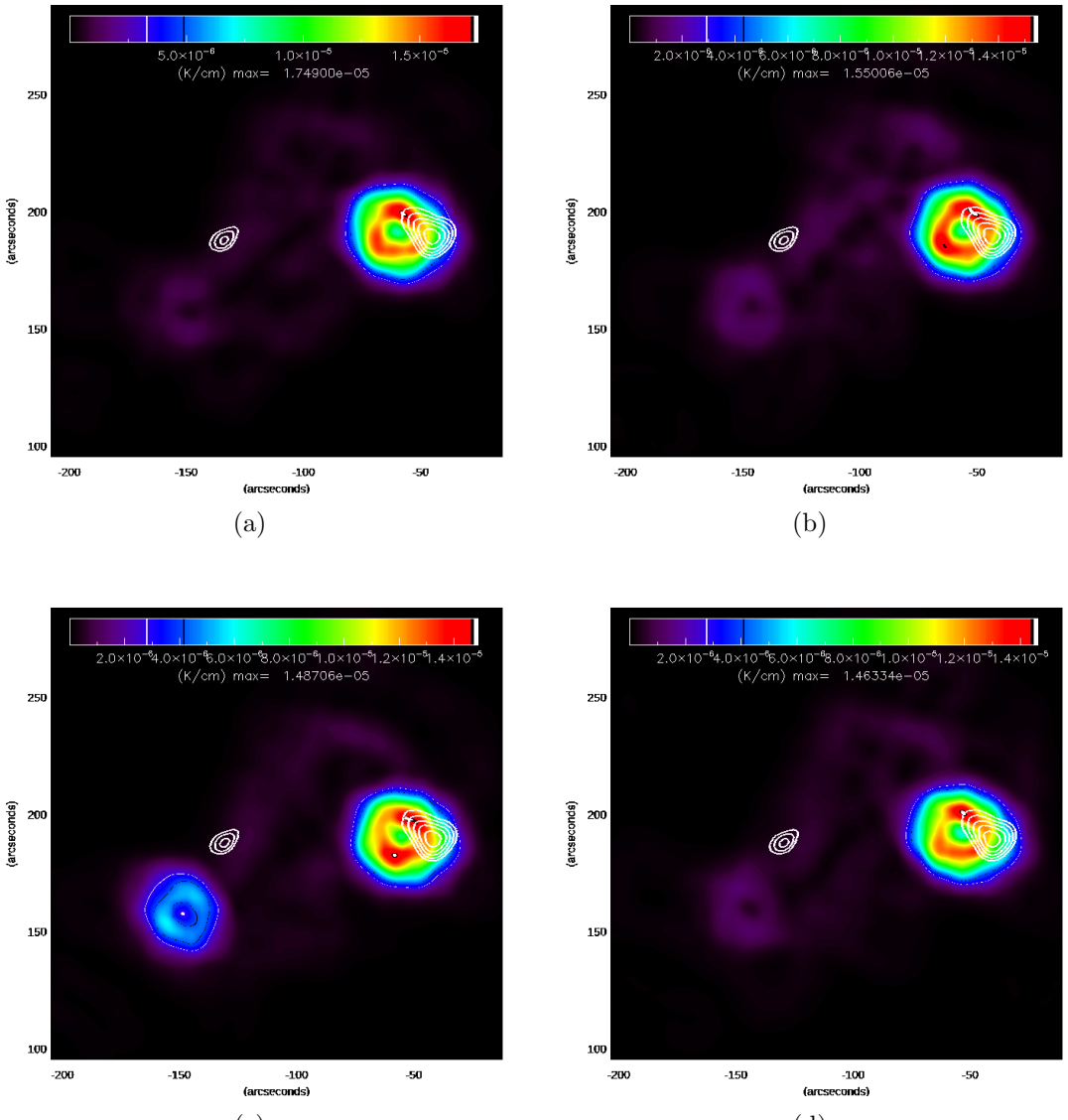

(a) (b)

(c) (d)

6.1.2 Active region NOAA 11302 (September 26, 2011)

Similarly to the previous region, this one also showed high left-hand circular polarization, where $|r_c| \geq 30\%$, over an area of prominent brightness growth (see Figure 6.12(a)). Among the 37 BTG maps of this region, corresponding to this day's ob-

servations, the levels of this polarization over the highly polarized brightness bump preferentially reached (or exceeded) 80%. On the other hand, this region showed a low circular polarization brightness bump (to the northeast of the highly polarized area). However, corroborating with the fundamentals of gyroresonance, the extrapolated magnetic field lines corresponding to 01:59:05 UT followed with little inclination to the line of sight over the highly polarized brightness bump referring to 02:00:01 UT, different from its disposition on the low polarization brightness bump (see Figure 6.12(b)) at the same time.

Figure 6.12 - LHCP-BTG maps of region NOAA 11302 (at September 26, 2011, 02:00:01 UT) on which are white contours of: (a) the high circular polarization and (b) the cosine of the angle between the extrapolated magnetic field and the line of sight. This extrapolation considered $\alpha = 0.0$ and a cube size of 256^3 voxels over this area. The red thick-line contour indicates half of the maximum value of $\left|\vec{\nabla} T_b^{(L)}\right|$ in each map.

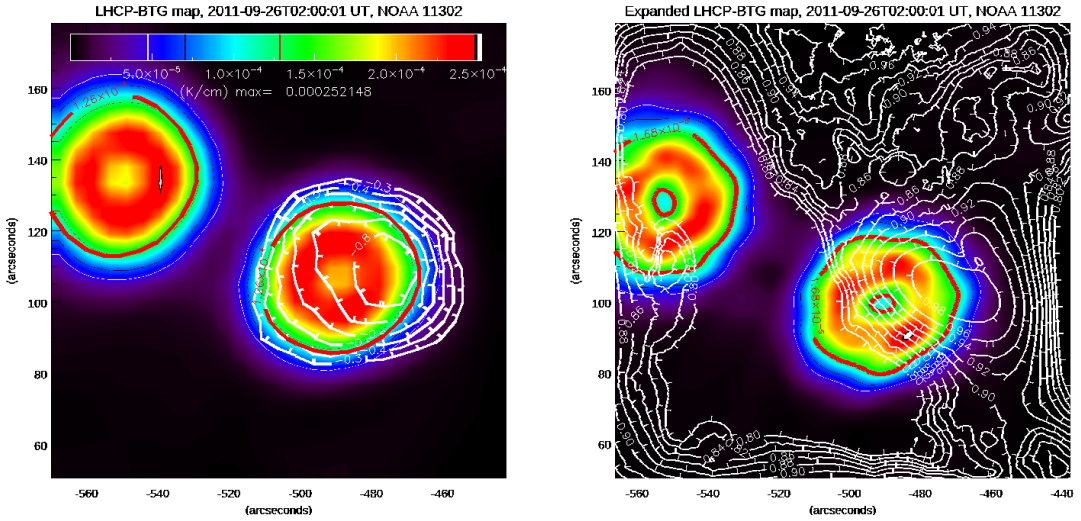

(a) (b)

From the area where $|r_c| < 30\%$, the $T_b{}^{(L)}$ ranged from $(3.8 \pm 0.6) \times 10^3$ to $(205.0 \pm 173.4) \times 10^3$ K, whereas, from the area where $|r_c| \geq 30\%$, it ranged from $(9.7 \pm 2.3) \times 10^3$ to $(484.2 \pm 186.6) \times 10^3$ K. As for $\left|\vec{\nabla} T_b^{(L)}\right|$, the values corresponding to $|r_c| < 30\%$ ranged from $(4.0 \pm 1.4) \times 10^{-8}$ to $(1.6 \pm 1.2) \times 10^{-4}$ K cm^{-1}, while, for $|r_c| \geq 30\%$, it ranged from $(1.3 \pm 0.8) \times 10^{-5}$ to $(33.1 \pm 13.7) \times 10^{-5}$ K cm^{-1}. Such data then indicate that, among the maps, the average of the maximum results of $T_b{}^{(L)}$ characterized by $|r_c| \geq 30\%$ is 136.154% greater than the average

of the maximum values of ${T_b}^{(L)}$ of low circular polarization. The data also indicate that the average of the maximum values of $\left|\vec{\nabla}T_b^{(L)}\right|$ corresponding to $|r_c| \geq 30\%$ is 111.695% greater than the average of the maximum values of $\left|\vec{\nabla}T_b^{(L)}\right|$ related to $|r_c| < 30\%$. However, the data also show that, from the maps, the average of the maximum values of ${T_b}^{(L)}$ of $|r_c| < 30\%$ is 2021.76% greater than the average of the minimum values of ${T_b}^{(L)}$ of $|r_c| \geq 30\%$, while the average of the maximum results of $\left|\vec{\nabla}T_b^{(L)}\right|$ of $|r_c| < 30\%$ is 1059.37% greater than the average of the minimum results of $\left|\vec{\nabla}T_b^{(L)}\right|$ of $|r_c| \geq 30\%$.

This advantage of low circular polarization brightness variables observed in some areas of the active region is evident in the LHCP-BTG maps (see Figure 6.12(a)) and in the scatter plots (Figures 6.13(a) and 6.13(b)) relating ${T_b}^{(L)}$ and $\left|\vec{\nabla}T_b^{(L)}\right|$ to the circular polarization degree (r_c). In Figure 6.12(a), the low-polarization brightness bump is almost as prominent as the high-polarization one.

Figure 6.13 - Scatter plots related to (a): $T_b^{(L)}$ vs. r_c and (b): $\left|\vec{\nabla}T_b^{(L)}\right|$ vs. r_c for the active region NOAA 11302 at September 26, 2011, 02:00:01 UT.

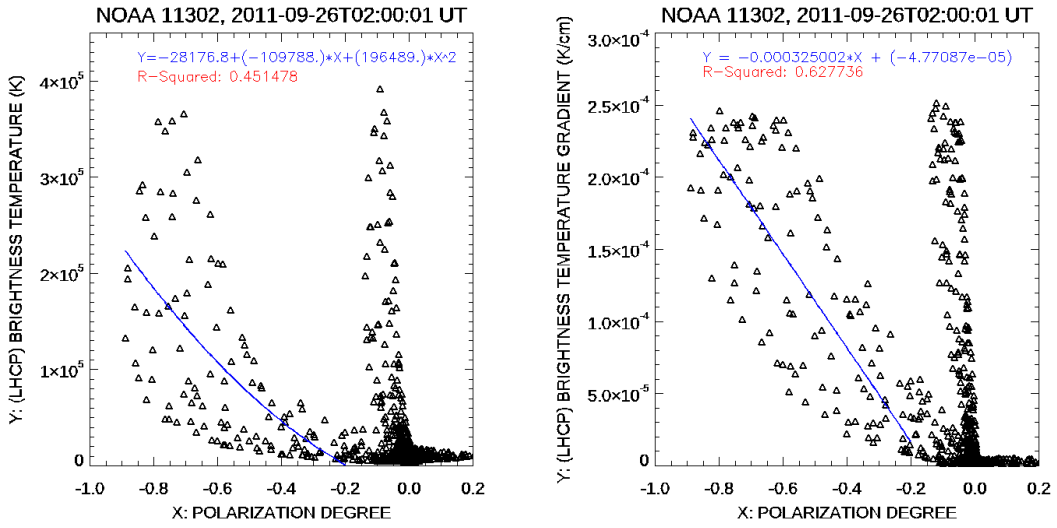

(a) (b)

In Figure 6.13, for each LHCP brightness variable, there is an intense peak around the null polarization. Such a peak, on the other hand, reveals an absence of control of the mechanism(s) associated with the low polarization emission over ${T_b}^{(L)}$ and $\left|\vec{\nabla}T_b^{(L)}\right|$, which can be verified in the correlations presented in Figure 6.14.

Figure 6.14 - Degree of Spearman correlation of $|r_c|$ with (a): $T_b^{(L)}$ and (b): $\left|\vec{\nabla} T_b^{(L)}\right|$ for each NoRH map of the region NOAA 11302 at September 26, 2011. The blue triangles represent the correlation with $|r_c| \geq 30\%$, while the red squares indicate the correlation with $|r_c| < 30\%$. This statistical result has high significance, except, for $|r_c| \geq 30\%$, in the 33rd-35th LHCP-BT maps and in the 33rd-35th LHCP-BTG maps, and, for $|r_c| < 30\%$, in the 6th, 7th, 20th, 23rd, 32nd, 33rd, 36th and 37th LHCP-BT maps, and in the 15th, 20th, 24th, 26th, 29th, 31st, and 34th-37th LHCP-BTG maps.

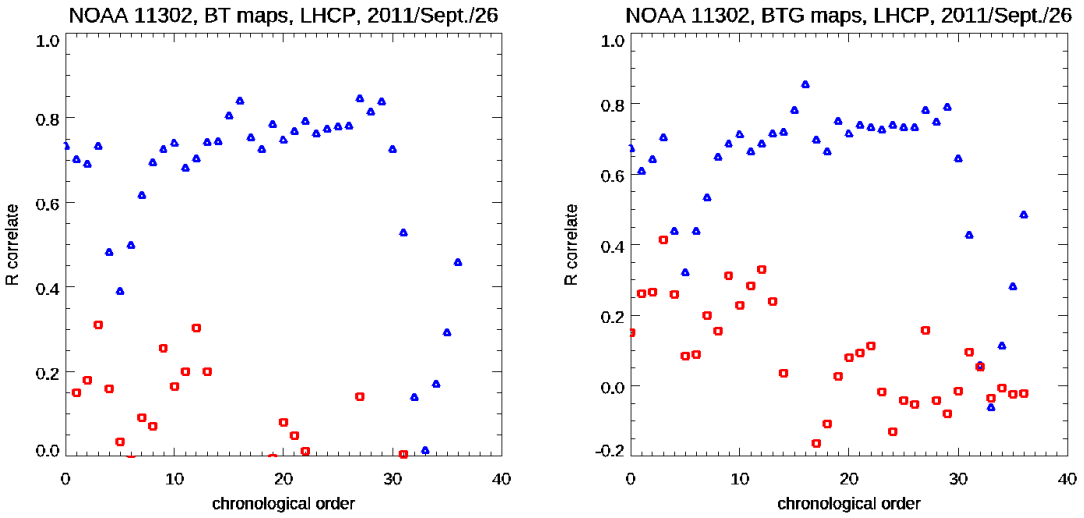

(a) (b)

Such statistical analysis was performed from scatter plots containing 102 to 219 points for $|r_c| \geq 30\%$ and 3502 to 3619 points for $|r_c| < 30\%$. Its result showed a predominance of strong correlations between each LHCP brightness variable and $|r_c| \geq 30\%$, although 9 out of 37 LHCP-BT maps and 10 out of 37 LHCP-BTG maps showed weak to moderate correlations with high polarization degree module. For $|r_c| < 30\%$, the correlations remained between weak and moderate (see the Figures 6.14(a) and 6.14(b)).

For the 37 LHCP-BT maps, the intensity strongly correlates with $|r_c| \geq 30\%$, then, in 76% of such maps. The correlation index showed between 0.70 and 0.85 with a high significance in 64% of LHCP-BT maps. For the other LHCP-BT maps, the correlation with $|r_c| \geq 30\%$ ranged from 0.02 to 0.39 in 5 maps and from 0.46 to 0.69 in 8 maps. The significance of this last interval is also high, but the previous interval presents lower significance: from $\simeq 0$ to 0.83. In turn, the values obtained for the correlation index of $|r_c| < 30\%$ with the LHCP brightness temperature

range from -0.36 to 0.31, a result with excellent significance. From the 37 LHCP-BT maps, eight did not show high significance in the correlation between $T_b^{(L)}$ and $|r_c| < 30\%$. Turning to the correlation between the module of the LHCP brightness temperature gradient and $|r_c| \geq 30\%$, the values presented are from 0.61 to 0.86 (of high significance), in almost 73% of the 37 LHCP-BTG maps; from 0.43 to 0.54, also of high significance, in almost 14% of the LHCP-BTG maps; and from -0.06 to 0.33 in the remaining LHCP-BTG maps. The significance obtained from this weak correlation interval is high only for 2 out of 5 maps. As for the correlation of the LHCP brightness temperature gradient with $|r_c| < 30\%$, the obtained results range from -0.22 and 0.42, in high significance measurements in 27 of the 37 LHCP-BTG maps.

Among the strong correlation values between each LHCP brightness variable and $|r_c| \geq 30\%$, every one of the two low (or medium) correlation sequences starts right after a flare occurrence. According to Solar Monitor[5], the only recorded events coming from this region and occurring from 00:00 to 06:00 UT are the flares of the following classes: C5.2 (at 00:35 UT), C9.5 (at 01:39) and M4.0 (at 05:06). After the first flare, the correlation of ${T_b}^{(L)}$ and $\left|\vec{\nabla} T_b^{(L)}\right|$ with $|r_c| \geq 30\%$, which fluctuates close to 0.70 in the first four maps (until 00:30:01 UT), turns to 0.49, 0.39 and 0.50 in the following three LHCP-BT maps, respectively, and to 0.44, 0.33, 0.44 and 0.54 in the next four LHCP-BTG maps, respectively. After recovering its high level, the correlation of brightness variables with $|r_c| \geq 30\%$ remains strong until the occurrence of the third flare, then assuming low levels again: 0.53, 0.30, and 0.46 in the next and last LHCP-BT maps; and 0.43, 0.29, 0.49 in the next and last LHCP-BTG maps. These statistical results showed high significance.

In analyzing the extrapolated magnetic field of the magnetogram shown in Figure 6.15(a), magnetic field levels associated with the extended 3rd and 4th harmonics near and over the brightness bumps were also identified (see Figure 6.15(b)). In this case, there is no indication of participation of the extended 3rd harmonic in generating the brightness bump. On the other hand, the magnetic levels associated with the extended 4th harmonic emerge over a significant portion of the brightness bump. In this same finding, it was also found that the 30% broadening of the 4th harmonic fits the brightness bump better. The estimated heights for the extrapolated magnetic field corresponding to the extended harmonic levels are available in Table 6.3.

[5]https://solarmonitor.org/?date=20110926

Figure 6.15 - Region NOAA 11302 at September 26, 2011: (a) SDO-HMI magnetogram (at 01:59:10 UT) and (b) its extrapolated magnetic field level lines over expanded LHCP-BTG map (at 02:00:01 UT). (b): The dotted lines indicate magnetic field strengths corresponding to extended 3rd harmonic, while the thick lines (except the red one) indicate fields associated with extended 4th harmonic. (b): Represented by the colors in the lines, the broadening of the harmonics are +5% (white), +10% (orange), +15% (green), +20% (light blue), and +30% (dark blue).

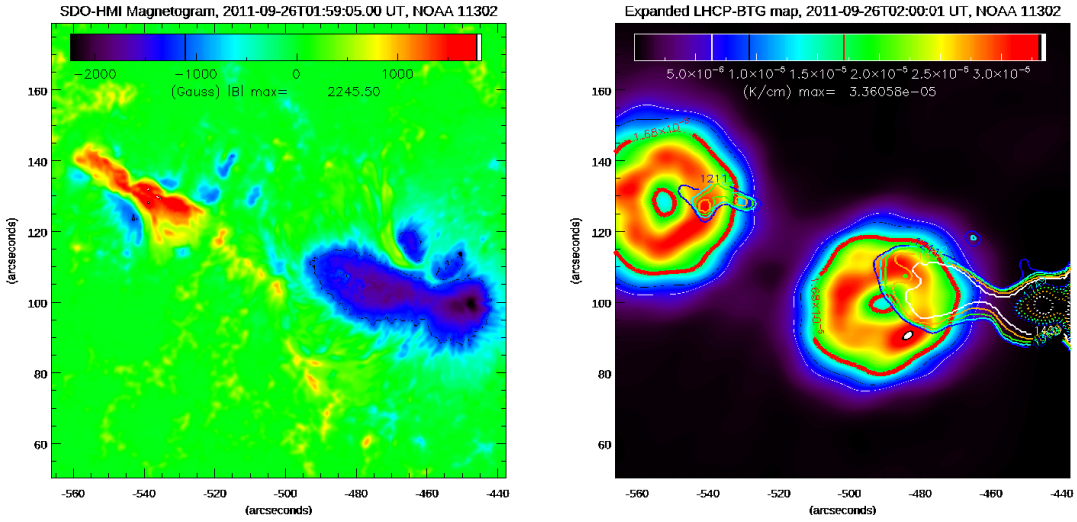

(a) (b)

Source: Figure (a): Adapted from NASA (2011).

Table 6.3 - For region NOAA 11302 at September 26, 2011: Height (in Km) of the extrapolated magnetic fields associated with the extended harmonics.

Harmonic	±5%	±10%	±15%	±20%	±30%
3rd	350	350-700	350-1050	350-1400	350-2100
4th	350-1750	350-2100	350-2450	350-2800	350-3850

6.1.3 Active region NOAA 11384 (December 26, 2011)

Moving on to observe this region, the present work also found the predominance of left-hand circularly polarized emission at 17 GHz with $|r_c| \geq 30\%$ coming from the area of highlighted brightness enhancement (see Figure 6.16(a)). In this case, the polarization maxima reached among the 20 BTG maps of this region lies between 40% and 80%. Concerning the inclination between the extrapolated magnetic field

and the line of sight, Figure 6.16(b) shows the highly polarized brightness bump under weakly tilted field lines from a magnetogram corresponding to 02:28:40 UT.

Figure 6.16 - LHCP-BTG maps of region NOAA 11384 (at December 26, 2011, 03:10:02 UT) on which are white contours of: (a) the high circular polarization and (b) the cosine of the angle between the extrapolated magnetic field and the line of sight. This extrapolation considered $\alpha = 0.0$ and a cube size of 256^3 voxels over this area. The red thick-line contour indicates half of the maximum value of $\left|\vec{\nabla} T_b^{(L)}\right|$ in each map.

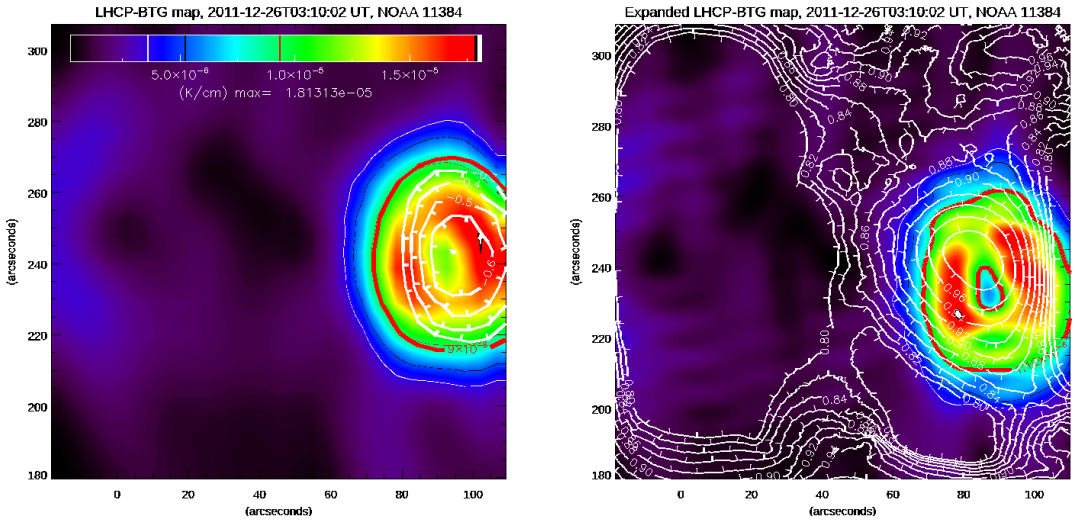

(a) (b)

From the area outside the brightness bump, the emission at 17 GHz was permanently characterized by its low degree of polarization. From this area, where $|r_c| < 30\%$, the $T_b{}^{(L)}$ measurements presented values between $(4.5 \pm 0.3) \times 10^3$ and $(18.8 \pm 2.0) \times 10^3$ K, whereas from the area where $|r_c| \geq 30\%$, the $T_b{}^{(L)}$ presented measurements between $(10.7 \pm 1.1) \times 10^3$ and $(30.9 \pm 7.0) \times 10^3$ K. Then, among the maps, the advantage of the average of the maximum values of $T_b{}^{(L)}$ corresponding to $|r_c| \geq 30\%$ over the average of the maximum values of the low-polarization $T_b{}^{(L)}$ is 64%. However, it is also observed, among the maps, that the average of the maximum results of $T_b{}^{(L)}$ corresponding to $|r_c| < 30\%$ exceeds by 75% the average of the minimum results of $T_b{}^{(L)}$ associated with $|r_c| \geq 30\%$.

The $\left|\vec{\nabla} T_b^{(L)}\right|$ measurements, in turn, ranged between $(1.1 \pm 0.3) \times 10^{-8}$ and $(1.4 \pm 0.4) \times 10^{-5}$ K cm^{-1} from where $|r_c| < 30\%$, and between $(7.8 \pm 2.3) \times 10^{-6}$ and $(1.6 \pm 0.5) \times 10^{-5}$ K cm^{-1} from where $|r_c| \geq 30\%$. Hence, it was verified, among

the maps, that the average of the maximum values of $\left|\vec{\nabla}T_b^{(L)}\right|$ related to $|r_c| \geq 30\%$ exceeds by 12.25% the average of the maximum values of $\left|\vec{\nabla}T_b^{(L)}\right|$ corresponding to $|r_c| < 30\%$. However, it was also found, in the maps, that the average of the maximum results of $\left|\vec{\nabla}T_b^{(L)}\right|$ related to $|r_c| < 30\%$ is 81.53% greater than the average of the minimum results of $\left|\vec{\nabla}T_b^{(L)}\right|$ corresponding to $|r_c| \geq 30\%$.

Such results then reveal a tendency for high polarization brightness variables, associated with the gyroresonance, to have an advantage over low polarization brightness variables. However, they also show that low-polarization brightness variables can outperform brightness variables associated with such a mechanism. In addition to the finding of the advantage of highly polarized brightness variables at 17 GHz, is also observed a significant advantage of the mechanism control associated with $|r_c| \geq 30\%$ over the ${T_b}^{(L)}$ (see the Figures 6.17(a) and 6.18(a)). In Figure 6.18(a), it is verified that in almost all LHCP-BT maps, the ${T_b}^{(L)}$ is strongly correlated with $|r_c| \geq 30\%$ (except for two of such maps) and weakly correlated with $|r_c| < 30\%$. For each of the two LHCP-BT maps where such correlation with $|r_c| \geq 30\%$ was not strong, the result is 0.54 and 0.55, respectively, while among the remaining 18 LHCP-BT maps, this correlation ranged from 0.70 to 0.89. In the analysis of the correlation between ${T_b}^{(L)}$ and $|r_c| < 30\%$, the highly significant result varies between 0.06 and 0.36. The correlation of ${T_b}^{(L)}$ showed high significance, except with $|r_c| < 30\%$ only in 2 out of 20 maps.

Figure 6.17 - Scatter plots related to (a): $T_b^{(L)}$ vs. r_c and (b): $\left|\vec{\nabla}T_b^{(L)}\right|$ vs. r_c for the active region NOAA 11384 at December 26, 2011, 03:10:02 UT.

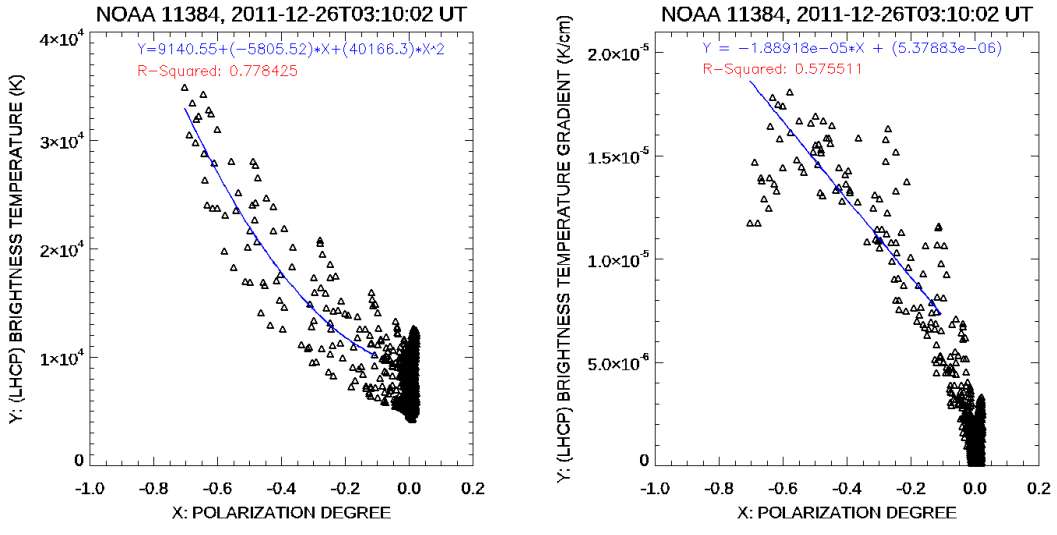

(a) (b)

The $T_b{}^{(L)}$ data from this region then corroborate with the association between the gyroresonance and the brightness increase at 17 GHz. However, for a cause yet to be investigated, the statistical analysis of the $\left|\vec{\nabla}T_b^{(L)}\right|$ did not support such an association, which can be verified in Figures 6.17(b) and 6.18(b), where the $\left|\vec{\nabla}T_b^{(L)}\right|$ does not correlate well with either $|r_c| \geq 30\%$ and with $|r_c| < 30\%$. However, such a weak correlation of gradient results of highly polarized emission has high significance only in 4 out of 20 LHCP-BTG maps. In addition, this result does not necessarily imply a supposed absence of control of the gyroresonance on the brightness at 17 GHz. For low polarized emission, the correlation of $\left|\vec{\nabla}T_b^{(L)}\right|$ has high significance in every map.

Figure 6.18 - Degree of Spearman correlation of $|r_c|$ with (a): $T_b^{(L)}$ and (b): $\left|\vec{\nabla}T_b^{(L)}\right|$ for each NoRH map of the region NOAA 11384 at December 26, 2011. The blue triangles represent the correlation with $|r_c| \geq 30\%$, while the red squares indicate the correlation with $|r_c| < 30\%$. The statistical significance of these results is high in the $T_b{}^{(L)}$ correlation, except in the 3rd and 11th LHCP-BT maps with $|r_c| < 30\%$. For $\left|\vec{\nabla}T_b^{(L)}\right|$, the correlation with $|r_c| < 30\%$ is of high significance in all maps, but the low correlation of this gradient with $|r_c| \geq 30\%$ is high only in the 8th, 13th, 14th, and 15th LHCP-BTG maps.

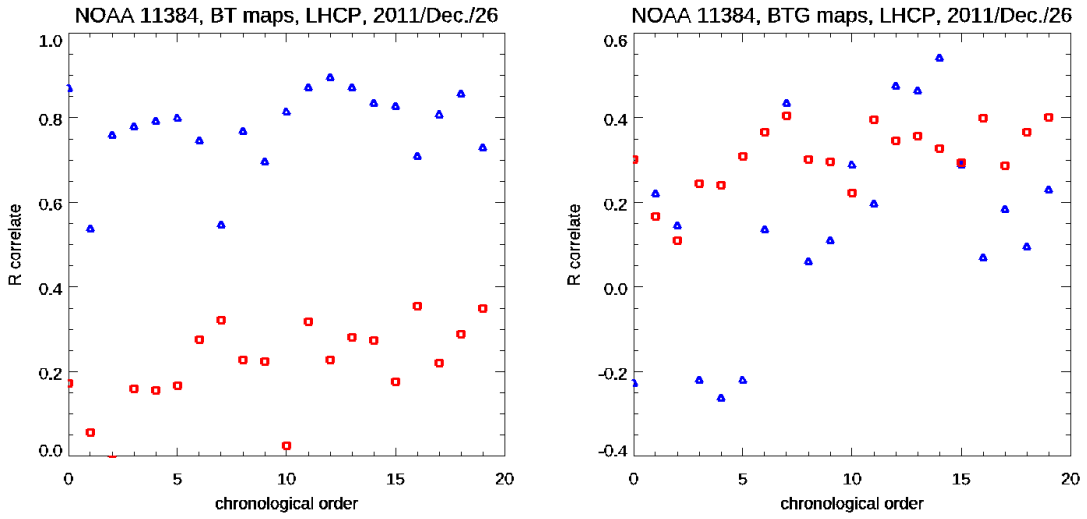

(a) (b)

From the magnetogram extrapolation (Figure 6.19(a)) of this region, in turn, the magnetic field respectively associated with both extended 3rd and 4th harmonics emerged from the brightness bump (Figure 6.19(b)). In this observation, there was

also a prevalence of the broadened 4th harmonic, especially at the 30% broadening. The estimated heights of the extrapolated magnetic fields associated with the extended harmonics are shown in Table 6.4. According to the Solar Monitor[6], no flare was recorded during the capture of the 17 GHz images of this region, which excludes the possibility of the influence of non-thermal emission mechanisms.

Figure 6.19 - Region NOAA 11384 at December 26, 2011: (a) SDO-HMI magnetogram (at 02:38:40 UT) and (b) its extrapolated magnetic field level lines over expanded LHCP-BTG map (at 03:10:02 UT). (b): The dotted lines indicate magnetic field strengths corresponding to extended 3rd harmonic, while the thick lines (except the red one) indicate fields associated with extended 4th harmonic. (b): Represented by the colors in the lines, the broadening of the harmonics are +5% (white), +10% (orange), +15% (green), +20% (light blue), and +30% (dark blue).

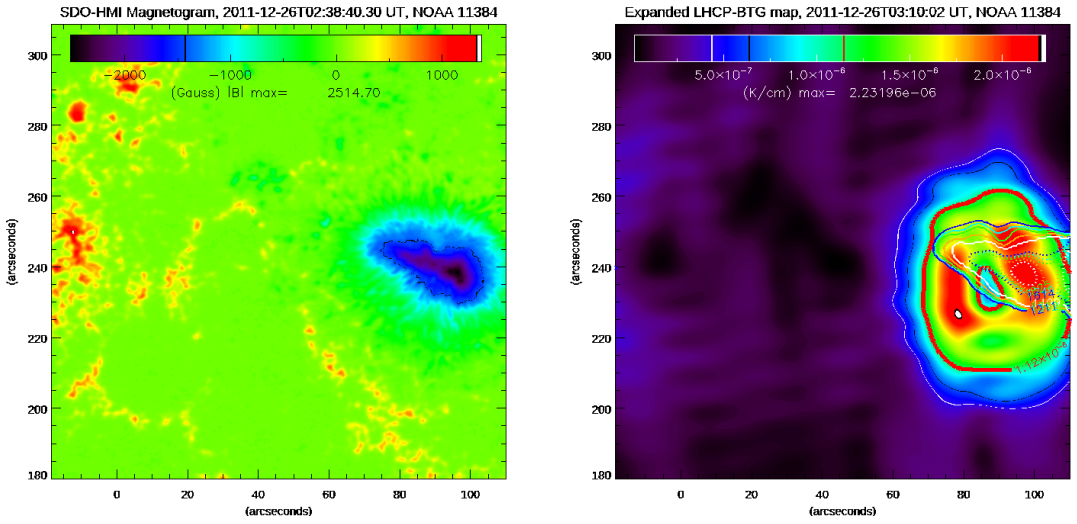

(a) (b)

Source: Figure (a): Adapted from NASA (2011).

Table 6.4 - For region NOAA 11384 at December 26, 2011: Height (in Km) of the extrapolated magnetic fields associated with the extended harmonics.

Harmonic	±5%	±10%	±15%	±20%	±30%
3rd	350-700	350-1050	350-1050	350-1400	350-2100
4th	350-2100	350-2450	350-2800	350-3150	350-3850

[6]https://solarmonitor.org/?date=20111226

6.1.4 Active region NOAA 11476 (May 10, 2012)

In contrast to the previous regions, this one promoted several flares, according to the Solar Monitor[7], during the 17 GHz imaging performed by NoRH on May 10, 2012. Table 6.5 presents the classification and time associated with each event. In this high activity condition, a highly polarized brightness bump corresponding to 01:50:02 UT was found to occur under extrapolated magnetic field lines of low inclination with the line of sight (see the Figures 6.20(a) and 6.20(b)).

Table 6.5 - Flares produced by NOAA 11476 during the NoRH operation on May 10, 2012, according to Solar Monitor[9].

Schedule (UT)	01:44	01:57	02:09	04:11	05:04	05:17	05:55	06:19
Event	C2.4	C1.9	C1.2	M5.7	C7.9	C8.3	C3.1	C3.6

Figure 6.20 - LHCP-BTG maps of region NOAA 11476 (at May 10, 2012, 01:50:02 UT) on which are white contours of: (a) the high circular polarization and (b) the cosine of the angle between the extrapolated magnetic field and the line of sight. This extrapolation considered $\alpha = 0.0$ and a cube size of 256^3 voxels over this area. The red thick-line contour indicates half of the maximum value of $\left|\vec{\nabla} T_b^{(L)}\right|$ in each map.

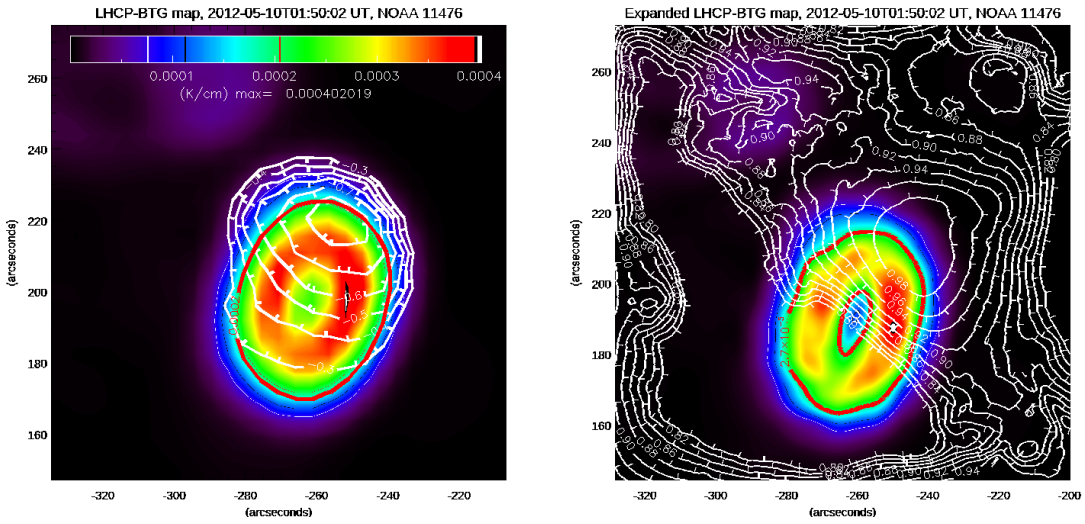

(a) (b)

[7] https://www.solarmonitor.org/index.php?date=20120510

Since the contours of the characteristic magnetic field appeared in only 3 out of 13 obtained maps, the high frequency of flares likely weakened the gyroresonance process. In this context, the statistical analysis only reveals correlations that rank between weak and moderate in the relationship of the brightness variables with $|r_c| \geq 30\%$ and $|r_c| < 30\%$ (see the Figures 6.21 and 6.22).

Figure 6.21 - Scatter plots related to: (a): $T_b^{(L)}$ vs. r_c, and (b): $\left|\vec{\nabla} T_b^{(L)}\right|$ vs. r_c for the active region NOAA 11476 at May 10, 2012, 01:50:02 UT.

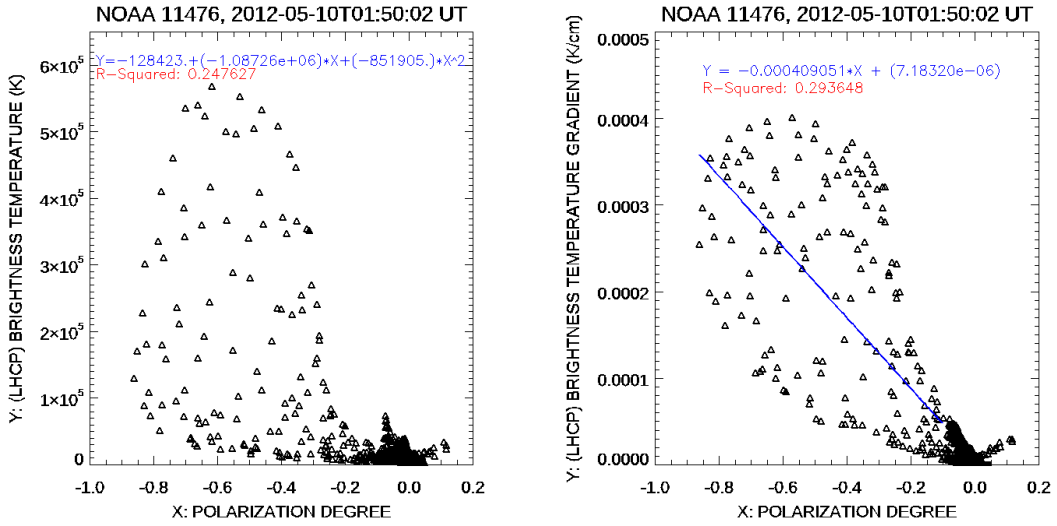

(a) (b)

The high significance in the correlation with $|r_c| < 30\%$ was observed in almost all maps except in 1 LHCP-BT map. For $|r_c| \geq 30\%$, the correlation is highly significant in 6 out of 13 LHCP-BT maps and 11 out of 13 LHCP-BTG maps. The high degree of polarization revealed on the brightness bumps, as shown by Figure 6.20(a), then suggests that even though another highly polarized emission mechanism can cause brightness intensification at 17 GHz, such a radiative process did not promote brightness temperature control at this frequency.

Figure 6.22 - Degree of Spearman correlation of $|r_c|$ with (a): $T_b^{(L)}$ and (b): $\left|\vec{\nabla} T_b^{(L)}\right|$ for each NoRH map of the region NOAA 11476 at May 10, 2012. The blue triangles represent the correlation with $|r_c| \geq 30\%$, while the red squares indicate the correlation with $|r_c| < 30\%$. For $|r_c| < 30\%$, only the 9th LHCP-BT map did not show high significance in the correlation. For $|r_c| \geq 30\%$, highly significant correlations were found only in 1st, 3rd-5th, 7th, and 11th LHCP-BT maps and in 1st, 2nd-5th, 7th, 8th, 10th-13rd LHCP-BTG maps.

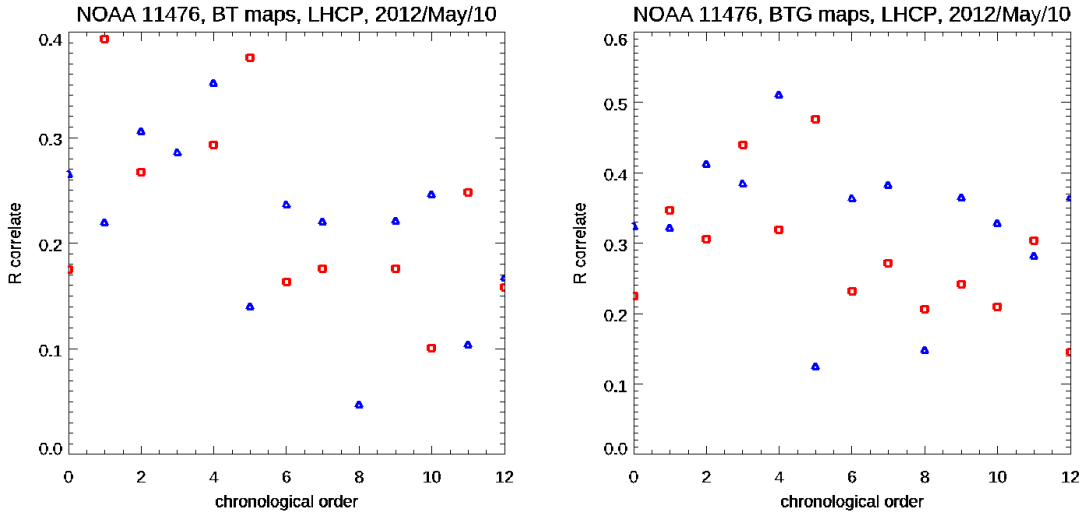

(a) (b)

Although these data do not corroborate a brightness control performed by a gyroresonance mechanism, the extrapolated magnetic field (Figure 6.23(b)) indicates the presence, over the brightness bump, of field lines associated with such a radio mechanism. Similar to the many other cases analyzed in this work, the extended 4th harmonic (better than the extended 3rd harmonic) fits the bump well. The magnetogram used for extrapolation corresponds to 01:49:23 UT (Figure 6.23(a)). Table 6.6 shows the estimated height values for the extrapolated magnetic fields associated with these extended harmonics.

Figure 6.23 - Region NOAA 11476 at May 10, 2012: (a) SDO-HMI magnetogram (at 01:49:23 UT) and (b) its extrapolated magnetic field level lines over expanded LHCP-BTG map (at 01:50:02 UT). (b): The dotted lines indicate magnetic field strengths corresponding to extended 3rd harmonic, while the thick lines (except the red one) indicate fields associated with extended 4th harmonic. (b): Represented by the colors in the lines, the broadening of the harmonics are +5% (white), +10% (orange), +15% (green), +20% (light blue), and +30% (dark blue).

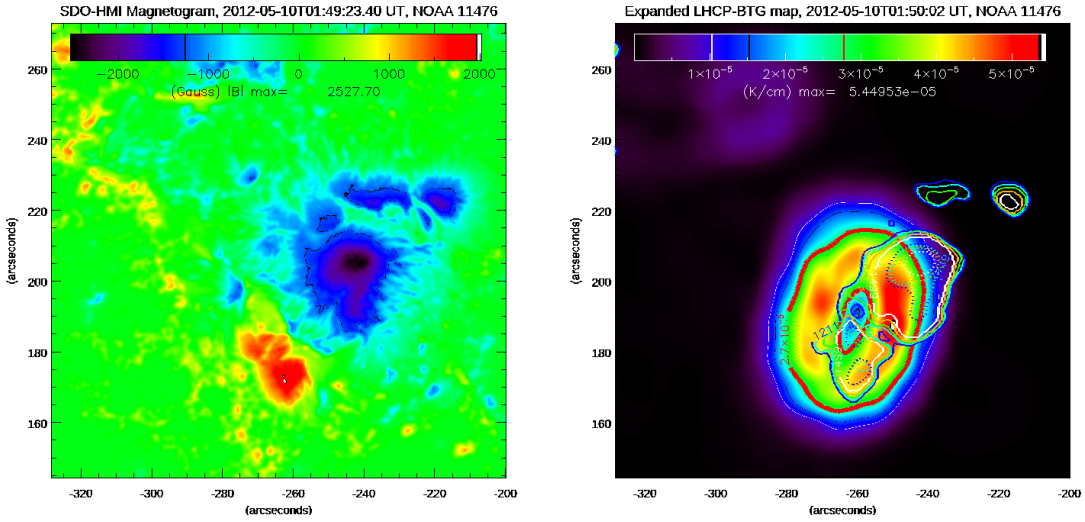

(a) (b)

Source: Figure (a): Adapted from NASA (2012).

Table 6.6 - For region NOAA 11476 at May 10, 2012: Height (in Km) of the extrapolated magnetic fields associated with the extended harmonics.

Harmonic	±5%	±10%	±15%	±20%	±30%
3rd	350-700	350-1050	350-1400	350-1750	350-2800
4th	350-2450	350-2800	350-3150	350-3850	350-4900

6.1.5 Active region NOAA 11504 (June 14, 2012)

With right-hand circular polarization, this region also showed an area of prominent brightness intensification with $|r_c| \geq 30\%$ in each of its 26 RHCP-BTG maps. The upper level of polarization was beyond 60% in most of these maps, as the example presented by the Figure 6.24(a). From the extrapolated magnetic fields of 02:04:26 UT magnetogram (Figure 6.27(a)), a set of lines of low inclination with the line of

sight emerged over the 02:05:00 UT bump (see the Figure 6.24(b)).

Figure 6.24 - RHCP-BTG maps of region NOAA 11504 (at June 14, 2012, 02:05:00 UT) on which are white contours of: (a) the high circular polarization and (b) the cosine of the angle between the extrapolated magnetic field and the line of sight. This extrapolation considered $\alpha = 0.20$ and a cube size of 400^3 voxels over this area. The red thick-line contour indicates half of the maximum value of $\left|\vec{\nabla} T_b^{(R)}\right|$ in each map.

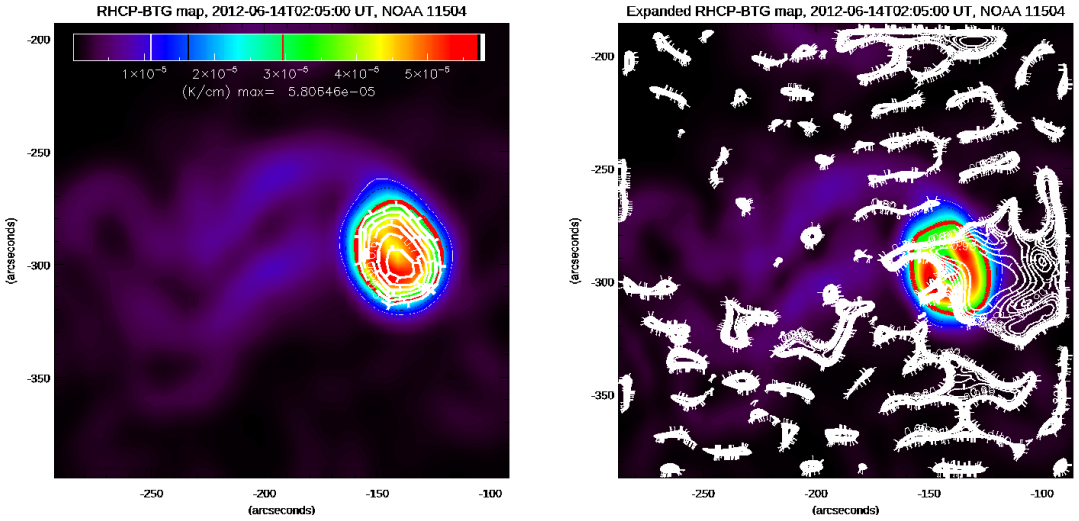

(a) (b)

From the surrounding area, with $|r_c| < 30\%$, the variation of $T_b{}^{(R)}$ occurred from $(4.8 \pm 0.1) \times 10^3$ to $(37.9 \pm 9.8) \times 10^3$ K, while for $|r_c| \geq 30\%$, the $T_b{}^{(R)}$ ranged from $(14.4 \pm 1.3) \times 10^3$ to $(101.3 \pm 14.8) \times 10^3$ K. The average of the maximum results of $T_b{}^{(R)}$ corresponding to $|r_c| \geq 30\%$ from all the maps, hence, is 167.585% greater than the average of the maximum values of $T_b{}^{(R)}$ associated with $|r_c| < 30\%$. This last average, in turn, is 163.270% greater than the average of the minimum values of $T_b{}^{(R)}$ corresponding to $|r_c| \geq 30\%$.

Moving on to analyze $\left|\vec{\nabla} T_b^{(R)}\right|$, it was found that such brightness variable corresponding to $|r_c| < 30\%$ ranged from $(3.6 \pm 0.8) \times 10^{-8}$ to $(4.1 \pm 0.6) \times 10^{-5}$ K cm^{-1}, while for $|r_c| \geq 30\%$, it was between $(2.7 \pm 0.5) \times 10^{-5}$ and $(6.7 \pm 1.2) \times 10^{-5}$ K cm^{-1}. Using these data, then, it was found that the average of the maximum results of $\left|\vec{\nabla} T_b^{(R)}\right|$ associated with $|r_c| \geq 30\%$ proved to be 64.7460% higher than the average of the maximum values of $\left|\vec{\nabla} T_b^{(R)}\right|$ corresponding to $|r_c| < 30\%$. This last

average, on the other hand, is 51.9252% greater than the average of the minimum results of $\left|\vec{\nabla} T_b^{(R)}\right|$ associated with $|r_c| \geq 30\%$.

The scatter of these data has 2536 to 2552 points for $|r_c| < 30\%$ and 49 to 65 points for $|r_c| \geq 30\%$. Figures 6.25(a) and 6.25(b) present samples of these data clouds, corroborating the relationship between the intense circular polarization and the brightness variables at 17 GHz.

Figure 6.25 - Scatter plots related to (a): $T_b^{(R)}$ vs. r_c, and (b): $\left|\vec{\nabla} T_b^{(R)}\right|$ vs. r_c for the active region NOAA 11504 at June 14, 2012, 02:05:00 UT.

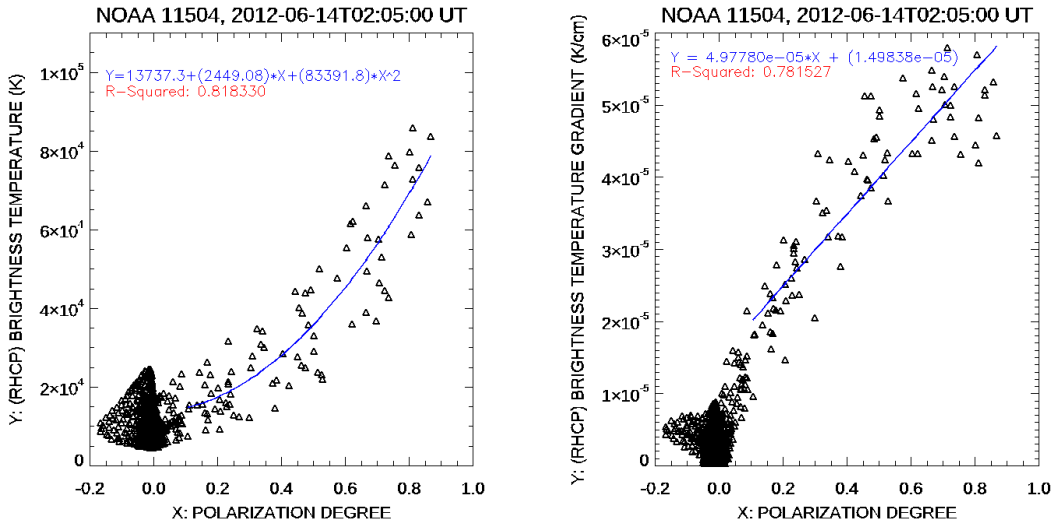

(a) (b)

The statistical analysis, as shown in Figures 6.26(a) and 6.26(b), indicates the intense circular polarization brightness variables correlating strongly with $|r_c|$ in all RHCP-BTG maps and 19 out of 26 RHCP-BT maps, while $|r_c|$ is weakly correlated with the low circular polarization brightness variables in the RHCP maps (see the Figures 6.26). Then, $|r_c| \geq 30\%$ shows correlation from 0.61 to 0.92 with $T_b{}^{(R)}$ among all maps, and from 0.65 to 0.93 with $\left|\vec{\nabla} T_b^{(R)}\right|$ among 19 out of 26 maps. Among the remaining 7 RHCP-BTG maps, the correlation between its presented brightness variable and $|r_c| \geq 30\%$ is moderate: between 0.44 and 0.56. In turn, $|r_c| < 30\%$ indicates correlation of -0.07 to 0.30 with $T_b{}^{(R)}$, and of 0.10 to 0.38 with $\left|\vec{\nabla} T_b^{(R)}\right|$. Almost all correlation data showed high significance, except with $|r_c| < 30\%$ in 1 out of 26 RHCP-BT maps.

Figure 6.26 - Degree of Spearman correlation of $|r_c|$ with (a): $T_b^{(R)}$ and (b): $\left|\vec{\nabla} T_b^{(R)}\right|$ for each NoRH map of the region NOAA 11504 at June 14, 2012. The blue triangles represent the correlation with $|r_c| \geq 30\%$, while the red squares indicate the correlation with $|r_c| < 30\%$. Only the 24th RHCP-BT map did not show a high significance correlation, which in this case was for $|r_c| < 30\%$.

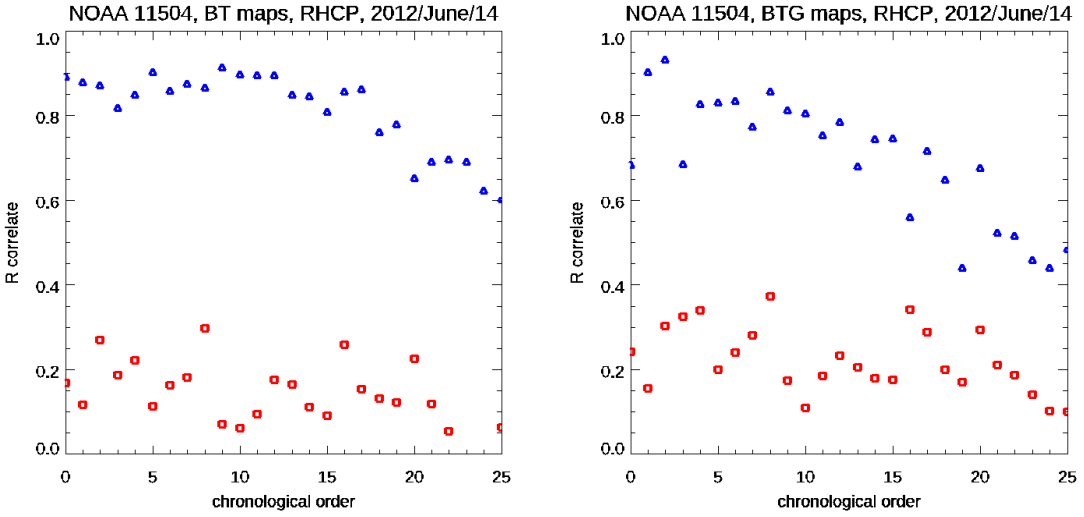

(a) (b)

On the record of events, the Solar Monitor[10] indicates the occurrence of 2 C-class flares. The first occurred at 01:43 UT, and the second at 04:59 UT. Although it is not clear whether such events have produced effects on the correlation between each RHCP brightness variable and $|r_c| \geq 30\%$, it was recorded for the $\left|\vec{\nabla} T_b^{(R)}\right|$ data, a drop of correlation from 0.93 (at 01:35 UT) to 0.69 (at 02:05 UT). And five minutes before the second flare, the correlation drops to its second-lowest value: 0.44. Such statistical results showed high significance.

The extrapolation of the magnetogram (Figure 6.27(a)), in turn, indicates, on one side of the brightness bump, an emergence of a magnetic field corresponding to the extended 3rd and 4th harmonics (Figure 6.27(b)), with some advantage of the extended 4th over the extended 3rd in brightness bump extension.

[10] https://www.solarmonitor.org/index.php?date=20120614

Figure 6.27 - Region NOAA 11504 at June 14, 2012: (a) SDO-HMI magnetogram (at 02:04:26 UT) and (b) its extrapolated magnetic field level lines over expanded RHCP-BTG map (at 02:05:00 UT). (b): The dotted lines indicate magnetic field strengths corresponding to extended 3rd harmonic, while the thick lines (except the red one) indicate fields associated with extended 4th harmonic. (b): Represented by the colors in the lines, the broadening of the harmonics are +5% (white), +10% (orange), +15% (green), +20% (light blue), and +30% (dark blue).

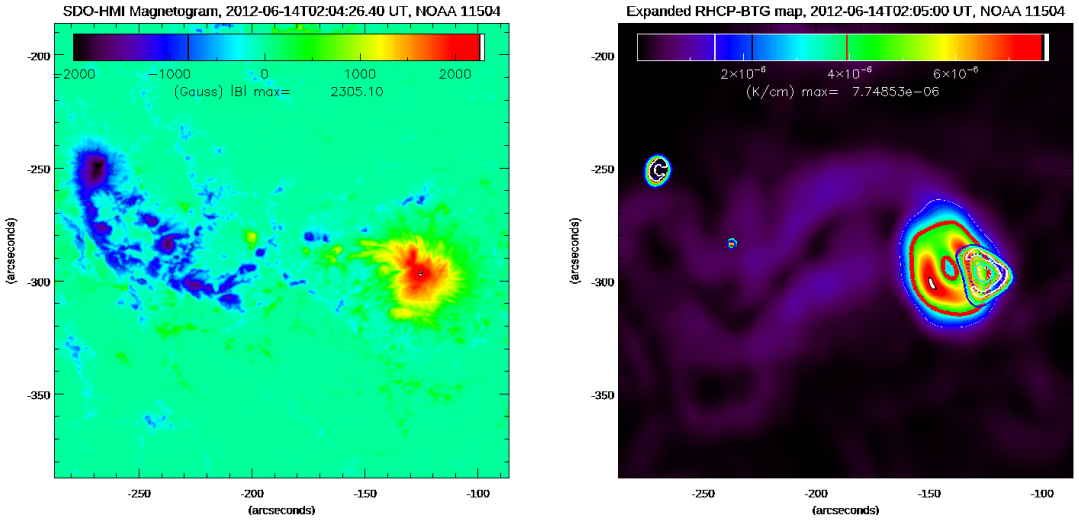

(a) (b)

Source: Figure (a): Adapted from NASA (2012).

6.1.6 Active region NOAA 11520 (July 14, 2012)

Moving on to the analysis of this region, this work also found a high-polarization source characterized by its highlighted gradient of brightness temperature (see Figure 6.28(a)), which was observed in all of its 21 RHCP-BTG maps, with polarization peaks lying between 50% and 65%.

Magnetogram extrapolation, in turn, indicated a distribution of low-slope lines with the line of observation over a high-polarization brightness bump (see the Figure 6.28(b)). The magnetogram used in this procedure corresponds to 01:34:24 UT (Figure 6.31(a)), and the brightness bump overlaid by the extrapolated field corresponds to 01:35:02 UT.

Concerning the highly polarized brightness temperature, the ${T_b}^{(R)}$ was between (1.9 $\pm$ 0.3) $\times$ 10^4 and (2.9 $\pm$ 0.5) $\times$ 10^5 K, whereas, from the low-polarization emission, the ${T_b}^{(R)}$ was between (4.0 $\pm$ 0.6) $\times$ 10^3 and (2.4 $\pm$ 0.5) $\times$ 10^5 K. Such data,

therefore, indicate a 21.2121% overrun of the average of the maximum values of the high-polarization ${T_b}^{(R)}$ over the average of the maximum results of the low-polarization ${T_b}^{(R)}$. Conversely, they also show an overrun of 1128.98% of the average of the maximum values of the low-polarization ${T_b}^{(R)}$ over the average of the minimum results of the high-polarization ${T_b}^{(R)}$.

Figure 6.28 - RHCP-BTG maps of region NOAA 11520 (at July 14, 2012, 01:35:02 UT) on which are white contours of: (a) the high circular polarization and (b) the cosine of the angle between the extrapolated magnetic field and the line of sight. This extrapolation considered $\alpha = 0.10$ and a cube size of 399^3 voxels over this area. The red thick-line contour indicates half of the maximum value of $\left|\vec{\nabla} T_b^{(R)}\right|$ in each map.

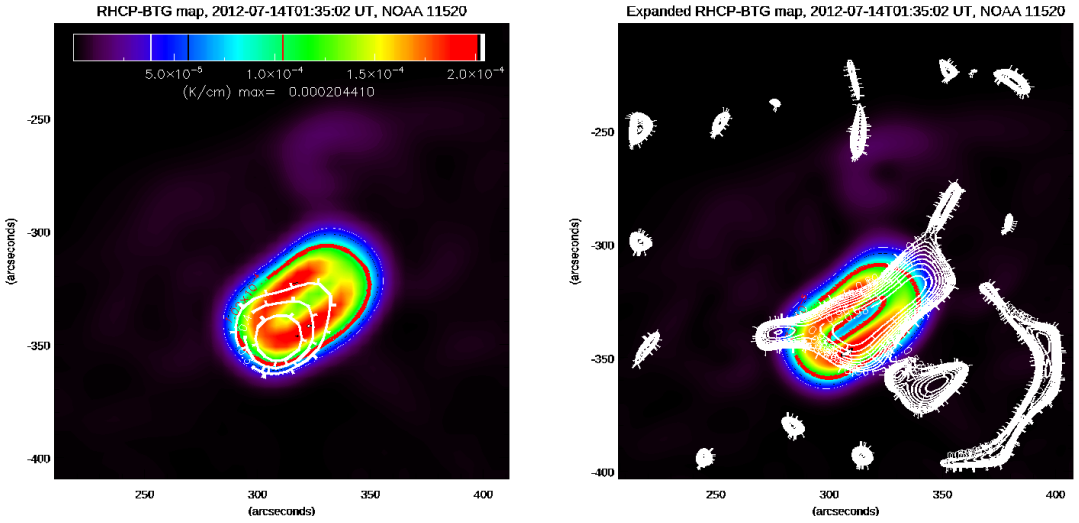

(a) (b)

Concerning the module of the brightness temperature gradient, from the area of intense polarization, $\left|\vec{\nabla} T_b^{(R)}\right|$ ranged from $(6.3 \pm 0.9) \times 10^{-5}$ to $(2.0 \pm 0.5) \times 10^{-4}$ K cm^{-1}, whereas, from the low-polarization area, the $\left|\vec{\nabla} T_b^{(R)}\right|$ ranged from $(3.5 \pm 0.7) \times 10^{-8}$ to $(1.8 \pm 0.5) \times 10^{-4}$ K cm^{-1}. This means that the average of the maximum results of the high circular polarization $\left|\vec{\nabla} T_b^{(R)}\right|$ exceeds the average of the maximum values of the low-polarization $\left|\vec{\nabla} T_b^{(R)}\right|$ by 10.5451%. On the other hand, it also indicates that the average of the maximum results of the low-polarization $\left|\vec{\nabla} T_b^{(R)}\right|$ exceeds the average of the minimum results from the high-polarization $\left|\vec{\nabla} T_b^{(R)}\right|$ by 187.941%.

For the statistical analysis, the 17 GHz maps provided scatterings of 3648 to 3669 points relating the brightness variables with low-polarization degree and of 52 to 73 points associating such variables with high-polarization degree (see Figures 6.29(a) and 6.29(b)). The results then obtained from these data, presented in Figures 6.30(a) and 6.30(b), unlike most of the cases of the active regions analyzed in this work, show low to a medium correlation between each brightness variable and $|r_c| \geq 30\%$.

Figure 6.29 - Scatter plots related to (a): $T_b^{(R)}$ vs. r_c, and (b): $\left|\vec{\nabla} T_b^{(R)}\right|$ vs. r_c for the active region NOAA 11520 at July 14, 2012, 01:35:02 UT. In these graphs, the fitting curve considers the polarization starting at 0.01.

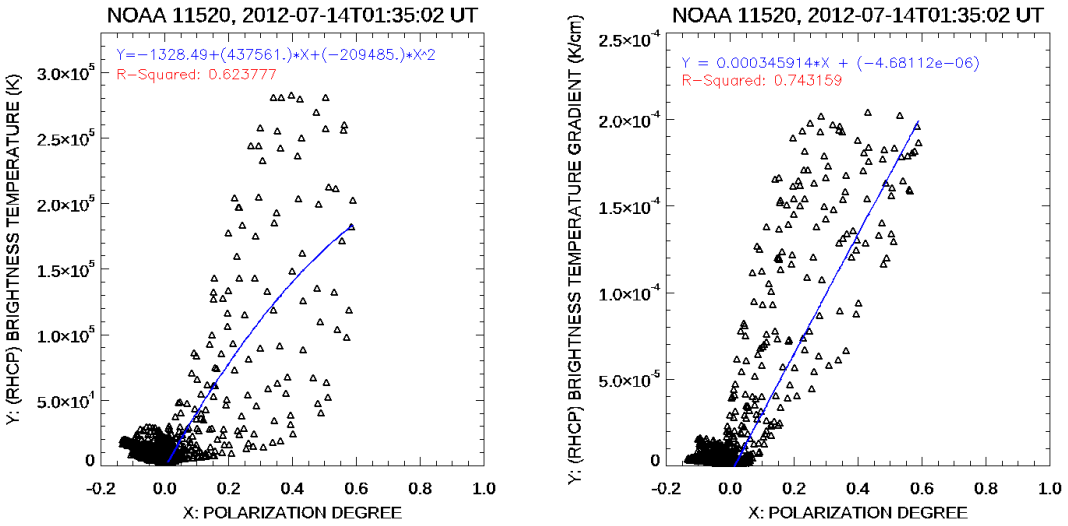

(a) (b)

In this case, such fact indicates low participation of the gyroresonance on the brightness control at 17 GHz or the absence of such mechanism, given the occurrence of two flares: a C5.0 at 03:00 UT, and an M1.0 at 04:51 UT, according to the Solar Monitor[11]. Corroborating with this result, the absence of the characteristic magnetic field contours was also observed in 10 out of the 21 maps of this region. Among the values obtained for the correlation between each brightness variable and $|r_c| \geq 30\%$, only the one presented by the 15th RHCP-BTG map reached a high level, a result that is also highly significant. Such correlation with $|r_c| \geq 30\%$ obtained high significance in 12 out of 21 RHCP-BT maps and 16 out of 21 RHCP-BTG maps. On the other hand, similarly to the other cases, the correlation of $|r_c| < 30\%$ with each

[11] https://solarmonitor.org/?date=20120714

brightness variable remains between low and medium, with great significance (see the Figures 6.30(a) and 6.30(b)).

Figure 6.30 - Degree of Spearman correlation of $|r_c|$ with (a): $T_b^{(R)}$ and (b): $\left|\vec{\nabla} T_b^{(R)}\right|$ for each NoRH map of the region NOAA 11520 at July 14, 2012. The blue triangles represent the correlation with $|r_c| \geq 30\%$, while the red squares indicate the correlation with $|r_c| < 30\%$. All correlations with $|r_c| < 30\%$ obtained high significance. For $|r_c| \geq 30\%$, highly significant correlations occurred: in the 9th, 10th, and 12th-21st RHCP-BT maps; and in the 5th, 7th-21st RHCP-BTG maps.

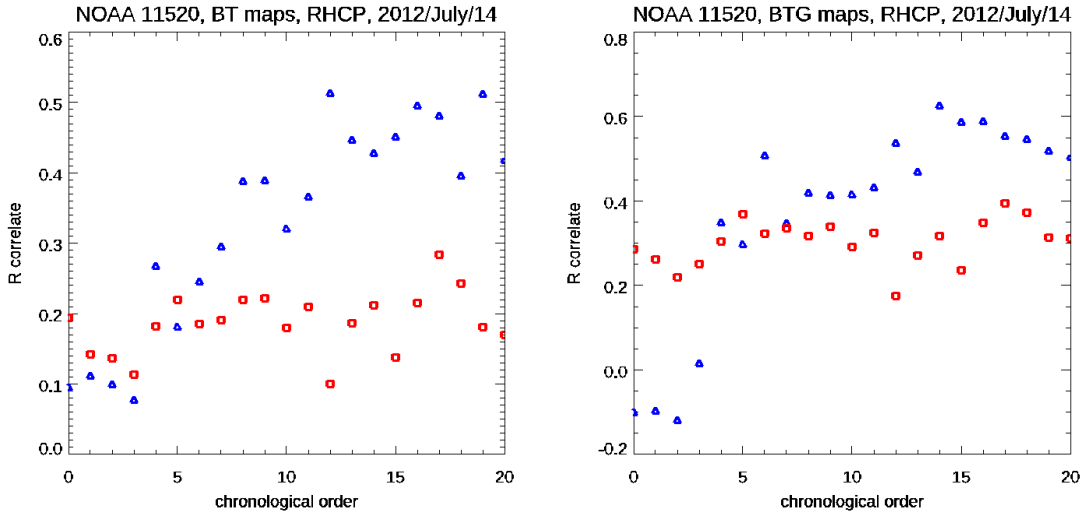

(a) (b)

Despite the low correlations related to the high polarization in this region, the extrapolation of its magnetogram (Figure 6.31(a)) points to an emergence, superimposed on the brightness bump, of a magnetic field associated with the extended 3rd and 4th harmonics (Figure 6.31(b)). In this case, the extended 4th harmonic has a vast advantage over the extended 3rd harmonic, which is indicated by 1 level only.

Figure 6.31 - Region NOAA 11520 at July 14, 2012: (a) SDO-HMI magnetogram (at 01:34:25 UT) and (b) its extrapolated magnetic field level lines over expanded RHCP-BTG map (at 01:35:02 UT). (b): The dotted lines indicate magnetic field strengths corresponding to extended 3rd harmonic, while the thick lines (except the red one) indicate fields associated with extended 4th harmonic. (b): Represented by the colors in the lines, the broadening of the harmonics are +5% (white), +10% (orange), +15% (green), +20% (light blue), and +30% (dark blue).

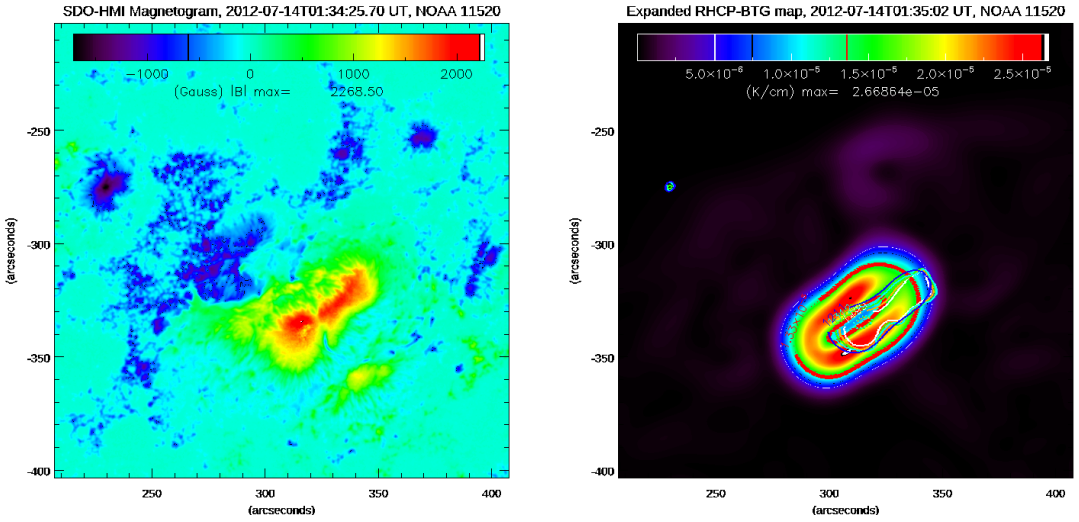

(a) (b)

Source: Figure (a): Adapted from NASA (2012).

6.1.7 Active region NOAA 11877 (October 24, 2013)

Analyzing this region, this work also identified brightness bumps with high right-hand circular polarization. In almost all radio maps belonging to this region, such bumps appear (almost) entirely characterized by their $|r_c|$ between 30% and 70%, reaching 80% in some cases (see the Figure 6.32(a)). As in the other cases, the extrapolated field lines slightly inclined with the observation line are preferentially distributed over such highly polarized bump (see the Figure 6.32(b)). In this case, the extrapolated magnetogram (Figure 6.35(a)) refers to 01:58:59 UT, and the RHCP-BTG map overlaid by the extrapolation lines corresponds to 02:00:01 UT.

From this area of high polarization, the ${T_b}^{(R)}$ ranged from $(1.3 \pm 0.1) \times 10^4$ to $(1.3 \pm 0.2) \times 10^5$ K and the $\left|\vec{\nabla} {T_b}^{(R)}\right|$ ranged from $(2.0 \pm 0.6) \times 10^{-5}$ to $(9.0 \pm 1.4) \times 10^{-5}$ K cm^{-1}. From the low-polarization area, the ${T_b}^{(R)}$ ranged from $(4.8 \pm 0.2) \times 10^3$ to $(2.2 \pm 0.6) \times 10^4$ K, while $\left|\vec{\nabla} {T_b}^{(R)}\right|$ ranged from $(2.2 \pm 0.6) \times 10^{-8}$ to (4.0

$\pm$ 0.6) $\times$ 10^{-5} K cm^{-1}. The averages of the maximum results of high-polarization ${T_b}^{(R)}$ and $\left|\vec{\nabla}{T_b}^{(R)}\right|$, then, are respectively 478.894% and 123.287% higher than the averages of the maximum results of low-polarization ${T_b}^{(R)}$ and $\left|\vec{\nabla}{T_b}^{(R)}\right|$ in that order.

Figure 6.32 - RHCP-BTG maps of region NOAA 11877 (at October 24, 2013, 02:00:01 UT) on which are white contours of: (a) the high circular polarization and (b) the cosine of the angle between the extrapolated magnetic field and the line of sight. This extrapolation considered $\alpha = 0.0$ and a cube size of 399^3 voxels over this area. The red thick-line contour indicates half of the maximum value of $\left|\vec{\nabla}{T_b}^{(R)}\right|$ in each map.

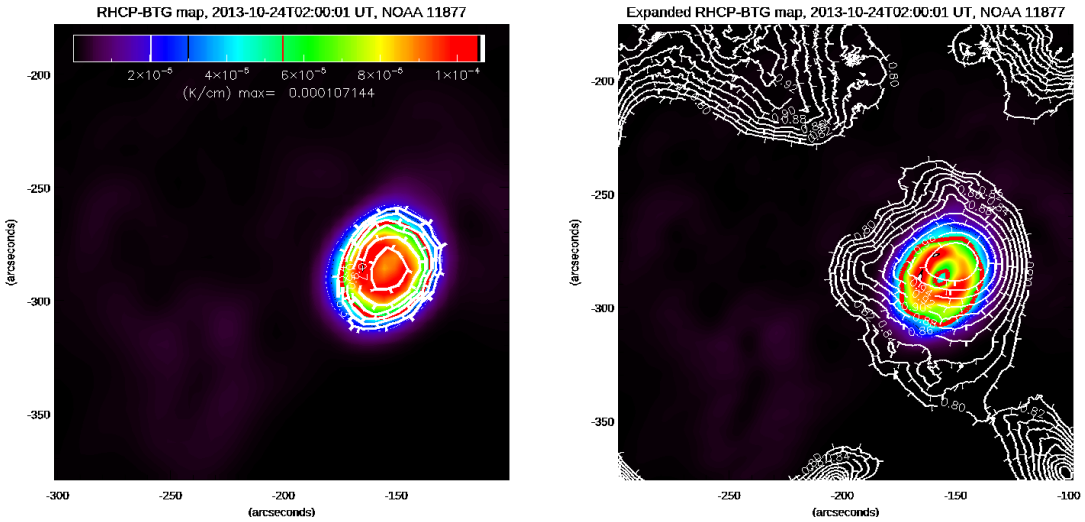

(a) (b)

Considering all these variations, the averages of the minimum results of the high-polarization ${T_b}^{(R)}$ and $\left|\vec{\nabla}{T_b}^{(R)}\right|$ are exceeded, respectively, by 77.6740% and 101.380% of their respective values by the averages of the maximum results of the low-polarization ${T_b}^{(R)}$ and $\left|\vec{\nabla}{T_b}^{(R)}\right|$ in that order. The averaging of the maximum values of the brightness variables did not include two radio maps in which very high brightness temperatures are recorded (4.4×10^5 and 1.1×10^6 K) following the occurrence of an M-class flare, which occurred at 00:21 UT according to the Solar Monitor[12].

As for the statistical analysis, it was performed using scatter plots containing from 3604 to 3664 points corresponding to the low-polarization areas and from 57 to 117 points corresponding to the high-polarization areas (see the Figures 6.33(a) and

[12]https://solarmonitor.org/?date=20131024

6.33(b)).

Figure 6.33 - Scatter plots related to: (a): $T_b^{(R)}$ vs. r_c, and (b): $\left|\vec{\nabla}T_b^{(R)}\right|$ vs. r_c for the active region NOAA 11877 at October 24, 2013, 02:00:01 UT. In these graphs, the fitting curve considers the polarization starting at 0.01.

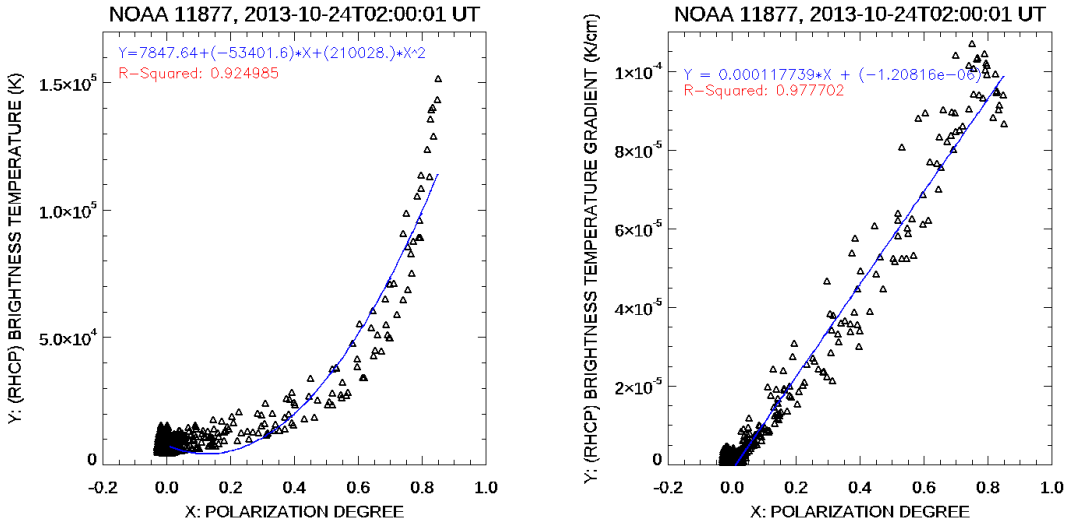

(a) (b)

This region, then, also shows a strong correlation between each high-polarization brightness variable and $|r_c|$, except in the 20 minutes following the M-class flare, and a weak to a medium correlation between each low-polarization brightness variable and $|r_c|$ (see the Figures 6.34(a) and 6.34(b)). Outside the time interval of influence of this flare, the correlation then obtained from the highly polarized emission is 0.79 to 0.98 for ${T_b}^{(R)}$, and 0.65 to 0.91 for $\left|\vec{\nabla}T_b^{(R)}\right|$. The correlation obtained from the low-polarization emission, on the other hand, lies between 0.02 and 0.39 for ${T_b}^{(R)}$, and between 0.07 and 0.49 for $\left|\vec{\nabla}T_b^{(R)}\right|$ (see the Figures 6.34(a) and 6.34(b)). Among these statistical results, the correlation obtained for high polarization is predominantly significant, except in 1 out of 38 RHCP-BT maps and 2 out of 38 RHCP-BTG maps. The correlation with $|r_c| < 30\%$ also obtained high significance in most maps, except in 4 out of 38 RHCP-BT maps.

The result of the magnetogram extrapolation (Figure 6.35) of this region also indicates the presence of the magnetic field linked to the extended 3rd and 4th harmonics over a considerable part of the brightness bump (Figure 6.35(b)). Also, it was found that the widest range of the extended 4th harmonic levels best fit over this bump.

Table 6.7 shows the estimated heights for the extrapolated magnetic fields corresponding to these extended harmonics.

Figure 6.34 - Degree of Spearman correlation of $|r_c|$ with (a): $T_b^{(R)}$ and (b): $\left|\vec{\nabla} T_b^{(R)}\right|$ for each NoRH map of the region NOAA 11877 at October 24, 2013. The blue triangles represent the correlation with $|r_c| \geq 30\%$, while the red squares indicate the correlation with $|r_c| < 30\%$. The correlation of $|r_c| \geq 30\%$ is highly significant, except for the 5th RHCP-BT map and the 4th and 5th RHCP-BTG maps. Correlation of $|r_c| < 30\%$ is also highly significant, except for the 21st, 26th, 32nd, and 38th RHCP-BT maps.

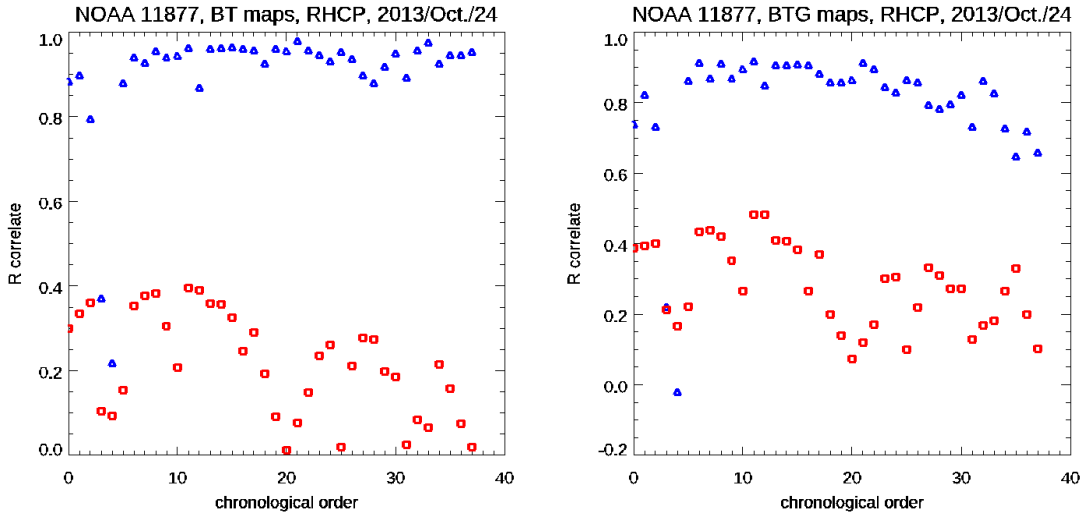

(a) (b)

Table 6.7 - For region NOAA 11877 at October 24, 2013: Height (in Km) of the extrapolated magnetic fields associated with the extended harmonics.

Harmonic	±5%	±10%	±15%	±20%	±30%
3rd	350-700	350-1050	350-1400	350-1750	350-2450
4th	350-2450	350-2800	350-3150	350-3500	350-4550

Figure 6.35 - Region NOAA 11877 at October 24, 2013: (a) SDO-HMI magnetogram (at 01:58:59 UT) and (b) its extrapolated magnetic field level lines over expanded RHCP-BTG map (at 02:00:01 UT). (b): The dotted lines indicate magnetic field strengths corresponding to extended 3rd harmonic, while the thick lines (except the red one) indicate fields associated with extended 4th harmonic. (b): Represented by the colors in the lines, the broadening of the harmonics are +5% (white), +10% (orange), +15% (green), +20% (light blue), and +30% (dark blue).

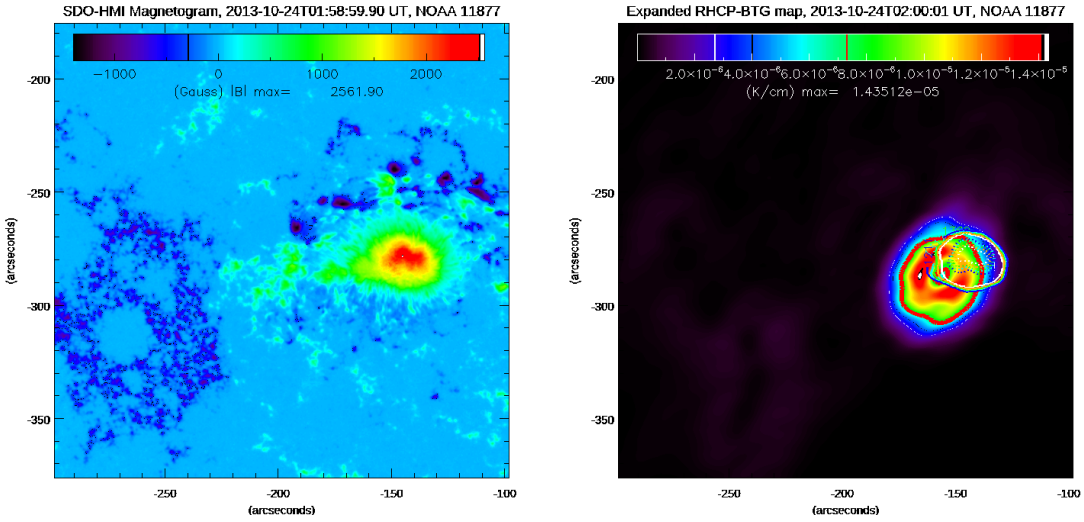

(a) (b)

Source: Figure (a): Adapted from NASA (2013a).

6.1.8 Active region NOAA 11899 (November 16, 2013)

Finally, the 17 GHz emission from this region on this day was also characterized by a highly polarized brightness bump (see Figure 6.36(a)). In this case, it was left-handed sense. Among its 39 BTG maps, the highest levels are between 70% and 85%. As for the magnetogram extrapolation over one of the BTG maps, the SDO-HMI data for this day corresponds to 01:58:57 UT, while the NoRH data for the same day refers to 02:00:00 UT. The extrapolated field lines over the bump then indicated a reduction in slope to near zero angles (see Figure 6.36(b)).

From the brightness bump area, then, where $|r_c| \geq 30\%$, the ${T_b}^{(L)}$ increased from $(1.3 \pm 0.1) \times 10^4$ to $(3.0 \pm 0.5) \times 10^5$ K, whereas, from the remaining area, ${T_b}^{(L)}$ ranged from $(4.5 \pm 0.3) \times 10^3$ to $(1.9 \pm 0.2) \times 10^4$ K. These results indicate that the average of the maximum values of the high-polarization ${T_b}^{(L)}$ is 1509.49% greater than the average of the maximum values of the low-polarization ${T_b}^{(L)}$. This last average is

49.8156% greater than the average of the minimum values of the high-polarization ${T_b}^{(L)}$.

Figure 6.36 - LHCP-BTG maps of region NOAA 11899 (at November 16, 2013, 02:00:00 UT) on which are white contours of: (a) the high circular polarization and (b) the cosine of the angle between the extrapolated magnetic field and the line of sight. This extrapolation considered $\alpha = 0.0$ and a cube size of 399^3 voxels over this area. The red thick-line contour indicates half of the maximum value of $\left|\vec{\nabla} T_b^{(L)}\right|$ in each map.

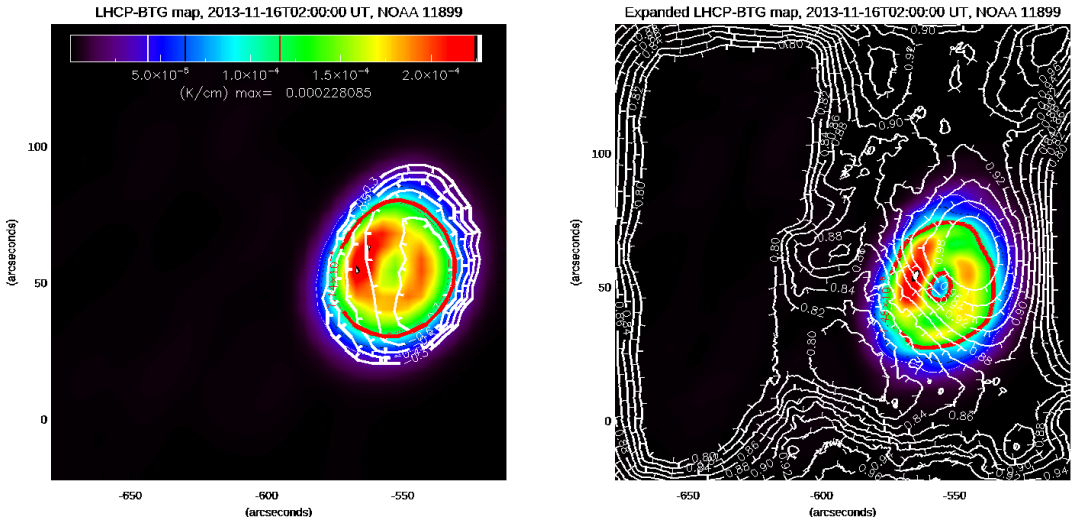

(a) (b)

For $\left|\vec{\nabla} T_b^{(L)}\right|$, the variation occurred from $(1.3 \pm 0.4) \times 10^{-8}$ to $(6.0 \pm 1.0) \times 10^{-5}$ K cm^{-1} in the area from where the emission was low polarized, whereas it was from $(1.9 \pm 0.5) \times 10^{-5}$ to $(2.1 \pm 0.3) \times 10^{-4}$ K cm^{-1} from the area of highly polarized emission. These results show that the average of the maximum values of high-polarization $\left|\vec{\nabla} T_b^{(L)}\right|$ is 255.049% greater than the average of the maximum values of low-polarization $\left|\vec{\nabla} T_b^{(L)}\right|$. This last average is 215.968% greater than the average of the minimum values of high-polarization $\left|\vec{\nabla} T_b^{(L)}\right|$.

For the correlation analysis, the maps of this region provided scatter plots (associating each brightness variable with its circular polarization module) containing 6332 to 6430 points from the area where $|r_c| < 30\%$, and containing 131 to 229 points from the area where $|r_c| \geq 30\%$ (see the Figures 6.37(a) and 6.37(b)).

Figure 6.37 - Scatter plots related to: (a): $T_b^{(L)}$ vs. r_c, and (b): $\left|\vec{\nabla} T_b^{(L)}\right|$ vs. r_c for the active region NOAA 11899 at November 16, 2013, 02:00:00 UT. In these graphs, the fitting curve considers the polarization starting at -0.1.

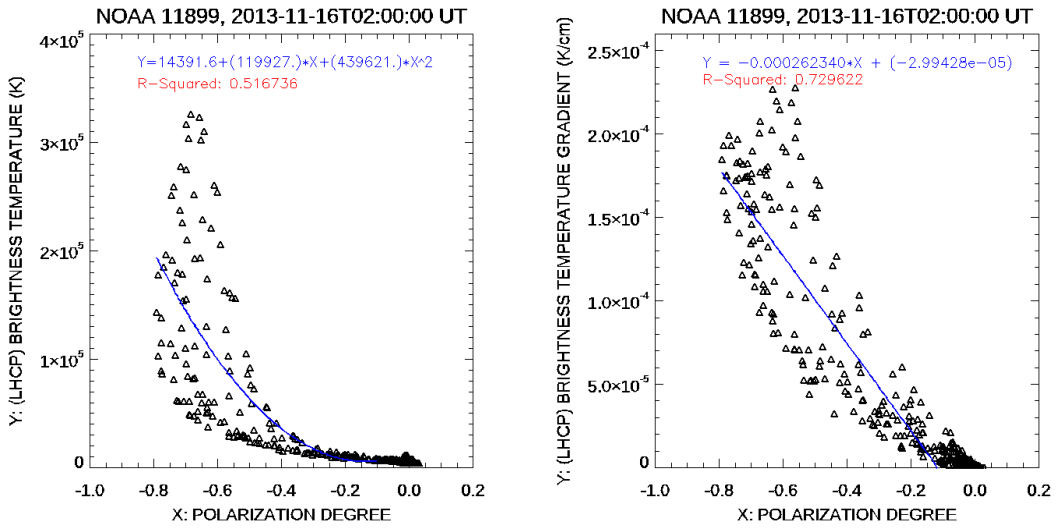

(a) (b)

Such scatter plots, then, also show that each brightness variable strongly correlates with $|r_c| \geq 30\%$, while correlating weakly or moderately with $|r_c| < 30\%$ (see the Figures 6.38(a) and 6.38(b)). For high-polarization $T_b^{(L)}$, such correlation lies between 0.69 and 0.92, while for low-polarization $T_b^{(L)}$, it ranges from 0.05 to 0.39. For the highly polarized $\left|\vec{\nabla} T_b^{(L)}\right|$, the correlation lies between 0.62 and 0.84, while for the weakly polarized $\left|\vec{\nabla} T_b^{(L)}\right|$, the correlation ranges from 0.05 to 0.39. Such data shows high significance, as well as all maps' correlations with $|r_c| \geq 30\%$. With $|r_c| < 30\%$, the correlation is highly significant in 35 out of 39 LHCP-BT maps and 38 out of 39 LHCP-BTG maps.

From the extrapolation of the magnetogram (Figure 6.39(a)), it was also obtained, over the brightness bump of this region, the emergence of the magnetic field related to the extended 3rd and 4th harmonics (Figure 6.39(b)). Similarly to the previous cases, the extended 4th harmonic demonstrates greater coverage in the area of the brightness bump. The estimated heights of the extrapolated magnetic fields associated with the extended 3rd and 4th harmonics are shown in Table 6.8.

Figure 6.38 - Degree of Spearman correlation of $|r_c|$ with (a): $T_b^{(L)}$ and (b): $\left|\vec{\nabla} T_b^{(L)}\right|$ for each NoRH map of the region NOAA 11899 at November 16, 2013. The blue triangles represent the correlation with $|r_c| \geq 30\%$, while the red squares indicate the correlation with $|r_c| < 30\%$. These results are highly significant, except those obtained in correlation with $|r_c| < 30\%$ through the 14th, 18th, 35th, and 39th LHCP-BT maps, and the 6th LHCP-BTG.

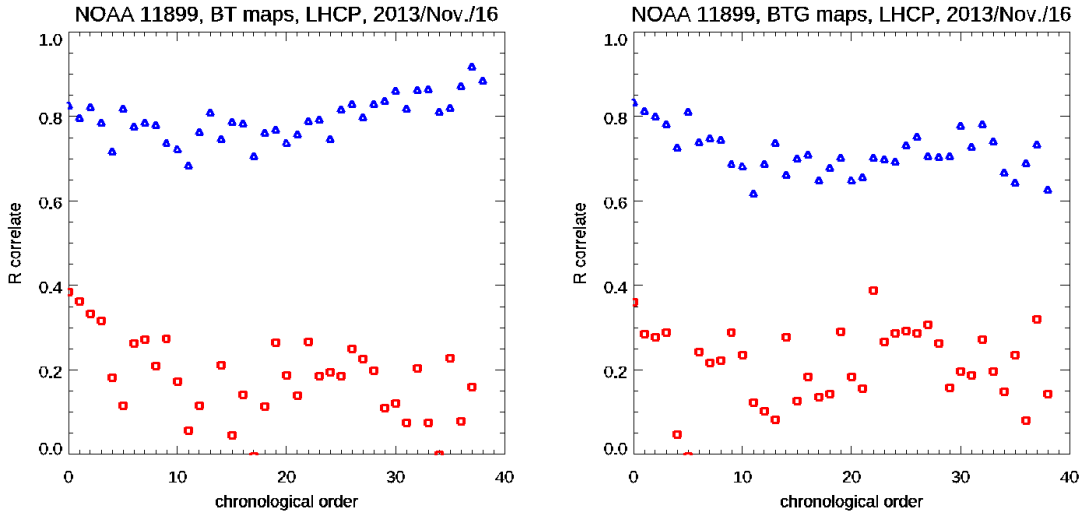

(a) (b)

Table 6.8 - For region NOAA 11899 at November 16, 2013: Height (in Km) of the extrapolated magnetic fields associated with the extended harmonics.

Harmonic	±5%	±10%	±15%	±20%	±30%
3rd	350-1400	350-1750	350-1750	350-2450	350-3150
4th	350-3150	350-3500	350-3850	350-4200	350-5250

Figure 6.39 - Region NOAA 11899 at November 16, 2013: (a) SDO-HMI magnetogram (at 01:58:57 UT) and (b) its extrapolated magnetic field level lines over expanded LHCP-BTG map (at 02:00:00 UT). (b): The dotted lines indicate magnetic field strengths corresponding to extended 3rd harmonic, while the thick lines (except the red one) indicate fields associated with extended 4th harmonic. (b): Represented by the colors in the lines, the broadening of the harmonics are +5% (white), +10% (orange), +15% (green), +20% (light blue), and +30% (dark blue).

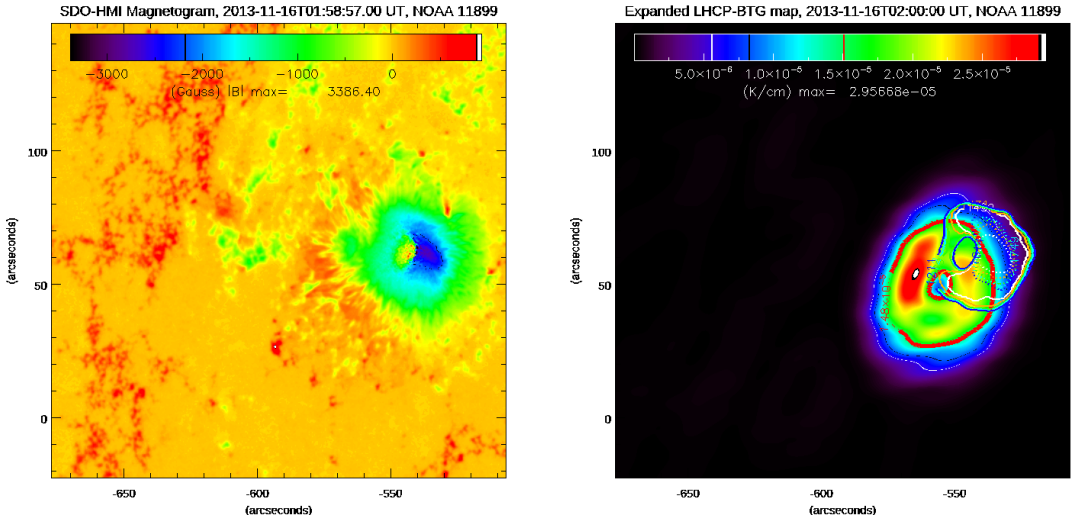

(a) (b)

Source: Figure (a): Adapted from NASA (2013a).

7 CONCLUDING REMARKS

The present thesis aimed to verify the association of gyroresonance with the appearance of 17 GHz brightness bumps in active regions and to statistically characterize the relationship of such a radio emission mechanism with brightness intensification at this frequency using solar maps synthesized by NoRH. Several previous works, *e.g.* Ginzburg and Zheleznyakov (1961), Kundu et al. (1977), Alissandrakis et al. (1980), Alissandrakis and Kundu (1982), and Lang and Willson (1982), have already demonstrated the key role of gyroresonance in brightness enhancement at frequencies below 17 GHz. However, until the present work, precise information about the correlation between the brightness temperature gradient and such a radio mechanism was still lacking.

This work then analyzed 8 active regions with strong magnetic fields to produce gyroresonance. The data then showed the presence of intense brightness bumps completely or partially involving the magnetic field contours associated with such radio process. The BTG maps show most of these bumps as high circular polarization ($|r_c| \geq 30\%$) emission, which also turns out to be strong evidence for the presence of the gyroresonant mechanism. On the other hand, some of these maps show low polarization at the edges and in the center of the bumps, including low-polarized spots, evidencing the participation of bremsstrahlung in the brightness intensification process at 17 GHz. The distribution of the brightness temperature gradient in the BTG maps also revealed a tendency toward formations of contours analogous to horseshoes in the bumps and to guts outside the bumps. Horseshoes had already been observed at 5.0 GHz by Lang and Willson (1982) through circular polarization contours on maps of an active region, as discussed in Chapter 3 (Section 3.3). They had already found then that the center of this formation was of low brightness intensification and was contoured by an area of a high-temperature gradient.

This thesis also performed linear force-free extrapolation of HMI-SDO magnetograms from each selected region. Their results indicated the recurrence of bump association with gyroresonance and the prevalent contribution of the 4th harmonic plus broadening up to 30%. Among the results of this extrapolation, a distribution of cosines of the inclination angle between the magnetic field line and the line of sight was identified. Arranged in contour lines, this distribution indicated the presence of less inclined field lines over the highly polarized bumps, which explains the high circular polarization in such bumps, corroborating the evidence for gyroresonance in such areas of brightness intensification. Although White and Kundu (1997) and

Vourlidas et al. (2006) have shown a positive correlation between this tilt angle and opacity, the results of this thesis, without opposing such authors, indicate an inverse relationship between such tilt and the brightness variables T_b and $\left|\vec{\nabla T_b}\right|$. Although these extrapolation results assume a scenario without intense current sheets and further analysis can still be done later using the radiative transfer equation until the BTG maps are properly simulated, the extrapolation results converged in several cases on this common finding about the contribution of gyroresonance.

Statistical analysis, in turn, revealed that generally, both brightness temperature and its gradient (considering their respective prevailing sense of polarization) showed a strong correlation with $|r_c| \geq 30\%$, and weak or moderate correlation with $|r_c| < 30\%$. Such weak/moderate correlation was observed in all cases. Given that among the observed active regions, some produced flares for the highly polarized emission, however, such correlation tends to attenuate to moderate values during flares or at times close to such events.

This work also checked the brightness temperature profiles and its gradient, varying with the degree of circular polarization. It was then found that the brightness temperature profiles (associated with their respective predominant sense of polarization) closely approximate a 2-degree polynomial curve in most cases, in which there was (were) no (or few) flare(s). In these cases, then, the profiles of the brightness temperature gradient (characterized by its prevailing sense of polarization) were found to fit well into a linear relationship with the degree of polarization.

We should also consider that the explanation given by Lang and Willson (1982) for the peak of temperature gradient distributed in a horseshoe shape is quite adequate for the maxima peak observed in the BTG maps of the present thesis. Still, as in this thesis, their work did not show the concentric distribution of such a gradient around the horseshoe. This distribution reveals that the brightness temperature gradient grows toward the center of the bump formation, as does the brightness temperature and the modulus of the circular polarization degree. The scenario of a simultaneous increase in both $|r_c|$ and brightness variables points to the high polarization degree as an indicator of gyroresonance participation in this process. Such results indicate, then, that in gyroresonance, the rise in the degree of polarization is accompanied by an increase not only in brightness but also in the gradient of such brightness in the 17 GHz maps. As a likely cause of this effect, the distribution of gyroresonant electrons with a gyro orientation of low inclination to the line of sight increases when approaching similarly less inclined magnetic field lines. Generally,

such low-slope field lines emerge from magnetic poles, with more intense magnetic strength. Thus, a likely explanation for such an occurrence is a putative magnetic pressure gradient in the pole direction in the areas of brightness bumps where $|r_c| \geq 30\%$. The increased participation of electrons associated with the gyroresonance, evidenced by the increase in polarization degree modulus, can be caused by a rise in magnetic pressure to increasingly keep these electrons cohesive to the field lines as the magnetic field strength increases.

On the other hand, the analysis of each map found that the maximum $\left|\vec{\nabla}T_b\right|$ values of $|r_c| < 30\%$ exceed the minimum $\left|\vec{\nabla}T_b\right|$ values of $|r_c| \geq 30\%$ in predominantly sense of polarization emissions. This fact shows that it is still necessary to filter the gradients to identify the ranges of values that reveal a source of gyroresonance.

The finding obtained in this work about the strong correlation between the brightness temperature gradient and the degree of polarization associated with gyroresonance suggests that BTG maps at 17 GHz may be a very useful means to study the evolution of the chromospheric magnetic field associated with such a radio mechanism. Considering this correlation, it is likely that such a gradient should also correlate very well with this field, which, if it is confirmed, will provide the emergence of a method for mapping magnetic field strength associated with gyroresonant emission.

Therefore, future work is suggested to raise models that simulate a sequence of BTG maps over gyroresonant emission sources to reconstruct, using linear force-free extrapolation, the magnetic field directly associated with gyroresonance. If the proposed method for magnetic mapping holds, it will be possible to analyze the gyroresonant field more simply and directly without needing magnetogram extrapolation. This new task may be interesting to verify some possible magnetic patterns (not yet found) preceding the occurrence of flares, which would contribute significantly to predicting these events and the space weather warning system.

REFERENCES

ALISSANDRAKIS, C.; KUNDU, M. Observations of ring structure in a sunspot associated source at 6 centimeter wavelength. **Astrophysical Journal**, v. 253, p. L49–L52, 1982. xv, 21, 79

ALISSANDRAKIS, C.; KUNDU, M.; LANTOS, P. A model for sunspot associated emission at 6 cm wavelength. **Astronomy and Astrophysics**, v. 82, p. 30–40, 1980. 20, 22, 79

APPLETON EV & HEY, J. Circular polarization of solar radio noise. **Nature**, v. 158, n. 4010, p. 339–339, 1946. 1

ASCHWANDEN, M. **Physics of the solar corona: an introduction with problems and solutions**. [S.l.]: Springer Science & Business Media, 2006. xv, 1, 2, 9, 24

ASCHWANDEN, M. J. **Particle acceleration and kinematics in solar flares**. [S.l.]: Springer, 2002. 1–227 p. 5, 13, 19

AVRETT, E. H.; LOESER, R. Models of the solar chromosphere and transition region from sumer and hrts observations: formation of the extreme-ultraviolet spectrum of hydrogen, carbon, and oxygen. **The Astrophysical Journal Supplement Series**, v. 175, n. 1, p. 229, 2008. 7

BENZ, A. O. Flare observations. **Living Reviews in Solar Physics**, v. 14, n. 1, p. 2, Dec 2016. ISSN 1614-4961. Available from: <<https://doi.org/10.1007/s41116-016-0004-3>>. 11

BOGOD, V.; ALISSANDRAKIS, C.; KALTMAN, T.; TOKHCHUKOVA, S. K. Ratan-600 observations of small-scale structures with high spectral resolution. **Solar Physics**, v. 290, p. 7–20, 2015. 8

CARRINGTON, R. C. Description of a singular appearance seen in the sun on september 1, 1859. **Monthly Notices of the Royal Astronomical Society**, v. 20, p. 13–15, 1859. 1

COVINGTON, A. Micro-wave solar noise observations during the partial eclipse of november 23, 1946. **Nature**, v. 159, n. 4038, p. 405, 1947. 1

DRIEL-GESZTELYI, L. van; GREEN, L. M. Evolution of active regions. **Living Reviews in Solar Physics**, v. 12, p. 1–98, 2015. 10

DULK, G. A. Radio emission from the sun and stars. **Annual review of astronomy and astrophysics**, v. 23, n. 1, p. 169–224, 1985. 5, 13, 14, 16

EXPANDED OWENS VALLEY SOLAR ARRAY. **Welcome to the expanded owens valley solar array**. 2023. Available from: <<http://www.ovsa.njit.edu/>>. Access in: 2023-01-30. 26

FANNING, D. W. **Coyote's Guide to IDL Programming**. 2018. Available from: <<http://www.idlcoyote.com/>>. Access in: 2021-12-27. 29

FLEISHMAN, G. D.; KUZNETSOV, A. A. Theory of gyroresonance and free–free emissions from non-maxwellian quasi-steady-state electron distributions. **The Astrophysical Journal**, v. 781, n. 2, p. 77, 2014. 13

FREELAND, S.; HANDY, B. Data analysis with the solarsoft system. **Solar Physics**, v. 182, p. 497–500, 1998. 29

GANGADHARA, R.; HAN, J.; WANG, P. Coherent curvature radio emission and polarization from pulsars. **The Astrophysical Journal**, v. 911, n. 2, p. 152, 2021. 13

GINZBURG, V.; ZHELEZNYAKOV, V. Noncoherent mechanisms of sporadic solar radio emission in the case of a magnetoactive coronal plasma. **Soviet Astronomy**, v. 5, p. 1, 1961. 2, 19, 79

HADDOCK, F. Introduction to radio astronomy. **Proceedings of the IRE**, v. 46, n. 1, p. 3–12, 1958. 1

HINODE SCIENCE CENTER PROJECT, INSTITUTE FOR SPACE-EARTH ENVIRONMENTAL RESEARCH, NAGOYA UNIVERSITY, THE INTERNATIONAL CONSORTIUM FOR THE CONTINUED OPERATION OF NOBEYAMA RADIOHELIOGRAPH. **The International Consortium for the Continued Operation of Nobeyama Radioheliograph (ICCON)**. 2020. Available from: <<https://hinode.isee.nagoya-u.ac.jp/ICCON/>>. Access in: 2023-01-10. 26

HODGSON, R. On a curious appearance seen in the sun. **Monthly Notices of the Royal Astronomical Society**, v. 20, p. 15–16, 1859. 1

INTERNATIONAL CONSORTIUM FOR THE CONTINUED OPERATION OF NOBEYAMA RADIOHELIOGRAPH. **Nobeyama Radioheliograph (NoRH): Analysis Manual: ver. 3.3**. Japan, 2015. Available from: <<https://solar.nro.nao.ac.jp/norh/doc/man_v33e.pdf>>. Access in: 2021-12-20. 16, 29, 30, 34, 35

KAKINUMA, T.; SWARUP, G. A model for the sources of the slowly varying component of microwave solar radiation. **The Astrophysical Journal**, v. 136, p. 975, 1962. 2, 19

KERDRAON, A.; DELOUIS, J.-M. The nançay radioheliograph. In: CORONAL PHYSICS FROM RADIO AND SPACE OBSERVATIONS, 1996, Nouan le Fuzelier, France. **Proceedings...** Berlin, Heidelberg: Springer, 1997. p. 192–201. 26

KHOMENKO, E.; COLLADOS, M.; SOLANKI, S.; LAGG, A.; BUENO, J. T. Quiet-sun inter-network magnetic fields observed in the infrared. **Astronomy & Astrophysics**, v. 408, n. 3, p. 1115–1135, 2003. 8

KIEPENHEUER, K. O. Preface and introduction. In: KIEPENHEUER, K. O. (Ed.). **Structure and development of solar active regions**. [S.l.: s.n.], 1968. (IAU Symposium, v. 35), p. 3. 9

KONTAR, E.; PEREZ, J.; HARRA, L.; KUZNETSOV, A.; EMSLIE, A.; JEFFREY, N.; BIAN, N.; DENNIS, B. Turbulent kinetic energy in the energy balance of a solar flare. **Physical Review Letters**, v. 118, n. 15, p. 155101, 2017. xv, 10

KOSHIISHI, H. et al. Evaluation of the imaging performance of the nobeyama radioheliograph. **Publications of the Astronomical Society of Japan**, v. 46, p. L33–L36, 1994. xv, 27

KUNDU, M. R.; ALISSANDRAKIS, C.; BREGMAN, J.; HIN, A. 6 centimeter observations of solar active regions with 6 sec resolution. **The Astrophysical Journal**, v. 213, p. 278–295, 1977. xv, 20, 22, 79

LANG, K. R.; WILLSON, R. F. Very large array observations of solar active regions. **Nature**, v. 278, n. 5699, p. 24–28, 1979. 22

_____. Polarized horseshoes around sunspots at 6 centimeter wavelength. **The Astrophysical Journal**, v. 255, p. L111–L117, 1982. xv, 22, 23, 79, 80

LEE, J. Radio emissions from solar active regions. **Space Science Reviews**, v. 133, n. 1-4, p. 73–102, 2007. 2, 16

LIN, H.; PENN, M. J.; TOMCZYK, S. A new precise measurement of the coronal magnetic field strength. **The Astrophysical Journal**, v. 541, n. 2, p. L83, 2000. 8

LIU, Y. et al. A first look at magnetic field data products from sdo/hmi. In: 4TH HINODE SCIENCE MEETING: UNSOLVED PROBLEMS AND RECENT INSIGHTS, 4., 2010, Palermo, Italy. **Proceedings...** San Francisco: ASP Conference series, 2012. p. 337. 29, 30

LUGTEN, J. Optical design and performance of the bima interferometer. **BIMA Memo**, n. 39, 1995. 26

MELROSE, D. Coherent emission mechanisms in astrophysical plasmas. **Reviews of Modern Plasma Physics**, v. 1, p. 1–81, 2017. 17

MULLAN, D. J. **Physics of the Sun: A First Course**. [S.l.]: Chapman and Hall; CRC, 2009. 7

NAKAJIMA, H. et al. New nobeyama radio heliograph. **Journal of Astrophysics and Astronomy Supplement**, v. 16, p. 437, 1995. 26

NAKAJIMA, H. A. et al. The nobeyama radioheliograph. **Proceedings of the IEEE**, v. 82, n. 5, p. 705–713, 1994. xv, 25, 26, 27

NATIONAL AERONAUTICS AND SPACE ADMINISTRATION. **SDO HMI Magnetogram**. 2011. 43, 47, 53, 57

_____. _____. 2012. 61, 65, 69

_____. _____. 2013. 73, 77

_____. **Solar dynamics observatory shows sun's rainbow of wavelengths**. 2013. Available from: <<https://www.nasa.gov/content/solar-dynamics-observatory-shows-suns-rainbow-of-wavelengths>>. Access in: 2023-02-12. 1

_____. **SDO gallery**. 2023. Available from: <<https://sdo.gsfc.nasa.gov/gallery/main>>. Access in: 2023-02-27. xv, 10

NINDOS, A. Incoherent solar radio emission. **Frontiers in Astronomy and Space Sciences**, v. 7, p. 57, 2020. 13, 14, 16, 17, 18

NITTA, N. V.; SUN, X.; HOEKSEMA, J. T.; DEROSA, M. L. Solar cycle variations of the radio brightness of the solar polar regions as observed by the nobeyama radioheliograph. **The Astrophysical Journal Letters**, v. 780, n. 2, p. L23, 2013. 29, 30

NOBEYAMA RADIOHELIOGRAPH. **Index of /norh/images/10min/2011/08/02**. 2011. National Astronomical Observatory of Japan. Available from: <<https://solar.nro.nao.ac.jp/norh/images/10min/2011/08/02/>>. Access in: 2021-12-10. 3, 34

NOBEYAMA SOLAR RADIO OBSERVATORY, NAOJ. **Nobeyama Radioheliograph (NoRH): Analysis Manual: ver. 3.2**. Japan, 2013. Available from: <<https://solar.nro.nao.ac.jp/norh/doc/manuale.pdf>>. Access in: 2021-12-20. 16, 29, 30, 34, 35

NOBEYAMA SOLAR RADIO OBSERVATORY, NOBEYAMA RADIO OBSERVATORY, NATIONAL ASTRONOMICAL OBSERVATORY OF JAPAN. **Nobeyama Solar Radio Observatory, NAOJ**. 2015. Available from: <<https://solar.nro.nao.ac.jp/>>. Access in: 2023-01-10. 26

PLANCK, M. On an improvement of wien's equation for the spectrum. **Annals Physik**, v. 1, p. 719–721, 1900. 14

PORFIR'EVA, G.; YAKUNINA, G. On fine structure in solar flares from sdo, rhessi and trace observations. **Sun and Geosphere**, v. 8, n. 2, p. 77–81, 2013. 1

PRIEST, E. **Magnetohydrodynamics of the Sun**. [S.l.]: Cambridge University Press, 2014. 7, 8, 9, 10

RYBICKI, G. B.; LIGHTMAN, A. P. **Radiative processes in astrophysics**. [S.l.]: John Wiley & Sons, 1991. 13

SCHEDIWY, S. A clock for the square kilometre array. In: FROM ANTIKYTHERA TO THE SQUARE KILOMETRE ARRAY: LESSONS FROM THE ANCIENTS, 2012, Kerastari, Greece. **Proceedings...** Kerastari: Sissa Medialab, 2013. p. 31. xv, 25

SELHORST, C.; COSTA, J.; CASTRO, C. G. de; VALIO, A.; PACINI, A.; SHIBASAKI, K. The 17 ghz active region number. **The Astrophysical Journal**, v. 790, n. 2, p. 134, 2014. 10

SELHORST, C.; SILVA-VÁLIO, A.; COSTA, J. Solar atmospheric model over a highly polarized 17 ghz active region. **Astronomy & Astrophysics**, v. 488, n. 3, p. 1079–1084, 2008. 2, 23

SELHORST, C. L. Modelo de regiões ativas em rádio freqüências. 2007. 2

SHIMOJO, M.; IWAI, K. Over seven decades of solar microwave data obtained with toyokawa and nobeyama radio polarimeters. **Geoscience Data Journal**, v. 10, n. 1, p. 114–129, 2023. 1

SHIMOJO, M. et al. Observing the sun with the atacama large millimeter/submillimeter array (alma): high-resolution interferometric imaging. **Solar Physics**, v. 292, n. 7, p. 1–28, 2017. 26

SILVA, A. J. O.; SELHORST, C. L.; COSTA, J. E.; SIMÕES, P. J.; CASTRO, C. G. G.; WEDEMEYER, S.; WHITE, S. M.; BRAJŠA, R.; VALIO, A. A genetic algorithm to model solar radio active regions from 3d magnetic field extrapolations. **Frontiers in Astronomy and Space Sciences**, v. 9, p. 911118, 2022. 24

TAKANO, T. et al. An upgrade of nobeyama radioheliograph to a dual-frequency (17 and 34 ghz) system. In: CORONAL PHYSICS FROM RADIO AND SPACE OBSERVATIONS, 1996, Nouan le Fuzelier, France. **Proceedings...** Berlin, Heidelberg: Springer, 1997. p. 183–191. 26

THE NATIONAL RADIO ASTRONOMY OBSERVATORY. **Very large array**. 2023. Available from: <<https://public.nrao.edu/telescopes/vla/>>. Access in: 2023-01-30. 26

The SunPy Community; BARNES, W. T.; BOBRA, M. G.; CHRISTE, S. D.; FREIJ, N.; HAYES, L. A.; IRELAND, J.; MUMFORD, S.; PEREZ-SUAREZ, D.; RYAN, D. F.; SHIH, A. Y.; CHANDA, P.; GLOGOWSKI, K.; HEWETT, R.; HUGHITT, V. K.; HILL, A.; HIWARE, K.; INGLIS, A.; KIRK, M. S. F.; KONGE, S.; MASON, J. P.; MALONEY, S. A.; MURRAY, S. A.; PANDA, A.; PARK, J.; PEREIRA, T. M. D.; REARDON, K.; SAVAGE, S.; SIPőCZ, B. M.; STANSBY, D.; JAIN, Y.; TAYLOR, G.; YADAV, T.; RAJUL; DANG, T. K. The sunpy project: Open source development and status of the version 1.0 core package. **The Astrophysical Journal**, American Astronomical Society, v. 890, p. 68–, 2020. Available from: <<https://iopscience.iop.org/article/10.3847/1538-4357/ab4f7a>>. 29

VERNAZZA, J. E.; AVRETT, E. H.; LOESER, R. Structure of the solar chromosphere. iii-models of the euv brightness components of the quiet-sun. **The Astrophysical Journal Supplement Series**, v. 45, p. 635–725, 1981. 7

VOURLIDAS, A.; GARY, D. E.; SHIBASAKI, K. Sunspot gyroresonance emission at 17 ghz: a statistical study. **Publications of the Astronomical Society of Japan**, v. 58, n. 1, p. 11–20, 2006. 1, 2, 18, 22, 31, 35, 80

WELCH, W. J. et al. The berkeley-illinois-maryland-association millimeter array. **Publications of the Astronomical Society of the Pacific**, v. 108, n. 719, p. 93, 1996. 26

WHITE, S.; KUNDU, M. Radio observations of gyroresonance emission from coronal magnetic fields. **Solar Physics**, v. 174, n. 1-2, p. 31–52, 1997. 2, 5, 16, 18, 19, 79

WHITE, S. M. Coronal magnetic field measurements through gyroresonance emission. In: GARY, D.; KELLER, C. (Ed.). **Solar and space weather radiophysics**. [S.l.]: Springer, 2004. p. 89–113. 2, 18

YANG, S.; ZHANG, J.; JIN, C.; LI, L.; DUAN, H. Response of the solar atmosphere to magnetic field evolution in a coronal hole region. **Astronomy & Astrophysics**, v. 501, n. 2, p. 745–753, 2009. xv, 7, 8

ZHELEZNYAKOV, V. The origin of the slowly varying component of solar radio emission. **Soviet Astronomy**, v. 6, p. 3, 1962. 2, 20